Saman Khosravi Haji Vand, Fogh-lis

An Electrochemical Study of Novel Ti-based TFSOC on PEMFC Affordable Interconnects

DOCTORAL THESIS

to achieve the university degree of

Doktor der technischen Wissenschaften

submitted to

Graz University of Technology

Supervisor

Ao.Univ.-Prof. Dipl.-Ing. Dr.techn. Klaus Reichmann

Institut für Chemische Technologie von Materialien (ICTM)

Graz, November 2020

AFFIDAVIT

I declare that I have authored this thesis independently, that I have not used other than the declared sources/resources, and that I have explicitly indicated all material which has been quoted either literally or by content from the sources used. The text document uploaded to TUGRAZonline is identical to the present doctoral thesis.

Date, Signature

Abstract

This thesis work mainly focuses on the development of electrically conductive and highly electrochemical degradation resistant thin film solid oxide coatings (TFSOC) on C45E inexpensive low carbon steel and the evaluation of their applications in Proton Exchange Membrane Fuel Cell (PEMFC) technology. For this purpose, the thesis work involves the studies on how these novels TiSiN TFSOC prepared at different annealing temperatures in the nitrogen (N_2) atmosphere suppress degradation processes against the harsh acidic PEMFC environment during long-term immersion in standard condition solution (SCS). The reasonably low corrosion current density (I_{corr}) and the steady value of corrosion potential (E_{corr}) of the coated specimens over the long period confirm that the TFSOC can effectively restrain the surface electrochemical degradation caused by the highly acidic condition. Results also demonstrate that both N_2 atmosphere and niobium (Nb) with a more obvious impact than the N_2 significantly improve the electrical conductivity of the TFSOC. The presence of doped N_2 in the TFSOC and its electrochemical reaction (dissolution/transport) with H_2SO_4 in the PEMFC simulation environment, as well as the presence of iron oxide phases of the reference sample (RS) in the structure of the TFSOC are the cause for the effective and stable mechanism known as formation and consumption of metal ions, which has happened due to the restoring effect of TFSOC. Finally, the enriched N_2 at the RS/TFSOC interface decreases the anodic dissolution ratio, thereby reducing the I_{corr} and established the degradation resistance with high protective efficacy for the long-term operation. Following the formation of the metal oxide, the metal ions at a rate corresponding to the I_{corr} passed through the passive film. As a consequence, the degradation resistance can be constant over a long time in the presence of corrosive ions without raising the thickness of the passive film. These observations lead us to the conclusion that the TFSOC have long-lasting high resistance in the SCS, which is suitable for cost-effective metal interconnects in PEMFC applications.

Keywords:

PEMFC, Interconnect, Electrochemical degradation, Electrical conductivity, TFSOC

This thesis is dedicated to my beloved grandma **BB Delbar**.

I MISS YOU A BILLION TIMES OVER I MISS YOU

Preface

This thesis is a result of work performed between July 2017 and November 2020. The author was employed at the Institute for Chemistry and Technology of Materials (ICTM) at the Graz University of Technology in Austria, and the electrochemical characterization of work was performed in cooperation with the Institute of Materials Science, Joining and Forming (IMAT). **Prof. Klaus Reichmann** was supervisor from ICTM, while Dr. Rudolf Vallant contributed as a project-senior scientist from IMAT. The majority of the work described in this thesis was performed by Saman Khosravi H at the Institute for Chemistry and Technology of Materials (ICTM).

The following chapters have been prepared for publication as a review paper:

Chapter 1 is the introduction containing the background knowledge and principles of electrochemical degradation of the bare metal exposed in different conditions.

Chapter 2 is the introduction of polymer electrolyte membrane fuel cell and their interconnector.

Chapter 3 covers the literature survey of the electrochemical degradation and surface modification/coating of metal-based interconnects in PEMFC applications.

Parts of this work has been published in the following articles:

Chapter 4 of this thesis has been published as **Khosravi S**, Veerapandiyan VK, Vallant R, Reichmann K. Effect of processing conditions on the structural properties and corrosion behavior of TiO_2-SiO_2 multilayer coatings derived via the sol-gel method. Ceram Int 2020. Dr. Vallant helped with the electrochemical characterization. Prof. Reichmann provided valuable discussions, comments and suggestions for manuscript writing, revision and coating preparation and characterization.

Chapter 5 of this thesis has been published as **Khosravi H S**, Vallant R, Ladenstein L, Reichmann K. Electrochemical and Structural Property of TiSiNb TFSOC on Affordable Interconnects in Proton Exchange Membrane Fuel Cell Applications. Nanomaterials 2020;10:2010. Dr. Vallant helped with the electrochemical characterization, Ladenstein worked on the electrical conductivity of TFSOC under the guidance of Dr. Rettenwander, Prof. Hacker provided valuable discussion with the PEMFC, Prof. Reichmann provided valuable discussions, comments and suggestions for manuscript writing, revision and coating preparation and characterization.

Chapter 6 of the thesis includes the summary and future prospects.

November 30th 2020
Saman Khosravi H

Acknowledgements

First of all, I would like to express my sincere gratitude to my supervisor, Prof. Klaus Reichmann for his continuous support, guidance and inspiration. The constant critical feedback and encouragement I received from Prof. Reichmann help me in every step through the past four years. He inspired me to always stay motivated, to think and work as a Ph.D. candidate, to grow as a researcher, and to further pursue my career in research. I have been extremely lucky to have a supervisor who cared so much about my life and work, and who responded to my questions and queries so promptly.

Ich werde Sie immer als großartige Persönlichkeit in Erinnerung behalten. Ich wünschte es gäbe mehr Menschen wie Sie, die Welt wäre um vieles reicher.

Vielen Dank für Ihre Unterstützung!

Special thanks to Dr. Rudolf Valiant for providing the instruments of his group to electrochemical characterization all the coatings. Thank you, Dr. Rudolf Vallant, your help is much appreciated.

Danke sehr!

Table of Contents

List of Tables

List of Figures

List of Symbols

A_a	Surface of Anode
A_c	Surface of Cathode
$\Delta\phi a$	Anodic Site
$\Delta\phi c$	Cathode Site
$\Delta\phi_{S,a}$	Anode Solution
$\Delta\phi_{S,c}$	Cathode Solution
E''_M	Potential of Anode
E''_X	Potential of Cathode
I	Current
V	Voltage
E	Potential
R	Resistance
E_{thermo}	Thermodynamic Voltage
η	Overpotential
η_{act}	Overpotential Activation
η_{ohmic}	Overpotential Ohmic
η_{conc}	Overpotential Concentration
E_{rev}	Reversible Voltage
E_{irrev}	Irreversible Voltage Loss
ΔG	Gibbs Free Energy
ΔG^0	Standard Gibbs Free Energy
I_{corr}	Corrosion Current Density
E_{corr}	Corrosion Potential
R_p	Polarization Resistance
R_{ct}	Coating Resistance
R_S	Solution Resistance
R_M	Metal Paths Resistance
β_a	Anodic Tafel
β_c	Cathodic Tafel
ac	Alternating Current
Q	Electrolyte Interface
ω	Angular Frequency
j	Imaginary Constant
C	Capacitance
Ev	Energy Level of Valence Band
Ea	Activation Energy
e^-	Electron

List of Abbreviations

GDP	Gross Domestic Product
DOE	United States Department of Energy
SS	Stainless Steel
SS316L	SAE 316L Grade Stainless Steel
SS441	AISI 441 is a Ferritic Chromium Stainless Steel
C45E	Low-Alloyed Carbon Steel (AISI/SAE1045)
SS430	Straight Chromium AISI 430 Stainless Steel
OCP	Open Circuit Potential
SCE	Over-saturated Calomel Electrode
OCP	Oxygen Reduction Reaction
WE	Working Electrode
SCS	Standard Condition Solution
RS	Reference Sample
CPE	Constant Phase Element
RC	Capacitive Behavior
RM	Resistance of Metal Paths
M	Metal
Eq	Equation
PEMFC	Polymer Electrolyte Membrane Fuel Cell
$PEMFC_I$	PEMFC Interconnect
$PEMFC_{MI}$	PEMFC Metal Interconnect
ASR	Area-Specific Resistance
ICR	Interfacial Contact Resistance
ECP	Electrically Conductive Polymers
EEC	Equivalent Electrical Circuit
TBOT	Tetra-n-butyl Orthotitanate
TEOS	Tetraethyl Orthosilicate
HF	Hydrofluoric Acid
LbL	Layer-by-Layer
FWHM	Full Width at Half Maximum
L	Layer
d	Day
h	Hour
min	Minute
bcc	Body-Centred Cubic
ppm	Parts Per Million
M	Molar Concentration
RT	Room Temperature
CTE	Coefficients Thermal Expansion
PVD	Physical Vapor Deposition
CVD	Chemical Vapor Deposition
TFMGs	Thin-Film Metallic Glass Coatings
TFSOC	Thin-Film Solid Oxide Coatings
PEP	Potentiodynamic Electrochemical Polarization
EIS	Electrochemical Impedance Spectroscopy
TGA	Thermal Gravimetric Analysis
DTA	Differential Thermal Analysis

FT-IR	Fourier Transform Infrared Spectrum
EDS	Energy-Dispersive X-ray Spectroscopy
SEM	Scanning Electron Microscope
XRD	X-ray Diffraction

Chapter 1

Introduction to the Principles of Electrochemical Degradation

Electrochemical degradation has been discussed in this chapter as one of the most relevant problems of energy production equipment. It also includes an introduction to the principles of electrochemical degradation in different environments to identify the challenges of this phenomenon in the field of sustainable metal-based materials production. Finally, electrochemical degradation products, formation mechanism and their advantages as protective passive layers have been studied.

1.1. Electrochemical Degradation in the New Energy Technologies

The increased use of non-renewable fossil fuels, the scarcity of these resources and the environmental issues generated by their use have caused the development of alternative renewable energy sources as a source of future energy [1,2]. The potential advent of renewable and green energy in electricity generation for the future is inevitable for a variety of reasons. In addition to the solar, geothermal, biomass resources and fuel cell technology have now become very significant [3,4]. In the meantime, hydrogen is expected to provide a significant proportion of the energy supplies required for future generations due to its unique properties. In the extent that the experimental data of scientists suggest the future energy source belongs to hydrogen and its associated technology [5,6]. Proton Exchange Membrane Fuel Cell (PEMFC) technology, which transforms hydrogen into electricity and heat through a chemical reaction with oxygen, is one of the promising technologies for generating electricity due to its advantages such as high performance, environmental friendliness, high energy density, no noise and pollution [7,8]. Due to the complexities of this technology and its extensive range of applications, as well as its numerous impacts on the energy economy, environment, transport and industries, considerable attention has been given to the development, avoidance of production challenges and the affordable use of this technology [9-12]. Metallic materials are attractive candidates for use as interconnectors in PEMFC applications due to their high electrical conductivity, thermal properties and high mechanical efficiency [13,14].

However, PEMFC metal interconnections ($PEMFC_{MI}$) as much more common materials suffer from severe degradation in the harsh acidic and humid environment inside the fuel cell stack [15,16]. Subsequently, degradation attack and product formation on the surface of the metal as the most critical challenges will greatly increase the interfacial contact resistance (ICR), which gradually leads to durability problems for other parts and significantly decreased the output power from the fuel cell stack [17,18]. Therefore, investigation on developing of novel low-cost metal-based materials with excellent electrically and electrochemical degradation resistance ex-situ in a simulated cathode/anode environments or situ in a real operating PEMFC system and complementing this with long-term analysis is crucial in developing the next generation of cost-efficient, flexible and durable interconnect metal-based materials. Environmental sustainability is one of the biggest challenges and most important targets of modern technological research. Sustainable development of low-cost and renewable fuel is a critical issue for efficiently harnessing earth's energy [19,20].

To construct energy supply equipment, it is necessary to use cost-effective materials with long-term stability and reliability. Under certain conditions, the transmission and energy supply equipment must operate in a variety of conditions e.g., highly acidic, humidity and/or corrosive. This may induce electrochemical degradation and gradual deterioration of the machinery [21,22]. Electrochemical degradation of components causes a decrease in apparent device quality contributing to higher equipment repair costs and more maintenance losses for the industry [23]. Extensive researches have engaged in serious scientific to identify the new methods and materials to reducing and preventing corrosion over the past decades in pace with the growth progress of various industries [24,25]. Using the scientific principles and results of these studies in the implementations of special rules and methods for the control or prevention damages caused by this phenomenon extremely useful have been implemented and considerable progress has been achieved [26,27]. The phenomenon of electrochemical degradation is one of the major challenges in the energy generation and transmission industries.

Environmental contamination caused by leakage of fuels and lubricant leading to electrochemical destruction is of great concern owing to the presence of carcinogenic [28,29]. The explosion of new technologies and materials instead of traditional methods in addition to reducing costs and waste have improved the pace of construction and the safety of energy supply projects [30,31]. In general, the mechanism of electrochemical degradation is correlated with a variety of parameters in different environments [32]. Therefore, long-term use of devices in different conditions and environments is one of the important limitations of engineering designing and manufacturing energy production and transmission equipment in the three main dimensions of economy, safety and waste reduction [33,34]. Further, the use of innovative technologies and cost-effective materials with excellent electrochemical properties are of considerable significance due to the variety of applications and diverse environments [35,36]. In addition to the advantages of using materials resistant to electrochemical degradation, the study of electrochemical behavior, as well as the commercialization and industrialization of these materials are also important.

1.2. Definition and Examples of Electrochemical Degradation

The deterioration of materials due to reactions with their liquid or gaseous environment is the currently accepted broad definition of corrosion. From a practical point of view, the term materials refers to various materials such as ceramics, glasses, metals, polymers and composites utilized for construction within the different applications. The complexity of this interpretation can be adequately appreciated by considering some examples of corrosion instances:

- Electrochemical degradation of magnesium- [37], zinc- [38] and iron- [39] based as bioabsorbable (or biodegradable) implant materials in their corrosive service environments of isotonic solution (0.9 or 0.85 wt.% NaCl solution).
- Electrochemical degradation of different stainless steel as exhausts system of automobile due to high temperatures, corrosive exhaust gases such as water vapor,

carbon dioxide, nitrous oxides and hydrocarbons as well as high pressure inside the exhaust system [40].

- Hot electrochemical degradation of super-alloy components and their coatings under operating conditions as gas turbine blades due to the accumulation of deposits such as Na_2SO_4, NaCl with SO_x and other compounds of the alkali metals and alkaline earth metals [41].
- Electrochemical degradation of pipeline systems in the oil and gas industry due to the pH, carbon dioxide partial pressure, acetic acid, multiphase flow effect, temperature and condensation [42].
- Electrochemical degradation of different types of metals interconnects in fuel cells causing the release of various metallic ions such as Fe^{2+}/Fe^{3+}, Cr^{3+} and Cu^{2+} severely poisoning the catalyst layers and finally deteriorating the performance of the fuel cell stack [43-46].

1.2.1. The Need to Control Electrochemical Degradation

Electrochemical degradation occurs in various forms in industry and indicates a significant reduction in the value of materials that have been exposed to the direct chemical impact. In the concerns for the natural environment and the global energy infrastructure such as energy supply and transmission, it is a significant economic and safety challenge [47]. Notably, this serious problem clearly depletes our natural resources. The global electrochemical degradation costs are estimated at US$ 2.5 trillion or 3.4% of the global Gross Domestic Product (GDP) [48]. Moreover, in these costs typically neither individual safety nor environmental consequences are included [49]. Besides, the mentioned costs only relate to direct costs [50]. Indirect costs arising from the interruption of production, reduction of equipment efficiency resulting in a loss in productivity and exit from operating conditions according to plans (overhead cost of delays) are expenses that can be added to the direct costs, which might sum up to millions of dollars inflicting losses per day, which are estimated to be equal to the direct cost [51].

These stats indicate that investment decisions in the protection of materials from electrochemical degradation are, by all means, economically justified. The economy would be drastically changed if there were no electrochemical degradation and it would appear safe to say that almost everyone is at least somewhat familiar with this degradation form. It is common and varied mechanisms, which can not entirely be avoided from their associated costs but can be significantly minimized. However, the application of novel protection technologies suggests that reductions between 15% and 35% of the expense may be achieved; i.e., enormous reductions between US$ 375 and $875 billion, astronomical savings on a global basis [52]. In summary, the effective use of appropriate and novel methods of protection and control may maintain society's general health, minimize financial, human and environmental hazards and eventually save huge amounts of expenditures. Also, in consideration of the devastating effect of electrochemical degradation on metals [53], alloys [54], and equipment types [55], the emerging protective technologies may minimize natural resources over-harvesting and help support the proliferation of green energies such as fuel cells [56].

1.2.2. Basic Terminology, Reactions and Variables in Electrochemical Degradation

Different metals and alloys are corroded electrochemically due to the presence of species in the solution as an environment supporting the cathodic reaction. The primary mechanism and the simplest form of electrochemical degradation can be seen in Figure 1.1. The transition of metal atoms from the solid to the solution where they exist as ions as represented in Equation (1.1) is known as corrosion reaction [57]. It is assumed that these metal ions are separated from the metal surface at selected sites such as dislocation and grain boundaries. Then they pass through the interface and are coordinated by water molecules forming hydrate complexes [58]. Due to the continuity of this reaction on the metal surface and loss of electrons from the metal atom owing to transfer, this results in corrosion on the surface. As a result of this reaction, various forms of corrosion can occur on different types of metal. However, the presence of electrons in the solution is not freely conceivable, and so the electrons released in an oxidation

reaction must be consumed at the same time as a reduction reaction. The oxidation reaction is sustained by the consumption of the electrons in an anodic reaction (Equation 1.2) occurring on the metal surface in ranging from positions of a few atom distances up to several square meters [59]. These reactions may not be distinguishable due to proximity or even they can also move easily to change the positions [60]. In consequence, the ratio of the cathode to anode area ratio is also one of the most important factors impacting electrochemical degradation. The electrochemical degradation ratio can further depend on several factors such as O_2, Fe^{2+} and H^+ species that are related to both cathode and anode reactions or even thermodynamic driving forces or kinetic of several steps, which are generated by other constituents in the solution [61].

$M \rightarrow M^{m+} + me^-$ (Eq 1.1)

$X^{x+} + xe^- \rightarrow X$ (Eq 1.2)

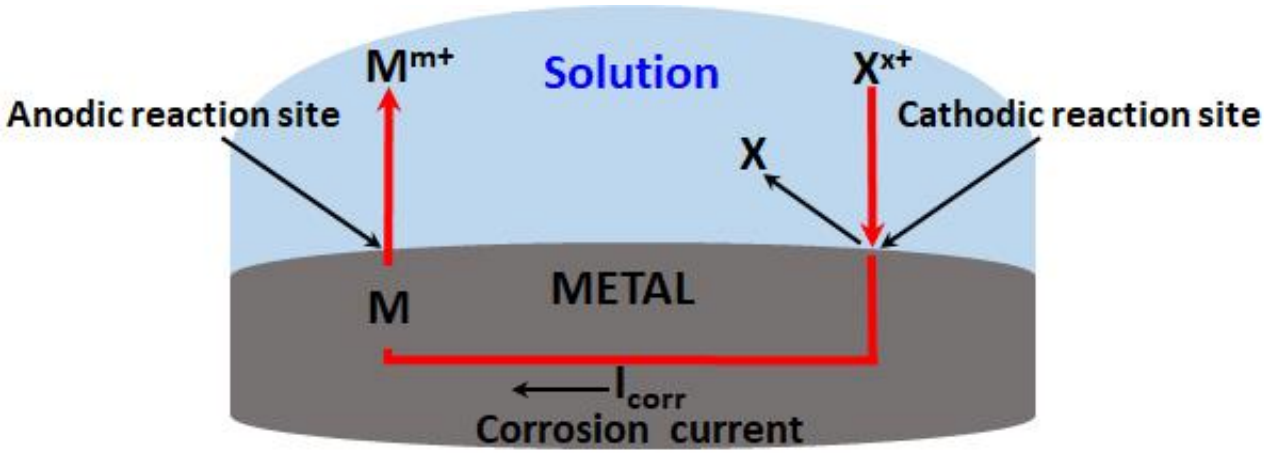

Figure 1.1. The basic electrochemical degradation process in solution.

1.3. Electrochemical Degradation Mechanisms on Metals

The variety of mechanisms whereby deterioration occurs in materials especially different types of steels is large due to the particularly broad definition of electrochemical reaction with the environment as well as the driving force that causes metals to corrode are the natural consequence of their unstable existence in the form of the metal [62,63]. Based on this assertion, it is important to know that the electrochemical degradation generally takes place at the interface of metals and environments as a significant factor, which is created via atomic,

molecular, or ionic transport process [64]. From the standpoint of the electrolytic theory [65] the explanation of this process is not difficult to comprehend, and so far has been found usually involves more than one definable step. Assuming that the rate of the overall reaction is essentially controlled by the slowest step, this rate requires to be as slow as possible to avoid continuous electrochemical degradation until catastrophic failure. Electrochemical degradation is characterized as a chemical reaction involving the transfer of electrons, so it is crucial to understand the fundamental nature of the reactions [66]. Nevertheless, these processes cannot be thoroughly analysed on the atomic scale and therefore it is appropriate to infer possible mechanisms from indirect measurements and observations [67]. For obvious reasons, measurements of electrical potential and current might infer electrochemical degradation. Zhang et al. [68] investigated the electrochemical degradation behavior of stainless steel (SS) 316L (SS316L) in pure water and boric acid solutions. Electrical potential and open circuit potential evolution (OCP) have been used to evaluate corrosion behavior at different temperatures from 50 °C to 185 °C over the long immersion time (7 days).

The corrosion rates based on the weight loss method showed that increase in the immersion time and temperature caused in enhancing the corrosion rate. They also pointed out that the rate of corrosion that has been successfully evaluated by electrical potential and OCP is changed by different solutions and immersion time. However, suggested by the work of Zhu et al. [69] the corrosion rate and pitting sensitivity increase with the alternating current, which affected the stability and protective property of the passive film on the super-duplex stainless steel in 3.5% NaCl solution. The rate of change in weight or dimensions and corrosion products in the environment as well as changes in mechanical and physical properties can also be used to evaluate electrochemical degradation. He Wei et al. [70] investigated the electrochemical degradation of medium-carbon steel via determining the weight of the sample after removal of corrosion products. The results have shown that with an increase in the content of the alloying elements the possibilities of corrosion occurrence were reduced. Samanbar et al. [71] studied

the relationship between the electrochemical degradation and physical properties of steel surface after 250 days. The surface of the steel specimens with compact and porous crevices showed indication of corrosion regardless of the level of cathodic polarization as well as in the anodic polarization case. Grain size also has a significant influence on electrochemical and physical properties. Xiaoqian Fu et al. [72] proposed a relationship between the grain size and its uniformity on corrosion resistance of SS316L. The result has shown that the grain uniformity and grain boundary intermetallic have a significant impact on the stability of passive films, which contributed to increasing the electrochemical resistance to degradation. Marta et al. [73] similar concept and result, presented the effect of grain size and grain boundary on the electrochemical response of commercially pure aluminum. However, the relationship between electrochemical degradation and several critical factors of metals such as environment, texture, residual stress, and impurity segregation is known [74]. Also, the possibility of further improving the properties of electrochemical degradation resistance by different annealing has been investigated. Low-temperature annealing offers a fast, simple and low-cost way to further enhancement of mechanical and corrosion properties, which are crucial for metals and alloys [75,76]. Besides, a model described the growth of duplex oxide such as Fe_2O_3 layers by high annealing temperature, which restricted the electrochemical degradation by the outward diffusion of metal ions along grain boundaries in the oxide [77].

1.4. The Elementary Electrochemical Degradation Circuit

Aqueous electrochemical degradation can be easily understood in terms of dead shortened batteries or electrochemical cells based on cathodic and anodic reactions, as seen schematically in Figure 1.2. Originally, net oxidation and reduction reactions occur at cathodic and anodic sites due to their inherent nature, respectively. Owing to the nature of electrochemical oxidation in different environments, these sites cannot be easily detected and separated [78]. In the electrochemical cell, the calculation of corrosion current (I_{corr}) is of fundamental importance [79]. By defining the area of the anode through, which the current flows, the rate of I_{corr} can be

determined and, as a result, valuable information can be extracted from this system. The use of current density to analyse the rate of corrosion in chemical techniques is becoming increasingly popular. According to Faraday's law [80] (Equation 1.3), I_{corr} is specifically connected to the corrosion intensity or corrosion penetration rate as essential parameters in electrochemical degradation studies.

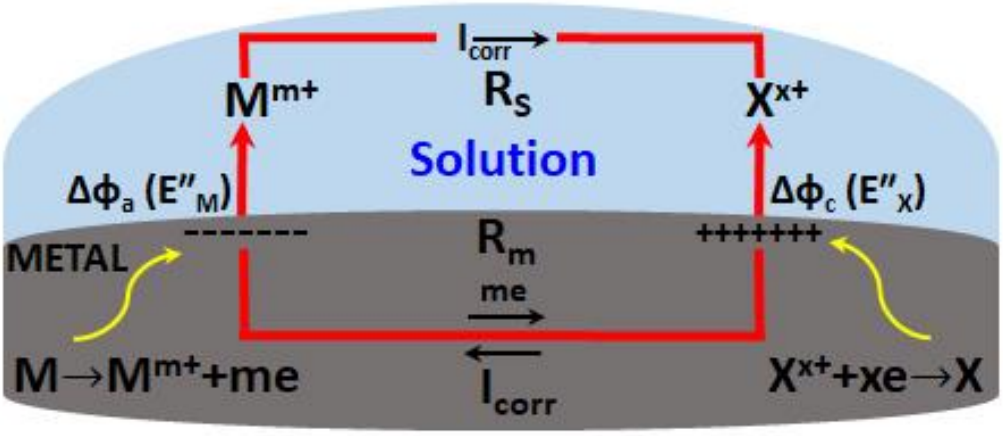

Figure 1.2. The elementary electrochemical degradation circuit.

In general, Faraday's law has been commonly used to measure the mass loss of different steel during electrochemical degradation [81]. It is also clear that the mass of weight loss can be determined by the oxidation reaction (Equation 1.1) that occurs on the metal surface during the degradation process. As schematically shown in Figure 1.3, considering a surface of the metal with the area of A_a as an anode, it is observed that the current flows (Equation 1.4) to the surface counter opposite to the electrons and finally enters the solution in the form of positive actions of the ions. As a consequence, the metal decomposes and gets lost to the solution and electrochemical degradation occurs in places where internal current flows to the metal surface or conversely. Therefore, the I_{corr} of electrochemical cells must be measured as an effective parameter to examine the corrosion behavior of metals.

$$i_{corr} = \frac{I_{corr}}{A_a} \quad \text{(Eq 1.3)}$$

$$I_{net,ox} = I_{ox,M} - I_{red,M} = I_{corr} \approx I_{ox,M} \quad \text{(Eq 1.4)}$$

Therefore, due to the transfer of ions or even electrons from the metal interface to the solution at the anodic and cathodic sites the differences electrical potentials, $\Delta\phi a$ and $\Delta\phi c$ occur according to the Equations (1.5) and (1.6), respectively [82]. M and S subscripts are designate the metal and solution phases, respectively.

$$\Delta\phi_a = \phi_{M,a} - \phi_{S,a} \quad \text{(Eq 1.5)}$$

$$\Delta\phi_c = \phi_{M,c} - \phi_{S,c} \quad \text{(Eq 1.6)}$$

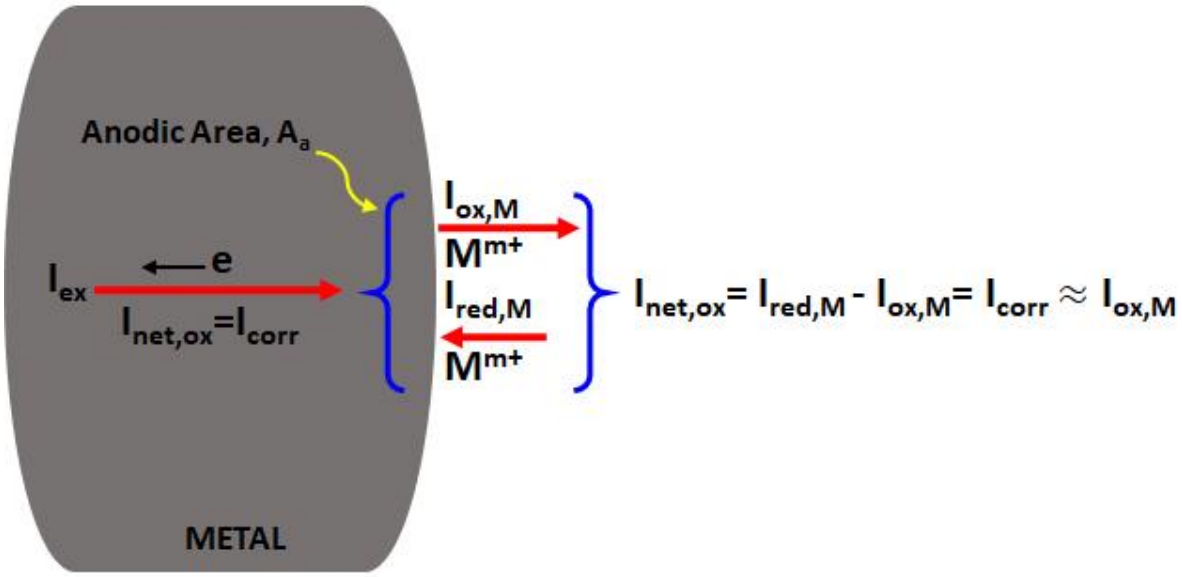

Figure 1.3. Ionic and electronic current components flow of the metal surface referenced in the derivation of Faraday's law.

As a result, the flow of electrons from the anodic to the cathodic site in the metal due to these potential differences constitute an electrochemical cell. As can be seen, due to the higher potential above of anode solution compared to the cathode $\phi_{S,a} > \phi_{S,c}$ the current flows from the anodic to the cathodic site. As a result, this current can be defined as a positive quantity. As can be seen in Figure 1.2, the potential difference between the anode and cathode reactions when the current passing the interface is defined by E''_M and E''_X, respectively ($E''_M = E''_X$). Therefore, in this case, the driving potential ($\Delta\phi_s$) for the current in the solution can be:

$$\Delta\phi_S = \phi_{S,a} - \phi_{S,c} = \left(\phi_{M,a} - \Delta\phi_a\right) - \left(\phi_{S,c} - \phi_c\right) \quad \text{(Eq 1.7)}$$

Also, the potential difference in metals is very small ($\phi_{M,a} \approx \phi_{M,c}$) because in different conditions are of low electrical resistance. As a result, the driving potential for the solution current with Equation (1.7) is as follows:

$$\Delta\phi_S = \Delta\phi_c - \Delta\phi_a = E''_X - E''_M \quad \text{(Eq 1.8)}$$

Also, using Ohm's law (Equation 1.9) with I as a current, V as a voltage and R as a resistance states that the current through a conductor between two points is directly proportional to the voltage across the two points.

$$V = IR \quad \text{(Eq 1.9)}$$

Since the values of E''_X and E''_M relate to the corrosion current of the electrochemical cell and recognizing that Ohm's law must apply and the current through a conductor between two points is directly proportional to the voltage across the two points, the corrosion current based on the Ohm's law is:

$$I_{corr} = E''_X - E''_M/(R_S + R_M) \quad \text{(Eq 1.10)}$$

By consideration the area of the anode through, which the current flows the rate of corrosion penetration can be calculated with the help of R_S and R_M as a resistance of the solution and metal paths, respectively.

1.5. Electrochemical Degradation Processes and Variables

Before examining in detail the electrochemical degradation theories and their quantitative calculation bases, it may be useful to identify the effects of the different environments in order to develop qualitatively and use the new protective techniques. Transport of mass across the surface to the environment as oscillations can generally be considered as an electrochemical reaction in engineering materials such as metals. Steady-state and dynamic behavior such as simple and complex periodical oscillation, quasi-periodicity and chaos might well be demonstrated by chemical reaction systems [83]. Since electrochemical degradation causes the release of metal ions to the environment and electron movement is necessary within the material, this mechanism can occur only if the environment can contain ions and the material

can conduct electrons [84]. The most important case of electrochemical degeneration is the simple degeneration of metals in aqueous solutions that most commonly occur as rust, which forms on the surface of the metals. In this mechanism, metal atoms arising from electron and ions can migrate away via space between the metal interfaces to the solution. To sustain the reaction, these ions are simultaneously consumed by species in the contact with the metal surface [85]. In more complicated cases, at sufficiently high temperatures the precipitate compounds such as hydroxides and oxides can be formed by moving metal ions into solution by forming complex ions and combining with other species in the solution [86,87]. The following sections review the general types of metal and corrosive environment combinations, the chemical reactions involved, idealized mechanisms for transition metal ions to the environment, and the electrochemical processes occurring at the interface between the metal and the aqueous environment.

1.5.1. Electrochemical Degradation With pH and Dissolved Oxygen as Variables

The occurrence of an electrochemical degradation is defined as a chemical reaction involving the transfer of electrons. The most straightforward corrosion reactions for metals (M), which seem to be thermodynamically unstable in water are generally assumed as Equations (1.11) and (1.12). Thus, the chemical reaction, which involves oxidation and reduction with transfers of electrons, the metal passes from the metallic state to ions of valence m in solution with the evolution of hydrogen, which is occurring in the metal interface and solution [88]. The hydrogen ions reaction in the acid solution is considered directly related to the increased concentration of the hydrogen ions in the corrosion medium. Progressively it is considered at higher pH and to neutral and alkaline conditions with water molecules. Therefore it can be concluded that the system can show different behaviors depending on the medium [89]. In general, two processes are involved in the electrochemical reaction: M to M^{m+} that is performed in all reactions and mH^+ to $m/2H_2$ in acidic solution, both involving a change in charge. The changes in charge are accomplished by electron transfer from M to H^+.

Since the metal phase is the electron conductor, it acts as an electron carrier and enables the above-mentioned two processes to be performed separately on the metal surface [90]. As a consequence, these processes occur in positions with atomic sizes, which continuously change over time, resulting in uniform surface corrosion, which is represented schematically in Figure 1.4. [91].

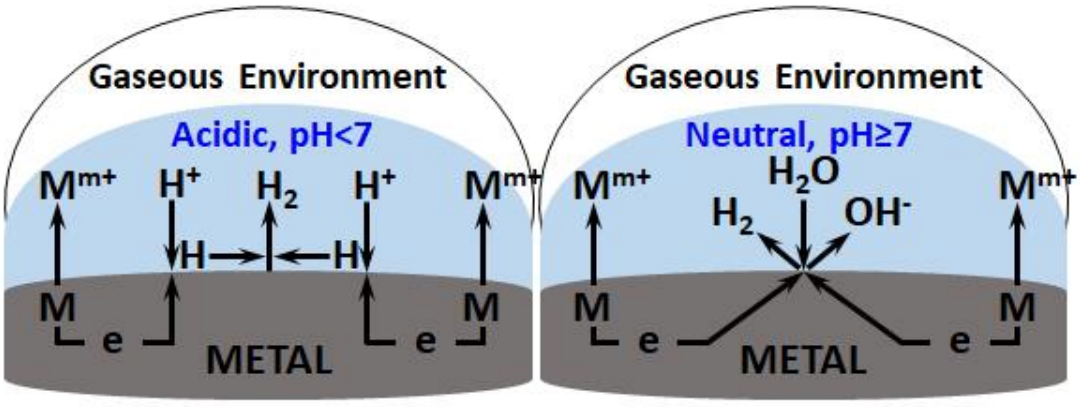

Figure 1.4. Electrochemical degradation supported by different controlled pH values.

In addition to the aforementioned reactions, when dissolved oxygen is present in the solution, however, the following reactions as Equations (1.13) and (1.14) might occur due to the presence of oxygen, which is represented schematically in Figure 1.5. Because two reactions consumed the electrons in this situation, the metals corrosion rate can also increase compared to the other conditions. Therefore, it can be concluded that metals can have different electrochemical behavior due to the pH of the solution, surface composition and etc. in different environments. For this reason, it is important to study and evaluate the mechanism of electrochemical degradation to find different protective methods against corrosive metals due to their environmental service.

$$M + mH^+ \rightarrow M^{m+} + \frac{m}{2}H_2 \qquad \text{at pH} < 7 \quad \text{(Eq 1.11)}$$

$$M + mH_2O \rightarrow M^{m+} + mOH^- + \frac{m}{2}H_2 \quad \text{at pH} \geq 7 \quad \text{(Eq 1.12)}$$

$$M + \frac{m}{4}O_2 + mH^+ \rightarrow M^{m+} + \frac{m}{2}H_2O \quad \text{at pH} < 7 \quad \text{(Eq 1.13)}$$

$$M + \frac{m}{4}O_2 + \frac{m}{2}H_2O \rightarrow M^{m+} + mOH^- \quad \text{at pH} \geq 7 \quad \text{(Eq 1.14)}$$

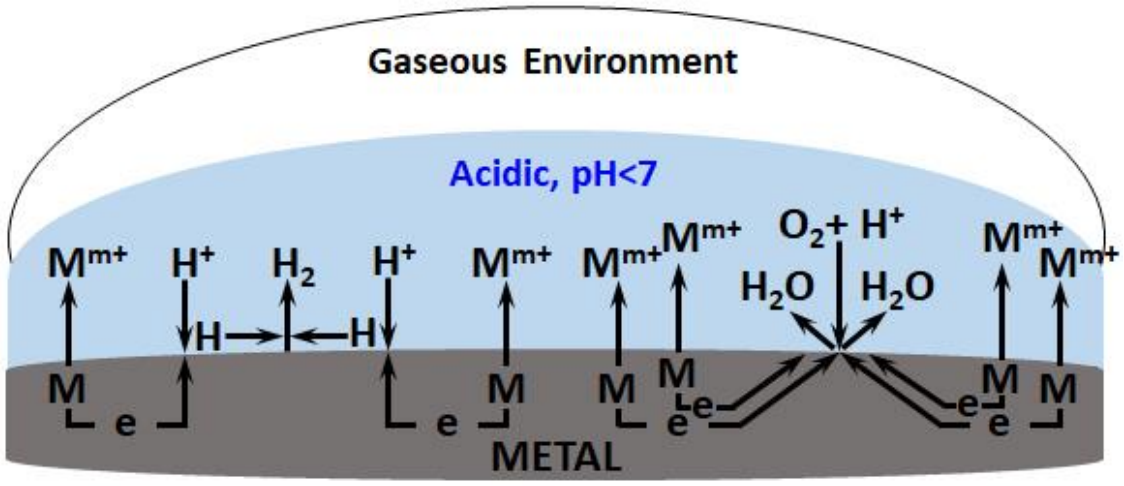

Figure 1.5. Electrochemical degradation supported by controlled pH in acid with pH < 7.

1.5.2. Solid Corrosion-Product Formation: Corrosion Acceleration versus Passivation

Metal rusting is a clear example of the formation of corrosion products as described in Figure 1.6 [92]. Under low pH conditions, the Fe_3O_4 in black and $Fe(OH)_2$ may form on the surface of the metal [93]. Most remarkably, oxygen is a highly reactive element that can spontaneously oxidize different types of metals. Therefore, red oxide iron such as Fe_2O_3 and FeO(OH) also can be formed in the presence of oxygen and water, which are generally known as significant causes of metal corrosion. As seen schematically in Figure 1.7, the process of formation of oxides harmful such as Fe_2O_3 under a wet-dry cyclic condition, which contributes to further corrosion of the metal surface is somewhat similar to galvanic electrochemical cell [94]. As can be seen, the oxidation-reduction cycle occurs by oxidation (anodic site) and reduction (cathodic site) half cycles in two different parts of the same metal surface. The anodic site is where the concentration of oxygen is low and the cathodic site typically forms where the oxygen concentration is high. According to Equation (1.15), various metals are oxidized with the loss of electrons under conditions of continuous moisture saturation. During this process, the metal atoms at the site of the anode release electrons and flow through the metal (as an electronic conductor or internal circuit) to the cathode site. Therefore, the cathodic half-cycle

reaction occurs in the cathodic site as shown in Equation (1.16). At the same time as electrons are transferred from the anode to the cathode in the metal, the Fe^{2+}(aq) ions arising from the anodic half-cycle also flow to the cathodic site through water droplets on the metal surface resulting in the formation of $Fe(OH)_2$(s) precipitate rust deposits as shown in Equation (1.17) on the metal surface in the forms of either the soluble ferrous iron or the insoluble ferric iron. The water droplets are known as a super-ionic conductor or external circuit due to the high and fast transmits of ions. As result, the $Fe(OH)_2$(s) is oxidized by oxygen and water to $Fe(OH)_3$(s) precipitate, which is generally assumed as Equation (1.18). Finally, as shown in Equation (1.19) the $Fe(OH)_3$ is decomposed to form iron (III) oxide-hydroxide or ferric oxyhydroxide as a result of the removal of residual water.

$$Fe(s) \rightarrow Fe^{2+}(aq) + 2e^{-} \quad \text{(Eq 1.15)}$$

$$O_2(g) + 2H_2O(l) + 4e^{-} \rightarrow 4OH^{-} \quad \text{(Eq 1.16)}$$

$$Fe^{2+}(aq) + 2OH^{-}(aq) \rightarrow Fe(OH)_2(s) \quad \text{(Eq 1.17)}$$

$$4Fe(OH)_2(s) + O_2(g) + 2H_2O(l) \rightarrow 4Fe(OH)_3(s) \quad \text{(Eq 1.18)}$$

$$4Fe(OH)_3(s) \rightarrow 2(Fe_2O_3.3H_2O)(s) \quad \text{(Eq 1.19)}$$

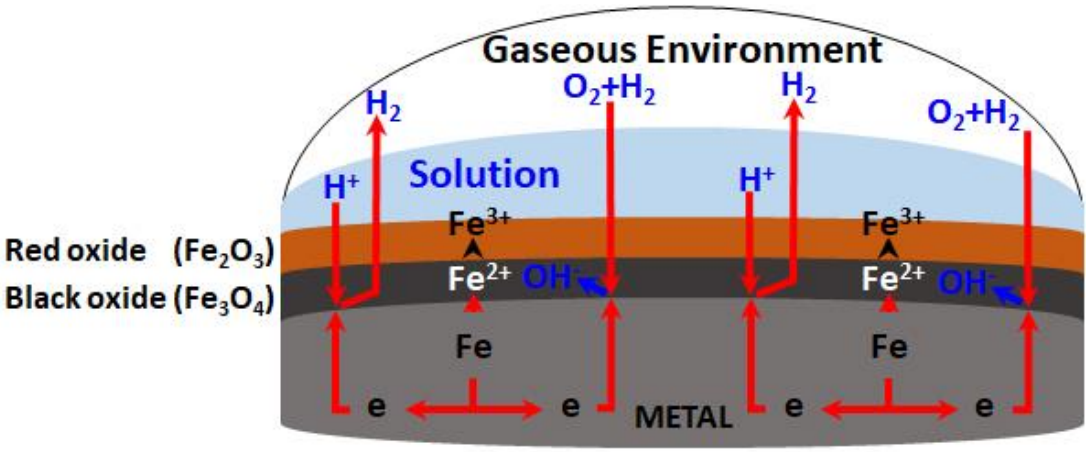

Figure 1.6. Electrochemical degradation with solid corrosion product deposit.

Therefore, it can be concluded that those metal surfaces that form a more porous oxide such as iron (III) oxide-hydroxide as harmful iron rust or worse, which are generally converted to soluble species under a wet-dry cyclic environment may result in a continuous loss of metal surface and electrochemical degradation can ultimately lead to metal failure [95,96]. However, it has also been shown that the formation of such layers of corrosion products due to the introduction of barriers against the diffusion of ions and oxygen into the metal influences the corrosion process and reduces the rate of corrosion [97]. The formation of these solid corrosion products can be a significant factor in corrosion control and consequently can have strong contributions to the improvement of the economic performance of equipment. These products are formed when the concentration of metal ions passing into the solution reaches a critical concentration, i.e. the surface corrosion rate is initially high. Since at the metal-solution interface, the metal ion concentration is the highest, it can be concluded that the precipitate appears to form on or near the metal surface [98]. If these precipitates do not adhere to the surface of the metal and their solubility is very low and due to the continuous removal of these ions from the solution the concentration of metal ions will remain at a low value and the corrosion rate may increase as a result.

However, if these products adhere to the metal surface in the form of continuous and nonporous layers or films, the corrosion rate is greatly decreased due to the avoidance of ion diffusion. Therefore, a complex mixture of these products with corrosion-resistant solid oxides such as titanium and silicon can be an intelligent solution for the use of these solid corrosion products to control electrochemical degradation using cost-effective methods to form non-porous films on the steel surface. Extensive research has been carried out on the formation of thin-film by these products with the mentioned oxides (cf. Chapter 3 and 4) in order to increase the resistance of electrochemical degradation of different steels as substrate. It has also been shown that if the combination of these products with different films is low in terms of electrical

conductivity, the resistance against electrochemical degradation will increase as a result of the difficulty of electrons to reach the solution interface to perform cathodic reactions [99].

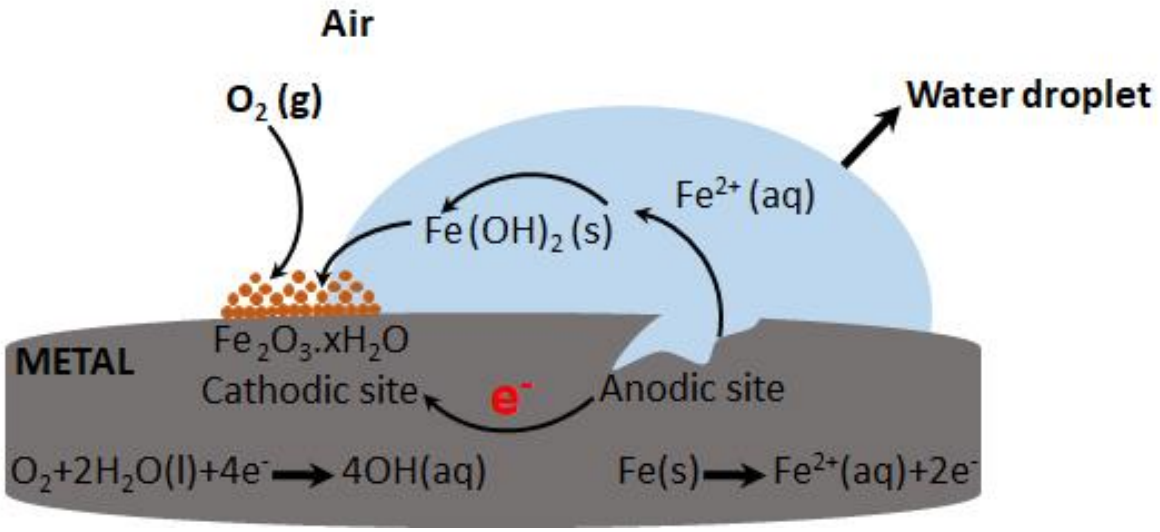

Figure 1.7. Basic electrochemical degradation process of metal under wet-dry cyclic condition.

1.6. Summary of Literature and Overview of Electrochemical Degradation

The economic significance of electrochemical degradation control was examined. It has also been found that this phenomenon plays a major role in the industries economic losses and the environment. Processes involved in the corrosion of metal as an important engineering material in various solutions have been reviewed and it has been observed that this phenomenon shows different behavior under the influence of pH as one of the main parameters as well as ambient temperature. The different steps and the mechanism of electrochemical degradation in aqueous solutions were investigated and it has been shown that the effect of various physical and chemical factors such as penetration and electrical conductivity may affect the behavior of electrochemical cells. It has also been shown that the formation of insoluble corrosion products under certain circumstances may increase and, eventually, reduce the corrosion rate with a mechanism comparable to cost-effective protective coatings. It was also concluded that it may not be possible to separate anodic and cathodic areas in the electrochemical metal system due to fast and extreme degradation. Furthermore, the electrochemical cell analysis showed that the corrosion current is essentially the most important factor in the investigation of the metal degradation rate in aqueous environments. It has also been demonstrated that most metals have the potential to be passivated, which may significantly control electrochemical deterioration over a long period.

Chapter 2

Introduction of Polymer Electrolyte Membrane Fuel Cell and their Interconnects

In this chapter, the PEMFC has been considered as one of the most significant developments for green energy production. It also includes an introduction incorporating the background knowledge and principles of polymer electrolyte membrane fuel cell to recognize the challenges of these technologies in the field of sustainable energy development. Finally, the structure, operation mode and advantages of these types of fuel cells have been studied.

2.1. Introduction of Fuel Cell

Humans have gone through different periods in terms of energy resources. The discovery of oil and the recognition of its benefits especially in transport industries have gradually caused a rapid development and transformation in the oil industries [100]. According to life-cycle energy consumption, most of the energy needed by humans was supplied from crude oil and its derivatives. However, as a result of oil combustion, greenhouse gasses such as carbon dioxide are released, which would melt the ice and gradually increase the temperature of the planet [101]. For understandable reasons, however, the use of fossil fuels has intensified environmental pollution and the greenhouse effect has affected humans and animals alike.

As a result, due to environmental concerns such as global warming, population growth rate, technological advances as well as the gradual depletion of the world's oil resources the use of renewable energy sources has been considered [102]. One of the cost-effective resources that would be a viable alternative to fossil fuels is hydrogen, which is used in a fuel cell that converts chemical energy to electrical energy [103]. Considering the advantages of hydrogen over other fuels such as green, renewable, zero-emission, it can be argued that hydrogen energy and its technology is the solution for the huge present and future energy requirements as a new energy era [104]. A fuel cell is a system that transforms chemical energy directly to electrical energy and it was first invented by William Grove in 1839 [105]. In a fuel cell system, the reactants enter the cell continuously and the products are constantly exiting [106]. As a result, the fuel cell can operate continuously with almost zero pollutants and greenhouse gases without moving any mechanical parts since all operations in a fuel cell system are controlled by the diffusion

of reactants and products. It is also highly efficient since the conversion of energy actually occurs directly.

2.2. Technologies and Types of Fuel Cells

Although the fuel cells have the same components and functionality as the green power generation system, they are different in several respects. A fuel cell is an energy generator device that is theoretically able to generate electrical energy as long as the oxidizing agent and fuel are supplied to its electrodes [107]. Nonetheless, electrochemical degradation and malfunction of the components reduce the working life of the fuel cell [108]. Various types of fuel cells are at different steps of development that can be categorized according to fuel type, fuel converter, oxidizing agent, generator, the electrolyte types and operating temperature [109]. Such various types of fuel cells operate somewhat differently from each other but generally consist of three main components: a cathode, an anode and the electrolyte or membrane [110]. The most common classification of the fuel cells is according to the type of electrolyte and temperature operation. Fuel cells are typically categorized into the following types depending on the type of electrolyte and fuel which determine the electrodes reactions are [111-116]:

- Alkaline fuel cell (AFC)
- Direct methanol fuel cell (DMFC)
- Molten carbon fuel cell (MCFC)
- Phosphoric acid fuel cell (PAFC)
- Proton Exchange Membrane Fuel Cell (PEMFC)
- Solid oxide fuel cell (SOFC)

On the other hand, the commonly available fuel cells which could be classified according to operating temperature are shown schematically in Figure 2.1. All of these types of fuel cells have advantages and challenges that allow them to be used in a specific field. While it is not complicated to describe how a fuel cell operates, it is difficult to develop a low-cost, efficient and reliable fuel cell [117]. For example, as a major disadvantage to using fuel cells as electrical sources, the electrical energy produced by a single fuel cell is only appropriate for small-scale

applications, therefore, several individual fuel cells are typically combined in series to form a fuel cell stack in order to achieve adequate operational power output [118].

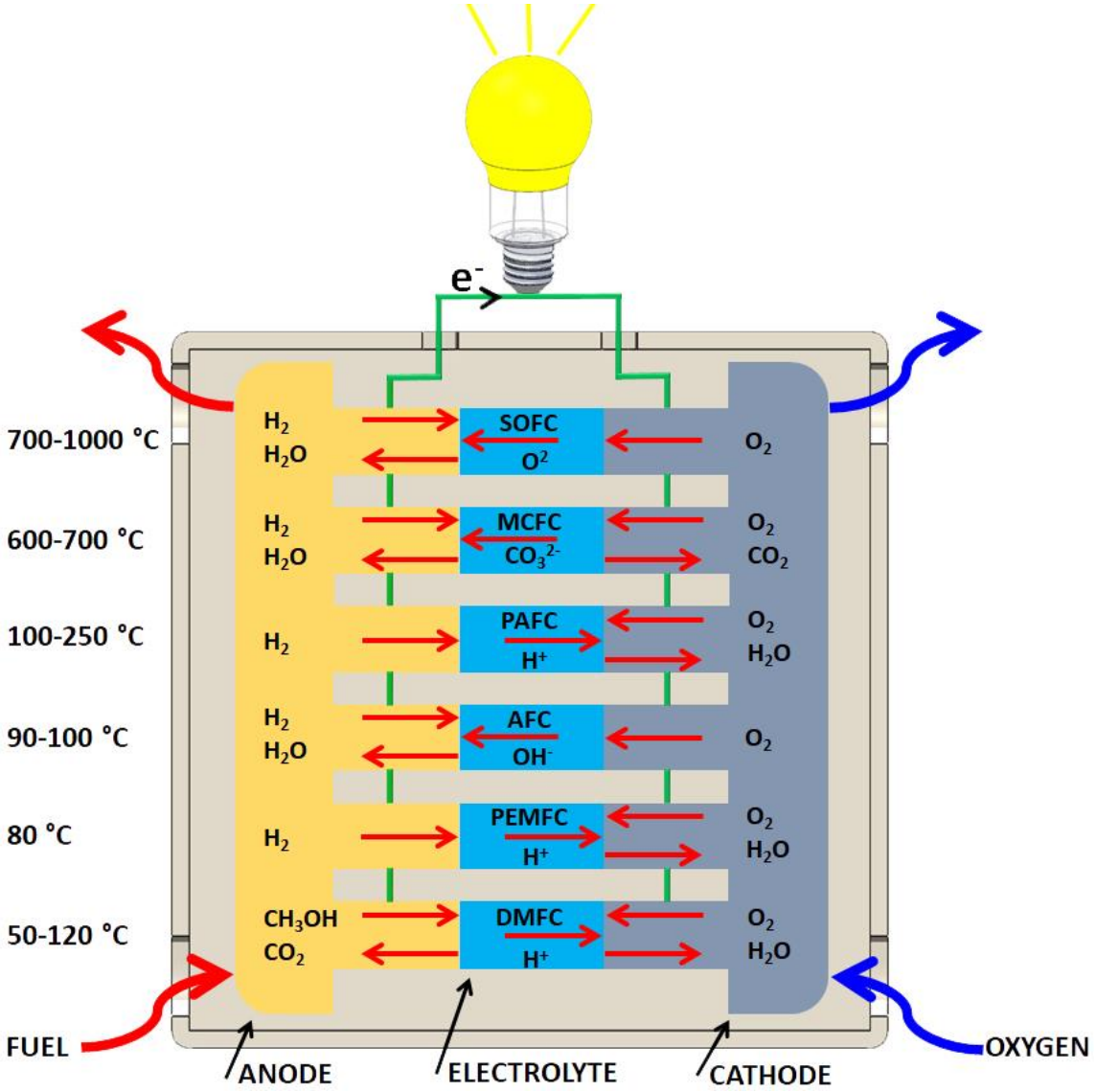

Figure 2.1. Principal types of fuel cells by temperature and their electrochemical reactions.

2.3. Proton Exchange Membrane Fuel Cell (PEMFC)

PEMFCs have attracted significant attention due to their lightweight, relatively easy maintenance, low-temperature operation and high power density [119]. Owing to the increasing need for clean energy, the PEMFC is expected to play a major role in the energy economy aiming for a green energy future [120]. PEMFCs are promising energy conversion devices to meet the threats from chemical pollution with long term environmental benefits for the planet, as well as to adapt to the growing energy demand as a safe and effective technology [121]. The most important advantage of PEMFC over other energy conversion devices is that the cell

generates electricity through a chemical reaction with a high power density, low in weight, start quickly as well as low-temperature operations (less warm-up time) [122]. Therefore, it can be concluded that the PEMFC has no thermodynamic constraints of energy conversion on the Carnot cycle [123]. As a result, the PEMFC can extract more efficiently and effectively energy from the fuel. Furthermore, heat dissipation from the fuel cell can be controlled and used to increase system efficiency to preserve the temperature for the chemical reaction [124]. PEMFC is considered a fuel cell of choice for different industrial applications due to its low operating temperature between 80 °C and 200 °C [125]. A graphical representation of PMFCs illustrating essential components is shown in Figure 2.2. As can be seen, the PEMFC stack assembly consists of anode, electrolyte and cathode with the membranes (Nafion®), gas diffusion and catalyst layers in series with interconnectors which are sealed with endplates [126].

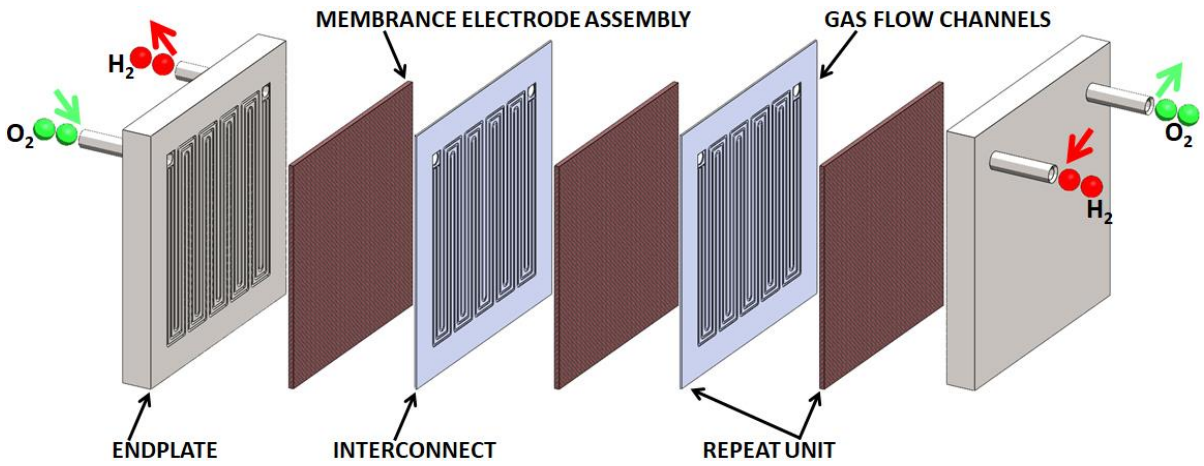

Figure 2.2. Schematic diagram of a PEMFC with its main components.

It can be seen in Figure 2.3 that the anode side with the negative electrode of the fuel cell is fed with hydrogen gas, whereas the oxygen or air reaches the cathode side of the cell with the positive electrode to distribute oxidant to the surface [127]. As the transport medium of hydrogen ions, the electrolyte membrane is employed. The platinum catalyst is utilized to split the fuel and oxidant at the anode and cathode interface, respectively [128]. Thanks to the use of hydrogen, water is only generated as a by-product in the entire energy conversion cycle of PEMFC, which is of great significance for renewable energy that can be accepted as a

replacement for fossil fuels [129]. The efficiency range of PEMFC is from 40% to 50% with a maximum power output up of 200 kW, which is suitable for a variety of applications [130].

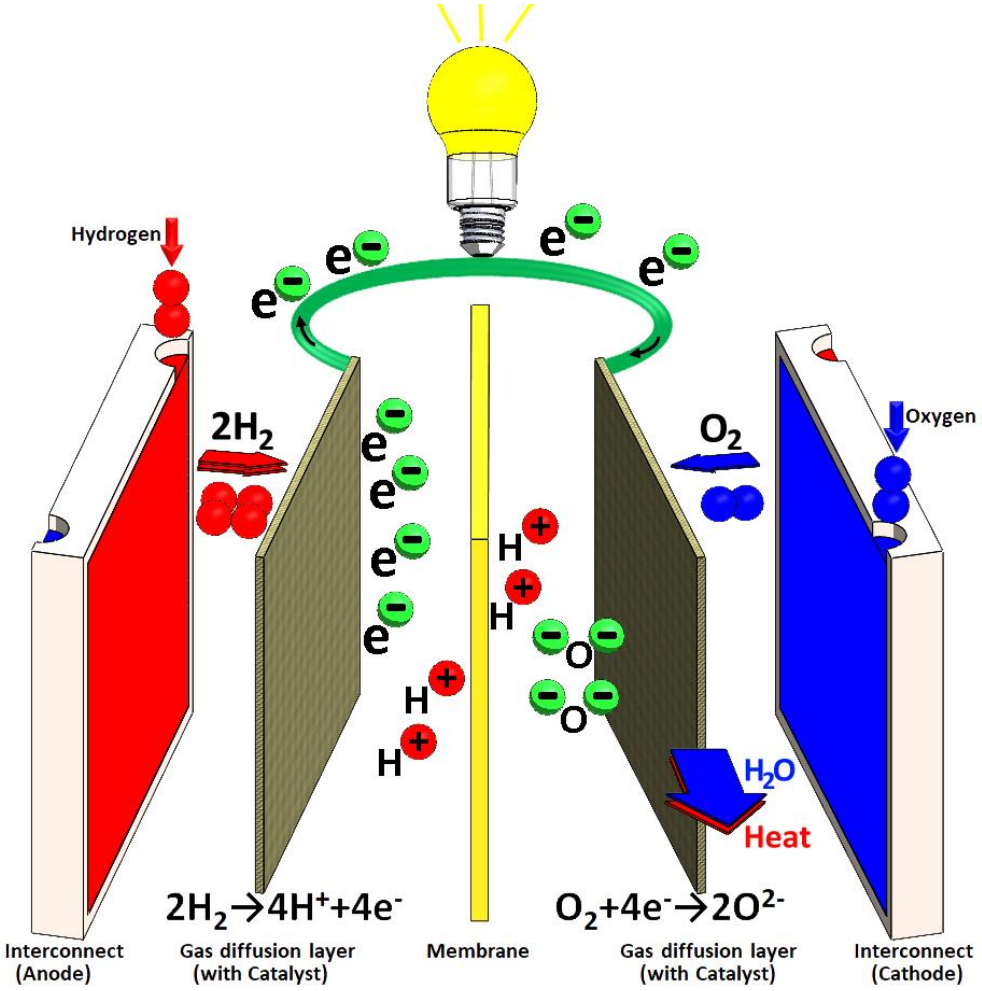

Figure 2.3. Typical construction of single-layer PEMFC components.

2.3.1. PEMFC Basic Chemistry and Mode of Operation

As described previously, PEMFC is an electrochemical system that transforms hydrogen and oxygen into electricity and water is released as a by-product at low operating temperatures. However, the PEMFC system encounters a variety of technical challenges, such as the control of water in the gas channels, the supply of oxygen and the high sensitivity to impurities which eventually cause electrochemical degradation [131,132]. A key component of PEMFC is the membrane, which allows the protons to pass through while the electrons are routed into an external circuit [133]. In the next step, hydrogen is split (oxidized) at the anode/electrode interface into protons and electrons according to Equation (1). Subsequently, the protons and

electrons travel through the supply routes to the cathode site via the electrolyte and interconnect, respectively, where the protons and electrons are consumed with oxygen to form water as can be seen in Equation (2). Finally, this oxygen reduction reaction (ORR) kinetics occurring simultaneously on both sides of the anode and cathode membrane to form the overall reaction as given in Equation (3).

$$H_2 \rightarrow 2H^+ + 2e^- \qquad \text{(Eq 2.1)}$$

$$\frac{1}{2}O_2 + 2H^+ + 2e^- \rightarrow H_2O \qquad \text{(Eq 2.2)}$$

$$H_2 + \frac{1}{2}O_2 \rightarrow H_2O \qquad \text{(Eq 2.3)}$$

In addition to other operational parameters to losses within the cell, the thermodynamic voltage (E_{thermo}) can also negatively affect the PEMFC output power. In other words, the output voltage of PEMFC depends on electrode potential difference between the anode and cathode, which is known as E_{thermo} or cell potential [134]. The overall reaction of the water formation (one mole of H_2O) can be obtained by combining one mole of H_2 and a half mole of O_2. Therefore, the theoretical estimation of E_{thermo} from this overall reaction as one of the most significant parameters on the performance of the PEMFC output power is required. Therefore, as given by Equation (2.4) and Equation (2.5) the measurement of the Gibbs free energy (ΔG) of water under the standard condition (25 °C and 1 atm) using pure H_2 and O_2 gasses could be used efficiently for the analysis of E_{thermo} [135].

$$\Delta G = \Delta G \text{ of products} - \Delta G \text{ of reactants} \qquad \text{(Eq 2.4)}$$

$$\Delta G = \Delta G^0 - RT \ln\left(\frac{a_{H_2} \times {a_{O_2}}^{\frac{1}{2}}}{a_{H_2O}}\right) \qquad \text{(Eq 2.5)}$$

Where ΔG^0 is a standard Gibbs free energy of the overall reaction (Equation (2.3)), R is the gas constant of 8.314 J mol^{-1} K^{-1}, T is the temperature in Kelvin (K) and the $a_{H_2}, a_{O_2}, a_{H_2O}$ are activities of H_2, O_2 and H_2O, respectively. Theoretically, it can be assumed that all of ΔG^0 is transformed into electrical energy if there are no losses in the PEMFC system [136]. However, when the reaction occurs in a single cell, all reactants are involved and the theoretical E_{thermo}value of 1.229 V can be determined under the standard condition from the free energy of Gibbs as given by Equation (2.6).

$$E_{thermo} = \frac{-\Delta G^0}{n.F} \quad \text{(Eq 2.6)}$$

Where $n = 2$ is the number of moles of electrons transferred during cell reaction and F=6.23×10^{23} is the Faraday constant. However, due to cell overpotential (η) and irreversible losses such as activation (η_{act}), ohmic (η_{ohmic}) and concentration (η_{conc}) the output potential (V) of the operation PEMFC is indeed lower than the E_{thermo} [137]. Therefore, it can be concluded that due to the different phenomena the operating cell voltage (E) is a number of losses extracted from the reversible theoretical fuel cell voltage as specified by the Nernst equation (Equation (2.7)) [138]. Where E_{rev} is a reversible voltage and E_{irrev} is an irreversible voltage loss. Therefore, owing to measuring the error of actual voltage the output voltages (V) of the PEMFC stack can be expressed by Equation (2.8).

$$E = E_{rev} - E_{irrev} \quad \text{(Eq 2.7)}$$

$$V = E_{thermo} - \eta_{act} - \eta_{ohmic} - \eta_{conc} \quad \text{(Eq 2.8)}$$

Among all these factors, η_{ohmic} has a significant effect on the V, which can be caused by PEMFC stack resistance such as electrical and electrochemical degradation resistance of the interconnectors [139]. These losses can be seen in a full range of currents in the PEMFC stack due to resistance to ion flow in the electrolyte and electron flow through electrode materials which are directly related to the property of the interconnector. Since the ionic flow in the

electrolyte obeys the law of Ohm and is directly proportional to the current, the equation can be expressed as Equation (2.9) [140]. Where the ASR is an area-specific resistance per unit of ($\Omega\ cm^2$).

$$\eta_{ohmic} = j \times (ASR_{ohmic}) \quad (Eq\ 2.9)$$

As described before, several PEMFCs are connected in series to meet the voltage requirements for industrial applications. This requires interconnectors to connect single cells and build up stacks. The specific properties and functions of interconnects also known as bipolar plates will be described in the following sections.

2.4. Introduction of PEMFC Interconnectors

The interconnector is a key component of PEMFC since it allows the connection of the cathode of a single cell with the anode of the adjacent cell forming a stack [141]. The material and manufacturing of this important component make up a significant fraction of the cost and weight of the PEMFC stack. The interconnectors accounting for more than 80% of total stack weight and a very significant portion of about 45% of the total PEMFC stack costs [142]. The placement of interconnects in PEMFC stacks is displayed in Figure 2.2. As can be seen, the gas and water flow channels are machined or stamped directly on the surface of the interconnector. Due to the presence of these interspaces as channels for inlet and exit of the reactant gases in the corrosive environment that are responsible for the homogeneous delivery and distribution of fuels, as well as the natural chemically/electrochemically reactions of metals with corrosive medium to form a stable compound, a significant portion of the η_{ohmic} from interfacial contact resistance (ICR) of approximately 11% happens in the cell system, which reduces PEMFC efficiency [143]. Therefore, in order to improve the efficiency and commercialization of PEMFCs, environmentally-friendly, quick and cost-effectiveness techniques such as surface modification and protective coatings are essential for understanding and modifying electrochemical degradation of interconnectors.

2.4.1. PEMFC Interconnector Features and Requirements

The reduction in volume and weight and, consequently, the overall cost of the PEMFC are considered to be the main motivation for the research on interconnections. In general, interconnects are an electrical connection between a single cell cathode and an anode of the adjacent cell in a PEMFC stack to satisfy a certain voltage requirement [144]. These interconnectors are designed to perform several functions, such as separates physically the two adjacent cells, supply and disperse fuel gas and oxygen uniformly within the active PEMFC surface by gas flow channels [145]. As a multi-functional component, it avoids leakage of reactants and coolant via control and management of heat and water transfer within the cell in addition to ultimately provide electrical connections from the cathode of one cell to the anode of the next cell [146,147]. Finally, it provides the structural integrity of the stack between the Nafion membranes and electrodes [148]. The most severe requirements for PEMFC apply to the interconnection that should follow the standards set out in Table 2.1 by the United States Department of Energy (DOE) to execute the above-mentioned multi-functions [149,150]. As presented above the most important performance indicating parameters for a PEMFC interconnector are interfacial contact resistance or have good electrical conductivity, high resistance to electrochemical degradation and suitable mechanical strength with acceptable cost and lightweight for materials and processes.

Table 2.1. DOE technical targets for PEMFC interconnect.

Characteristic	***Value***	***Units***
Density	<5	g cm^{-3}
ICR	<10	mΩ cm^2
Electrical Conductivity	>100	S cm^{-1}
Flexural Strength	>60	Mpa
Corrosion Rate	<1	μA cm^2
Stack Weight	at least	g $(kw)^{-1}$
Stack Volume	at least	cm^3 $(kw)^{-1}$
Stack Cost	<3	\$ $(kW)^{-1}$

2.4.2. PEMFC Interconnect Materials

Main materials for PEMFC interconnector are generally falling into two categories, which include non-metallic materials such as graphite or polymer-based composites and metallic materials such as stainless steel, aluminum, titanium and copper. A high-density graphite plate has historically been used to manufacture interconnect because of its intrinsic electrical conductivity and excellent resistance to electrochemical degradation in the aggressive PEMFC environment [151]. However, owing to its molecular composition as high-molecular-weight materials, the graphite interconnects not only has poor mechanical properties but also is a difficult material to machine the gas flow field channels which are adding manufacturing costs [152]. Recently, to achieve high electrical conductivity with sufficient mechanical strength as known as disadvantages of graphite interconnect various types of graphite-filled polymer were developed as high-performance composite interconnecting materials [153,154]. Carbon-based composites PEMFC interconnect are generally made from various fillers and polymer-matrix which satisfies the properties of DOE criteria [155]. Graphite composites in a polymeric matrix as a PEMFC interconnect has increased mechanical stability and fracture toughness [156]. However, due to the high electric resistance of the polymer matrix, the filler is required to attain adequate electrical conductivity, this high loading can lead to brittleness and cracking [157]. In consideration of the disadvantages of graphite and its composite with various forms of polymer, there are clear technological and economic benefits of replacing conventional graphite and their matrix with metals as appropriate material for PEMFC interconnect [158,159]. The possibility to satisfy PEMFC interconnector requirements has been shown in metallic materials with a reasonable electric conductivity, formability and machinability, gas permeability and excellent mechanical properties [160]. The low density and reasonable mechanical properties of the metallic interconnect have demonstrated the potential for transport applications as they are exposed to shock and vibration. As a consequence, effective inhibitory action to avoid cracks and leakage of the reactant gas is also an important advantage of the

metallic interconnection [161]. Compared to graphite, metallic materials have a comparatively low cost with good electrical properties and simplicity of machining which can be easily manufactured by stamping in large quantities [162]. Therefore, stainless steel (SS), titanium and aluminum alloys are commonly studied as basic materials for PEMFC interconnecting due to their unique properties [163]. In addition to the qualities of metals mentioned here, stainless steel is a popular option to use as PEMFC interconnection because of its features such as good degradation resistance, excellent interfacial conductivity, good mechanical properties, flexural strength, high hardness, low residual stress, abundance, lower cost and range of alloying options [164]. Various types of stainless steels, including austenitic, ferric, martensitic and other grades can be used with a lower thickness compared to graphite, which achieves a higher power density and decreases the weight and volume of the PEMFC interconnector [165,166]. As stated in Section 2.4.1, the necessary parameters required for interconnect materials are closely interlinked with each other, and the identification and selection of the material that satisfies all the criteria are exceedingly difficult. Graphite is brittle and porous with low gas impermeability has a high-cost, which makes it difficult to meet the criteria for manufacturing. While carbon-polymer composite materials have low electrical conductivity and poor stability which cannot meet the requirements of DOE standards at the same time. As a major concern, the metallic interconnects suffer from severe electrochemical degradation and high ICR during operating in the highly acidic environment of the PEMFC [167,168]. A combination of these variables hurts overall power and no single material could meet all the proposed property requirements at the same time. However, out of all the materials under consideration, SS has emerged as the most promising to better meet the DOE targets after appropriate modification. For this purpose, the problems can be minimized to a significant extent by using different protective coatings on top of the metal surfaces which is the main focus of this research.

2.4.3. Electrochemical Degradation of PEMFC Metal Interconnector

As mentioned in Chapter 1, metals can be electrochemically degraded due to ions or electrons leaching that adversely affects their efficiency and durability, which can poison the PEMFC and reduce the fuel cell output [169]. It has also been shown that the interconnects operate in a harsh acidic medium of pH around 4~5 and high humidity of 90% as PEMFC working conditions containing acidic ions such as SO_4^{2-}, SO_3^{2-}, HSO_4^- and etc [170]. The anode side of PEMFC is a reducing environment due to the presence of hydrogen and its passes to the cathode side. As a result, it can be concluded that the anode-side is more corrosive than the cathode-side due to the formed unwanted hydride and the presence of $H^+$and F^- ions in the corrosive medium [171]. At the cathode, due to air or oxygen reduction, metal dissolution can cause contamination and the oxidizing environment contributes to oxide formation of PEMFC metal interconnect, which increases the contact resistance resulting in the loss of efficiency and even the failure of the cell [172]. Furthermore, regarding the influence of electrocatalysts ions on oxygen reduction reaction, control of active degradation sites and stabilizing the surface structure can be also affected by the mechanism of metal ion catalyst reaction [173]. Therefore, the dissolved metal ions thus have a detrimental effect on the activity of the catalyst layer, which reduces cell efficiency.

2.4.4. Summary of PEMFC Metal Interconnect

In summary, this review assessed that stainless steel and its alloys are considered to be adequate candidates for use in the PEMFC system to satisfy commercial applications. However, problems related to electrochemical degradation and ICR in the working environment for PEMFCs under extreme conditions, weakly acidic containing F^-, SO_4^{2-} and Cl^- have significantly restricted its large-scale application. In addressing these issues, many research approaches have been focused on surface modification treatments and various protective coatings with considering the cost to provide and enhance electrochemical degradation resistance while simultaneously reducing the ICR to make PEMFC interconnection meet to comply with environmental PEMFC requirements. Meanwhile, intensive research has been conducted on various materials and methods for the development of metal interconnections as well as to uncover the mechanism and control of electrochemical degradation in the environments simulating operations of PEMFC.

2.5. Aim of this Thesis

The aims of this thesis are: (i) establish and use a cost-effective metal as novel PEMFC metal interconnection and strategies to address the issues associated with the study of electrochemical degradation in the simulated PEMFC environment and (ii) development of TFSOC with high resistance to electrochemical degradation and appropriate electrical conductivity on low-alloyed carbon steels to enable its application as metal PEMFC metal interconnect. A literature review on the electrochemical degradation behavior of different uncoated metals and surface engineering of PEMFC metal interconnects are discussed in the following chapter to summarize what other researchers have achieved and to specify the remaining gaps.

Chapter 3

Literature Survey of Metal Interconnects in PEMFC Applications

This chapter reflects on recent studies on (i) electrochemical degradation of the various metal bare substrates as a PEMFC interconnect and (ii) different surface modifications on the steel base, which have been described in the literature.

3.1. Electrochemical Degradation of Bare Metal

The motivation behind the development and evolution of PEMFC interconnect materials has been to reduce the fuel cell's volume, weight and consequently total costs [155]. It has also been established that the contact resistance and electrochemical degradation resistance are the most critical output indicating parameters for a PEMFC interconnection [174]. As discussed in the previous chapter, PEMFC interconnect has the weakness of interconnection degradation, which causes the performance of fuel cells to decrease and ultimately its breakdown. Attributed to the reason that the interconnectors operate in an acidic environment, it is not only electrochemical degradation that is correlated with this component, rather the metallic ions products from the substrate at first increase the surface contact resistance, then reduce the ionic conduction of the proton via the membrane electrode, and eventually poison it [175]. Electrochemical degradation activities of PEMFC metal interconnects in different simulated environments have been thoroughly studied to identify the corrosion mechanism.

3.1.1. Different Simulated Test Solution

Various simulated environments have been used to investigate the corrosion behavior of different types of steel-based used as interconnectors in PEMFCs. In general, these simulated environments are used to measure the interfacial contact resistance (ICR) value with the potentiodynamic electrochemical polarization (PEP) and electrochemical impedance spectroscopy (EIS) experiments in order to investigate the potential of the materials used as a PEMFC interconnect. As a simulated PEMFC environment, the 0.5 M H_2SO_4+5ppm HF solution was used to investigate the electrochemical behavior of austenitic stainless steel as interconnects [46]. For a long period, the stable corrosion current density of the manufactured stainless steel was investigated. The electrochemical behavior of SS316L as interconnect was

studied in different concentrations of H_2SO_4 as a simulated PEMFC cathode environment [176]. As concentrations of H_2SO_4 increase, the corrosion current increased due to a decrease in the thickness of the passive film generated on the surface. Also, Zhang et al. [167] systematically studied the effect of 0.05 M H_2SO_4 + 2 ppm HF + 10 M HCOOH + xM CH_3OH (x=0, 3, 6 and 9) solution on the corrosion properties of SS316L as PEMFC interconnect at 70 °C. The PEP results demonstrated that the corrosion potential of SS316L is moving in a positive direction, while the corrosive current densities decrease when the methanol content increases in different test solutions. The results of EIS also showed that the transfer resistance increases with an increase in the concentration of methanol. As a consequence, the sample tested in a solution with a higher concentration of methanol has a lower ICR value. Stein et al. [177] investigated the SS416 as PEMFC metal interconnect in a solution with pH3, which contains 0.1 ppm hydrofluoric acid (HF) for 24 hours (h) at 80 °C. The ICR behavior of SS416 revealed a complex character in the HF solution, which were varied on the surface at two different levels. The first level was related to densely disperse pitting corrosion in the range of 10-40 μm through susceptible spots at the surface. The second level was related to the corrosion roughing of the surface, where the modification of the surface morphology is useful in the reduction of the ICR. However, the achieved ICR stability was determined below the DOE target (cf. 2.41) when exposed to this corrosive environment. Ben Jadi et al. [45] also studied the corrosion behavior of nickel as a PEMFC interconnect in an aggressive medium using 3.5% NaCl due to its high mechanical and good electrical conductivity. A depressed semicircle was observed at high frequency for the Nyquist plot from EIS, which is attributed to corrosion resistance. Increased polarization resistance was also demonstrated by the development of corrosion products in the interface. The effects of O_2 and H_2 on the electrochemical degradation of SS316L as a metal interconnect were also analysed in the simulated PEMFC environments [178]. Experimental results of PEP showed that I_{corr} in the environment-containing O_2 due to the more stable and thicker passive layer is around one-fourth compared with that of the H_2

environment. On the side of the anode, the stable current on the anode side was negative due to the reduction of $H^+$to H_2 and the positive current at the cathode arises from the degradation of the metal. It has been concluded that such levels of metal ions concentration have adversely affected PEMFC performance and protective coating can be an effective method in order to reduce corrosion to levels acceptable.

3.2. Different Metal Composition of PEMFC Interconnect

The DOE (cf. 2.4.1) has set-up targets that provide instruction for the promising candidate metals to be selected, formed processes, as well as performance assessments of PEMFC interconnect with excellent potential. Accordingly, the most significant performance indicating parameters for PEMFC interconnects are the excellent conductivity with high electrochemical degradation resistance, which are influenced by the chemical composition of metals as a significant factor [176]. In the meantime, in an attempt to achieve full commercialization of metal-based interconnects in the PEMFC system, ease of production, reliability and cost-effective manufacturing should be considered as other essential considerations [179]. Over time, different chromium (Cr), molybdenum (Mo), and nickel (Ni) metal-based compositions have been used due to the corrosive PEMFC operating environment. Several types of research have been devoted to broadening the application of ferritic and austenitic stainless steels as PEMFC interconnect.

Ferrite stainless steels are among the most attractive materials due to the high levels of Cr and Mo, which are widely used to improve electrochemical degradation resistance in aggressive environments [180]. Typical ferritic stainless steels used for PEMFC metal interconnects are SS441, SS444 and SS430 [181]. The electrochemical degradation behavior of SS430 as interconnect has been investigated by Xu Yang et al. [142] in a simulated PEMFC environment at 70 °C. The results specifically showed that the corrosion behavior of SS430 is unstable with a corrosion potential (E_{corr}) and a corrosion current density (I_{corr}) of -439 mV and 30 μA cm^{-2}, respectively. Obviously, this high current density is attributed to the aggressive medium

penetrated to the SS430, which has resulted in severe and accelerated electrochemical degradation. Therefore, owing to low corrosion resistance and release of metal ions contaminating membrane electrodes in PEMFC as well as very limited formability attributable to body-centred cubic (bcc) structures, bare ferrite stainless steels were not accepted as a PEMFC interconnect [182].

Bare austenitic stainless steels, mostly SS310, SS316L, SS904L, SS304L and SS316L were intensively investigated as PEMFC interconnect application [183,184]. From the above mentioned stainless steels, SS304L and SS316L attract the attention of most researchers because of its superior comprehensive properties such as high electrochemical degradation resistance in the PEMFC environment. Zhihao Chen et al. [56] investigated the electrical properties and corrosion resistance of SS304L interconnect in simulated PEMFC working environment of 0.1 M H_2SO_4 solution using open circuit potential (OCP). The results demonstrated that the OCP value of 304SSL showed a small rise at the first 120 h, then decreased steadily and eventually remained constant, suggesting a continuous electrochemical degradation process during long-term immersion in the aggressive environment. The PEP results also revealed that the corrosive ions attacked the passive film over the surface and caused the pitting corrosion of the substrate. Kumar et al. [185] studied the corrosion characteristics and fuel cell performance of SS316L as PEMFC interconnect in an electrolyte of 0.05 M H_2SO_4 + 2 ppm HF at the temperature of 80 °C with the purged of H_2 and O_2 to simulate anodic and cathodic environments, respectively. The results showed an anodic current in the simulated environment, which decreased rapidly and eventually stabilized at $<1\ \mu\ cm^{-2}$. That indicated the formation of a passive layer on the surface. However, the ICR of 155 $m\Omega\ cm^2$ was measured, which did not comply with the DOE 2020 target requirement of 10 $m\Omega\ cm^2$. Therefore, they recommended an appropriate surface coating or engineering of the surface oxide to enhance its conductivity and electrochemical degradation properties. Compared to SS304L, SS316L has a higher resistance to electrochemical degradation due to

the presence of Mo in its composition, which may be attributed to the pitting and crevice resistance [186]. High chromium content or surface treatment is required in order to achieve good chemical compatibility and necessary corrosion resistance of such stainless steels in the PEMFC operating environment [187]. However, high alloy components and low carbon content have led to higher interconnects cost, and their use for production volumes is reduced when the cost is taken into consideration.

As compared to stainless steel, mild steel such as low carbon steels are inexpensive and have excellent mechanical properties [188]. Various low carbon steels were used as PEMFC interconnectors and to increase their weak resistance to electrochemical degradation different coatings or surface treatment methods have been applied on the surface of the steel [189]. The C45E low-alloyed carbon steel (AISI/SAE1045) is a commercial low-cost material (80% cheaper than the SS304 and SS316L as common interconnect metals) commonly used due to its combination of formability and high strength. However, its low electrochemical properties that include corrosion and rust resistance due to lack of chromium render it unpleasant to operate under harsh conditions [190,191]. As a result, several studies have been successfully performed to improve the C45E electrochemical weakness and use it as PEMFC interconnects under harsh conditions. Bai et al. [192] have claimed to be one of the first research groups to use C45E carbon steel as a PEMFC interconnect. Excellent combined properties such as low cost, high mechanical strength and the ease of forming sheets are advantages of using this steel as interconnect, which can effectively decrease the total cost of the fuel cell. Owing to the low electrochemical degradation resistance and ICR of C45E steel, a low-temperature pack chromization technique was employed to modify for the application of interconnect in PEMFC. Various analysis methods were used to evaluate the C45E as a good alternative material for PEMFC interconnects. The PEP results in 0.05 M H_2SO_4 at 70 °C showed that the C45E exhibited the lowest ICR of 3.13×10^{-8} A cm^{-2} with the most stable I_{corr} of 8.75×10^{-5} A cm^{-2} at anode and cathode environment. In the view of electrochemical degradation resistance, the

coated C45E steel demonstrated excellent performance. Hence, the performance of chromized C45E carbon steel is comparable to that of graphite or stainless steel for the application of interconnect in PEMFC.

Following from the previous study, Bai et al. [193] used rolling pre-treatment along with pack chromization on C45E steel to produce an anti-corrosive and highly conductive PEMFC interconnect. Modified steel plates were investigated in a single-cell PEMFC for 100 h and their performance was compared to that of conventional graphite interconnectors. The results revealed that the PEMFC single cell with C45E interconnects exhibited a maximum power density of 0.51 W cm^{-2}, which is very close to that of the cell with graphite interconnect (0.50 W cm^{-2}) as high-efficiency material in the PEMFC system. Based on the excellent mentioned results, modified C45E steel could be considered a reasonable candidate for interconnection in PEMFC applications. Previous work continued with surface modification of C45E as a PEMFC interconnect using carbides and nitrides [189]. Then, electrochemical behavior and contact resistances of the modified low-carbon steel interconnect were investigated in 0.5 M H_2SO_4 solution at room temperature (RT) for long period. The modified C45E interconnect pre-treated with electrical discharge currents of 2 A showed the lowest I_{corr} of 5.78×10^{-8} A cm^{-2}. At a compaction pressure of 140 N cm^{-2}, the smallest ICR value of 11.8 mΩ cm^2 for modified C45E steel was significantly lower than of various untreated and commercial stainless steels such as SS316L as well as the DOE target. As a result, modified mild carbon steel containing carbides and nitrides can be a promising and cost-effective candidate for metallic PEMFC interconnector material.

Yuan et al. [194] also studied the surface roughness of the C45E interconnect as a very important factor in the performance of the PEMFC. Surface quality is a very significant issue in the interconnection efficiency owing to the major effect on the resistance to contact and electrochemical degradation. PEP experiments were performed to evaluate the electrochemical behavior of interconnect in 0.5 M H_2SO_4 solution at RT as environment simulation for PEMFC.

The results showed that the milling process parameters greatly influence the surface roughness and corrosion behavior of low-carbon PEMFC interconnectors. The polarization curves of C45E stainless steel showed significantly lower I_{corr} value (6.37×10^{-5} A cm^{-2}) and ICR that meets the DOE target for PEMFC interconnect applications. In summary, it is clearly evident from previous studies that the variety of different grades of bare metals as PEMFC interconnect do not meet the requirements of DOE target and that surface engineering techniques are necessary.

3.3. Surface Modification of Metal Interconnect

Literature data have shown that the different grade metals have become the standard material for PEMFC interconnect applications. However, commercially available metals are not specifically designed for interconnect applications and have resulted in serious issues and major concerns leading to premature degradation of the PEMFC stack. These issues may become particularly problematic with growing ICR, electrochemical degradation resulting in stack poisoning and cell malfunction. To overcome these important problems, surface modification techniques have been identified as a possible solution to resolving and improve the interconnect challenges under PEMFC operating environment [195]. Therefore, surface chromizing and nitriding are typical modification technologies that are evolving rapidly and used on PEMFC metal interconnect to minimize corrosion and ICR in harsh environments [196,197].

3.3.1. Surface Chromizing of Metal Interconnect

Different protective chromium-rich films with reasonable adherence to the metal substrate and excellent resistance to electrochemical degradation and thermal oxidation are of great commercial importance [198]. Over the years and due to its good properties, the chromizing process has experienced tremendous improvement and has been the subject of careful and detailed studies for various applications [199]. In several studies, it was reported that the novel grades of metals through appropriate surface chromizing modification technique can be a viable material for the development of conductive PEMFC metal-based interconnect with high resistance to electrochemical degradation. Dong et al. [200] have shown the satisfactory performance of the surface chromizing layer on SS316L stainless steel as PEMFC interconnect. For this purpose, surface chromizing treatments have been performed by a high-temperature element diffusion process. The electrical conductivity and corrosion properties of the fabricated chromizing layer on SS316L were then investigated in 0.05 M H_2SO_4 + 2 ppm HF at 70 °C. PEP results showed lower I_{corr} (0.264 μA cm^{-2}) with the higher electrochemical impedance indicating a stable passive film on the surface of the substrate. However, despite the formation of the Cr_2O_3, Fe_2O_3 and Fe_3O_2 oxide films on the surface, the low ICR of 1.4 mΩ cm^2 was gradually stabilized after the compaction force of 140 N cm^{-2}, which indicated excellent electrical conductivity.

Zhang et al. [201] were also prepared the Cr-based multilayer coating on SS304 at a low temperature and its feasibility as a promising interconnect material for PEMFC is then evaluated. Under the above PEMFC simulation environment, the lower I_{corr} of 10^{-7} mΩ cm^2 and potential of 600 mV was measured as typical cathodic potential in the PEMFC environment. Due to the increased water contact angle, the chromium multilayer coating demonstrated higher electrical conductivity and good resistance to electrochemical degradation. In the work by Tsai et al. [199], chromized coatings on C45E steel as a cost-effective interconnect in PEMFC applications were also prepared by low-temperature pack

chromization. C45E steels coated with chromized layer showed a big water contact angle of about 100°, which suggested that the C45E steel is the most hydrophilic material. This outcome may be attributed to the existence of oxide corrosion products such as Fe_2O_3 and Fe_3O_4 on the surface, contributing to a better affinity with water than the chromium carbide on the surface of the chromized specimens. Also, the PEP results of the coated C45E specimen showed the low I_{corr}, 8.37×10^{-8} A cm^{-2}, and the small ICR, 14 mΩ cm^2 in a 0.5 M H_2SO_4 at RT. Based on the excellent properties mentioned above, the chromization process combined with the passive oxide film from the substrate can significantly improve the properties of C45E carbon steel as PEMFC interconnects. However, there is a limit to the chromizing process. Although Cr cementation for several hours is advantageous to corrosion resistance, however, surface defects such as voids and pits can leaded to long-term cementation, which may lead to high I_{corr}. Meaning, overdoing the chromizing process can have severe consequences for the efficiency of the interconnectors and eventually reduce the output power of the PEMFC.

3.3.2. Surface Nitriding of Metal Interconnect

The increased use of metals in the harsh environment at different sets of operating temperatures has raised the industrial importance of nitrides, which can improve their surface hardness and corrosion resistance using the nitriding process. The nitriding process is a kind of thermochemical surface treatment procedure in which nitrogen is applied to the surface of metal-based materials using a variety of techniques [202]. Oxidation is the most significant problem encountered in metallic materials used in various industries such as energy and fuel cell applications [203]. Nitrided metal surfaces are frequently susceptible to hydrolysis and oxidation, which represent indirect metallic degradation [204]. In this process, nitrogen can enter both α and γ iron phases, which ensures that various forms of steel can be nitrided at low temperatures without structural deformation [205]. To improve the electrochemical behavior of metals interconnect in PEMFC applications, various nitriding techniques including ion-plasma and diffusion methods have been employed to synthesize protective coatings [206,207].

Recently, Sung Kim et al. [141] investigated the effect of nitrogen implantation into SS316L as PEMFC interconnects by plasma immersion ion implantation. In summary, the phase transformation characteristics showed that the nitrogen might be located beneath the surface at peak concentration. The corrosion resistance was also enhanced due to the formation of nitrogen supersaturated phase, preferred orientation and distribution of nitrogen concentration near the surface as the most critical factors. PEP result showed an excellent corrosion resistance of 6.37×10^{-6} A cm^{-2} at 70 °C during the short-term immersion test in a simulated PEMFC environment. On the other hand, in terms of electrical conductivity the low ICR value of 0.7 $m\Omega\ cm^2$ was measured due to the reduction of grain boundaries as discussed through phase examination.

Tian et al. [208] discussed the effect of pH value on corrosion resistance and surface conductivity of plasma-nitrided SS304L interconnect for PEMFC applications. The results of their study further confirmed that low-temperature plasma nitriding has formed a dense and supersaturated nitrogen nitrided layer on the surface. Electrochemical behavior for untreated and nitrided steel showed that the ICR of 16 $\mu A\ cm^2$ for nitrided steel, which rose with increased pH value. The results of PEP showed that the SS304L is thermodynamically unstable in an aqueous solution, and metal passed from the metallic state to ions in solution with the evolution of hydrogen. This reaction of hydrogen ions in acid solution and progressively with water molecules raised the pH to neutral and resulted in decreased I_{corr} with increasing pH value from 1 to 3. However, more research is required to determine the long-term stability of the film and the performance of a single PEMFC. However, most of I_{corr} and ICR values were not satisfactory and are still higher than the DOE target. Furthermore, the electrochemical behavior of the different nitride layers was not adequately studied after a long-term test in a simulated PEMFC environment due to their unstable performance in harsh conditions.

3.4. Surface Modification of Metal Interconnect Through the Coating

The development of appropriate coatings is implemented as another effective technique of enhancing electrochemical degradation resistance and conductivity of conventional metallic based materials as PEMFC interconnect. By definition, the coating is a covering that can be applied on the surface of the various substrate in order to improve the functionality and achieve modification purposes [209]. In general, the main objective of coating on PEMFC interconnect applications is to serve as an electrochemical degradation resistance interface in harsh PEMFC environment, thereby reducing or eliminating the ICR value of interconnect as one of the most significant parameters that reduce the overall power output of the fuel cell stack [195,210,211]. These coatings improve surface characteristics such as mechanical and corrosion resistance without significantly altering the substrate interconnect properties [212]. Besides, the applications of different coatings can prevent the dissolution of ions as a result of using metals interconnect in a PEMFC corrosive media [213,214]. To satisfy the required properties for metal interconnect in PEMFC application, the coating must be able to meet the following essential criteria:

- The coatings need to be developed by low-cost, easy and fast technique with lightweight materials [206].
- They must exhibit long-term stability and good adhesion to the metal-based substrate without exposing the substrate to the corrosive environment [215,216].
- These coatings require to be impermeable to reactant gases and chemically stable or inert [217].
- The coating must be electro-conductivity with a low ICR value in order to improve electron conduction through it to the external circuit [218,219].

Carbon-based and metal-based coatings have been studied over the years as suitable candidates for improving the mechanical, electrochemical and electrical conductivity properties by depositing on the surface of the metal interconnect in PEMFC application [142,220].

3.4.1. Modification of Metal Interconnections through the Carbon-Based Coating

Surface modification technology through the carbon-based coating is a promising technique for improving the electrochemical degradation resistance for PEMFC metallic interconnects applications. However, two main issues including ameliorating the corrosion situation while reducing the ICR value in a PEMFC operating environment need to be taken into consideration [221]. Carbon-based coatings mostly consist of graphite, diamond-like carbon, self-assembled organic monopolymers and conductive polymer [129,222,223]. These coatings can minimize corrosion of metallic substrates through the barrier mechanism owing to their excellent stability and high level of electrochemical degradation resistance. However, the carbon-based coatings must have similar coefficients thermal expansion (CTE) with the interconnect material to prevent crack or wrinkles as an adverse parameter for cell output that generally occurs during the PEMFC operating temperature changes [224,225]. Generally, physical vapor deposition (PVD) and chemical vapor deposition (CVD) techniques are used to deposition anticorrosive carbon-based coatings to circumvent the shortcomings of PEMFC metallic interconnect surface [226,227]. CVD has been identified as one of the most versatile and promising methods of producing carbon-based coatings with chemical reactions on the heated interconnect substrate utilizing gaseous reactants [228]. The deposition of nanometer-scale carbon-based coating with different compositions can be provided using this technique. Moreover, single and multi-layer protective coatings with a controlled scale can be produced at low processing temperatures [229].

Che et al. [230] deposited carbon coating on SS316L by CVD and investigated the material structure, electrochemical behavior and ICR of the coated interconnect under PEMFC operation conditions. These performances were researched using different techniques. The finding demonstrated that the coating performance was influenced by various CVD parameters. These results optimistically revealed that the larger scale of microcrystals with hexagonal structure improved the conductivity of coated interconnect. The passivation current density

(0.6 V) and stable I_{corr} have been found to be less than 0.5 mA cm^2, which meet the DOE 2020 technical target. It was also found that the corrosion resistance of the coating is mainly related to the structure of the coating material and the coating defects. Also, it was observed that the ICR values dramatically increased due to the combination of weak ion bombardment and excessive coating growth. Although the carbon coating improved the corrosion resistance of bare interconnect, the cost, durability and suitability for mass production were not mentioned. The microstructure of niobium (Nb) doped amorphous carbon film on metallic interconnect for PEMFC applications was systematically characterized by Hou et al. [231]. ICR and electrochemical degradation were also tested to evaluate the effect of Nb doping. The microstructure analysed of coating showed that the doped Nb refined grain size increased the film compactness, which was beneficial for corrosion resistance. Meanwhile, the phase and bond type changed with the Nb-doped concentration. Besides, with moderate Nb doping, the ICR decreased to 1.22 mΩ cm^2 from an initial value of 4.41 mΩ cm^2. The acceptable resistance (R_{ct}) of coating which reflects the relative anti-corrosive property was measured above 1.81×10^6 Ω cm^{-2}. Nevertheless, it was concluded that the real application of Nb-carbon coating, long-time durability and anticorrosive performance in a high potential for PEMFC metallic interconnect applications still required further investigation. Electrically conductive polymers (ECP) coatings provide excellent electrochemical degradation resistance for PEMFC metallic interconnect applications. However, the balance of electrochemical stability, mechanical strength and electrical conductivity become the main challenge of different polymer coating as protective for PEMFC application [223]. Jiang et al. [232] have studied the polymer composite coating as a protective metallic interconnects in PEMFC applications. The results pointed out that the coatings have ultra-high resistance to corrosion and the contact resistance was within an acceptable range. However, the corrosion protection effect was lost with prolonged immersion time, which leads to an expansion of the contact area and resulting in high ICR values. Also, the authors were not mentioned the manufacturing costs, durability

and suitability for mass production. Overall, all the results and other research were found that several carbon-based composites coatings are not considered appropriate for metallic interconnect in PEMFC applications due to their intrinsic brittleness and poor adhesion as a usual problem [233-235]. Also, it is currently difficult to directly monitor the electrochemical and electrical conductivity behaviors to understand any implication of carbon-based coatings on the PEMFC stack under real operating conditions [236]. More importantly, the determination of the durability of such coatings is extremely time-consuming and costly due to the high expense of the production method [237].

3.4.2. Modification of Metal Interconnections through the Metal-Based Coating

The low electrochemical property of the metallic interconnect for PEMFC leads to contamination of the membrane electrodes. This can be suppressed by passivation that in turn increases the ICR and decreases the efficiency of the fuel cell stack. Significant progress has been made in addressing these barriers. It was reported previously that PEMFC metallic interconnects coated with carbon-based materials are a cost-effective approach to improve corrosion resistance while keeping the ICR low [238,239]. Also, different kinds of ECP coating were studied as potential coating materials due to their chemical and electrochemical stability [240]. But one main disadvantage of ECP is the presence of micro-defects that serve as migration channels for corrosive ions to penetrate to the substrate surface and passivate interconnect, which could further increase the ICR [241,242]. In recent years, additional studies on both chromized and nitrided layers (cf. 3.3.1 and 3.3.2) were evaluated as protective coatings on the different metal interconnect for PEMFC applications. Nevertheless, in spite of the high corrosion resistance of these compounds, they are no longer employed nowadays owing to their carcinogenic nature and adverse environmental effects. To address this challenge, some chemical inert conductive coatings, for instance, thin-film metallic glass coatings (TFMGs) or amorphous metal alloys [243] and thin-film solid oxide coatings

(TFSOC) [244] have proven to be promising candidates to be used as a protective coating for metal-based interconnect in PEMFC applications.

3.4.2.1. Thin Film Metallic Glass Coating (TFMGs)

For decades, $TFMG_S$, as one of the main subjects of scientific research and engineering applications, has been developed specifically to prevent environmentally assisted metallic corrosion of substrate surfaces. Thus, TFMGs might be promising materials to satisfy the clearly stated requirements to improve the electrochemical and conductivity properties of the PEMFC metallic interconnect [243,245]. As non-crystalline (non-uniform) metals, $TFMG_S$ do not show a long-range atomic order since they generally form with rapid cooling rates to keep glass melting state [218]. Glass and crystalline transition temperatures have been considered as important parameters during the heating process to create a liquid state [246]. The $TFMG_S$ has several superior properties owing to its irregular atomic structure and lack of grain boundaries, including soft magnetic and excellent mechanical properties, high strength, corrosion and abrasion resistance [247-249]. So far, different physical vapor deposition methods such as pulsed laser [250], arc plasma [251], and sputter deposition [252] have been used to fabricate $TFMG_S$ with excellent electrochemical and conductivity properties. In $TFMG_S$ fabrication, sputtering deposition represents a commonly applied method, where pure targets of single elements or alloy targets can be used to produce thin films. In recent years, researchers have successfully developed $TFMG_S$ based on zirconium and titanium.

Recently, Zr-based [245] TFMGs have been coated on an austenitic stainless to enhance the corrosion properties of the metallic interconnect for PEMFC applications. For this purpose, $Zr_{63.9}Al_{10}Cu_{26.1}$ was prepared on SS316L as a protective coating using a direct magnetron sputtering system. The electrochemical behavior of the coating was investigated by conducting electrochemical potentiodynamic measurements (PEP and EIS) in 0.05 M H_2SO_4 + 2 ppm HF at 70 °C as PEMFC simulated environment. The results showed that the 0.2 μm surface roughness as a significant factor achieved an ICR of 24.2 mΩ cm^2 and I_{corr} of 1 μA cm^2, which

is close to the DOE target for 2020. Surface roughness and adhesion as serious challenges of the sputtering technique are influenced by various factors, such as negative bias voltage and substrate temperature.

A novel TiSiN coated titanium alloy as PEMFC interconnect by magnetron sputtering was described in the work by Peng et al. [243]. The TiSiN nanocomposite coating, with an average thickness of ~10 μm showed a homogeneous and compact structure, free of defects such as voids or pinholes. The passive film with the good hydrophobicity that formed on the TiSiN coating, with I_{corr} of $\sim 10^{7}\ \Omega\ cm^{-2}$ displayed good electrochemical stability and was less affected by changes in HF concentration from the simulated environment at 70 °C. For the TiSiN coating, the ICR value lower than the bare substrate was 18.3 $m\Omega\ cm^{-2}$ under a compression pressure of 140 $N\ cm^{-2}$. Nevertheless, a detailed understanding of TFMG formation and its suitability to achieve a reliable and affordable coating with the excellent properties required for application in PEMFCs is still missing. For example, their structural and mechanical properties have not been studied systematically. Furthermore, the electrochemical behavior of such coatings has not been investigated for a prolonged period, probably due to numerous factors, such as low adhesion and expensive manufacturing.

3.4.2.2. Thin Film Solid Oxide Coating (TFSOC)

As discussed in previous sections, several materials and methods are available for the development of protective coatings for various types for PEMFC interconnects applications exposed to mechanical and chemical damage in the harsh environment. One of the most significant advantages of these protective functions is the reduction of manufacturing PEMFC costs due to the improvement of lifetime and high-throughput since the production of new parts is not necessary [253]. However, as described in the previous sections many coatings such as metal chromite, metal nitrides, metal carbides, and especially amorphous carbon and multilayer coatings fail to fulfill the requirements for electrochemical degradation resistance and ICR for satisfying the DOE targets. Meanwhile, the most effective barrier between different steels and harsh environments, are several oxide coatings, which increase high thermal fatigue resistance and high electrochemical degradation resistance. Several ZrO_2, Al_2O_3, Cr_2O_3, SiO_2 and TiO_2 based composite coatings and etc. all have very good long-term chemical stability, have recently attracted considerable attention due to their unique properties. Oxide ZrO_2 coating can improve oxidation and electrochemical degradation resistance of metals under different conditions due to its high dielectric constant, good thermal and chemical stability [254]. Different composite Al_2O_3 based coatings have been extensively studied as barrier materials to enhance the corrosion resistance and improve the service life of the substrate [255]. Furthermore, corrosion-resistance increases significantly due to corrosion products such as iron oxides and the addition of Cr_2O_3 nanoparticles to the coating [256].

L-Kui et al. made a SiO_2 coating on alloy using tetraethyl orthosilicate as a chemical precursor [257]. It was found that the SiO_2 coating efficiently improves corrosion resistance. After hot corrosion at 700 °C for 100 h in a eutectic salt mixture (75 wt.% Na_2SO_4+25 wt.% NaCl), no spallation and obvious destruction are observed. Edvan et al. [258] successfully developed a TiO_2 and N-doped TiO_2 coating on SS316L by metallorganic chemical vapor deposition at different temperatures. The films presented good homogeneity, low porosity and rounded

grains in the range of 40-90 nm. The EIS and PEP studies demonstrated that due to their microstructural variations, TiO_2 films grown at 400 °C displayed better electrochemical degradation resistance than those grown at 500 °C. According to the results presented, the electrochemical degradation resistance of N-TiO_2 coating on the substrate was not improved due to the formation of the nitrogen-rich phases in the coating. Since the corrosion initiates at the surface, the oxide coatings could be suitable candidates for use in PEMFC applications due to their inexpensive, eco-friendly, fast manufacturing technique and high resistance in harsh environments [259]. Some researchers reported the investigations on the performance of oxide films on the metal surface of interconnect in PEMFC application in order to improve the electrochemical degradation and long-term stability under the simulation operating condition. However, most metal oxides are generally electrically non-conductive, which is the main reason that relatively few oxides are deemed suitable for protective of interconnect in PEMFC applications.

In the work by Linghui Yang et al. [260], a SnO_2 oxide coating was successfully prepared on SS304 by combining the sol-gel dip-coating method. The coated was used to enhance the corrosion resistance of SS304 as interconnects in a simulated PEMFC environment. Compared with the bare SS304 (33.22 μA cm^2), the value of I_{corr} for the uniform and compact SnO_2 coating was decreased significantly to 0.1327 μA cm^2 in a simulated environment. In specific, the E_{corr} of the coated substrate with the thickness of 220-320 nm and poor crystallinity according to the XRD result was shifted from -330.22 to 140.65 mV in simulated PEMFC environment, which assisted it to achieve the low ICR and showed that the corrosion resistance of SS304 was significantly improved by SnO_2 surface layer oxide coating. However, despite the excellent electrochemical degradation resistance, the electrical property of the coating probably due to its low thickness has not been investigated. Furthermore, the long-term stability of coating in the PEMFC simulated environment has not been studied to approach or achieve the DOE targets. The team of A.P. Manso and Marzo et al. [261] prepared a tantalum oxide

coating on SS316L as interconnects in PEMFC applications and investigated the corrosion resistance and ICR. Results obtained by different experimental techniques showed a dense coating structure with an average thickness of 30 μm, mainly formed by surface crystals of α-Ta (bcc), Ta_2O_5 and carbon with good adherence to the base metal substrate. In order to estimate the durability of the coating at high potentials, long-duration tests (>100 h) were carried out at a potential of 1.139 V. The value of 8.02 μA cm^2, which is 8 times higher than the DOE target (1 μA cm^2) was achieved probably due to the progressive decrease of the protective character of the coating. Furthermore, the PEP result showed that the I_{corr} of oxide-coated SS316L in a simulated environment with a solution of H_2SO_4 + 0.1 ppm HF at 80 °C was about 0.038 μA cm^2, while the ICR at a compacting pressure of 140 N cm^{-2} was about 32.6 mΩ cm^{-2}. The results indicated that the SS316L coated with tantalum oxide showed excellent performance and a large lifetime as interconnect in PEMFC applications.

Ji Hun Park et al. [262] also investigated the SnOx-FTO oxide coating onto SS316L substrates as interconnects in PEMFC applications. To improve the ICR and corrosion resistance of the substrate below 0.6 μm of oxide coating composed of polycrystalline structures was applied on the surface. The lowest ICR of 74 mΩ cm^{-2} was obtained at the base compaction force of 150 N cm^{-2}. The corrosion resistance of 6.64 μA cm^2 was also obtained at the operating microwave power of 1000 W. Furthermore, the enhanced interconnect material provides a higher power density of about 225 mW cm^{-2} at the I_{corr} of 0.5 A cm^{-2} and the voltage of 0.6 V in the environment of 1M H_2SO_4 + 2 ppm HF at 70 °C purged with nitrogen gas. The deposition of SnOx-FTO coating on the substrates has contributed to the enhancement of ICR, corrosion resistance, power density, and cell voltage stability for interconnects of the PEMFC system. However, the long-term stability, electrical conductivity of such an oxide film with low thickness have not been investigated thus far probably due to the costly preparation and limitation of the technique.

Wang et al. [263] have studied the adhesive TiO_2 coatings with Nb-doped for SS316L as interconnects of PEMFC applications. The TiO_2 coatings with different Nb content were prepared using the sol-gel process as a simple and cost-effective technique, and their corrosion behavior is also investigated in 0.1 M H_2SO_4 at 80 °C. It was shown that the sol-gel as a fast, efficient, cost-effective and environmentally friendly manufacturing techniques technique can be a suitable method for preparing high electrochemical degradation resistant coatings in PEMFC applications. The $TiNbO_2$ coating has decreased I_{corr} from 26 to 0.13 $\mu A\ cm^2$. Moreover, the ICR of the pure TiO_2 coating decreases sharply with the Nb doping, which can be concluded that the Nb can significantly enhance the electroconductivity of the oxide coating. Furthermore, the $TiNbO_2$ coating has exhibited good chemical stability for up to 30 days under simulated PEMFC conditions.

Recently, Jin et al. [264] investigated incorporating oxygen into TiN coating to resist high potential effects on SS316L as interconnects in PEMFC applications. The results of X-ray photoelectron spectroscopy and X-ray diffraction showed that TiNO and TiO_2 existed in oxygen-doped coatings. The surface morphology analysis indicated that the oxygen-doped coatings tended to come into being denser surface. The results showed that there are relatively big grains on the coating surface. Also, some pinholes and particles unavoidably have been generated during the deposited course. After test and analysis in the simulated PEMFC cathode environment, it found that the doping oxygen into the coating was significantly enhanced oxidation resistance and corrosion resistance of the coating with the ICR values over 11.2 $m\Omega\ cm^{-2}$ (close to the DOE 2020 target) but at the same time weakened the conductivity. Therefore, further research has been suggested to be conducted in improving the conductivity of the coating, such as a multilayer structure of an excellent conducting layer. It is also has been proposed to experiment with doping oxygen into other coatings to prepare oxide coating for better conductivity and corrosion resistance to the high potential.

3.5. Summary of Literature and Aims of Thesis

Based on the literature review it is clear that several types of steels such as stainless steel, low and medium carbon steel can be promising alternative materials for commercial application in the PEMFC. Furthermore, it has been shown that these metallic interconnects are vulnerable to electrochemical degradation attack in the PEMFC harsh environment conditions. Various surface modification treatment techniques and different types of protective coatings have been applied to the PEMFC metal-based interconnect. Researchers have demonstrated improved electrochemical resistance to degradation and electrical conductivity. However, although these current surface modification methods and coatings have a reasonable output of electrochemical degradation resistance, still some weaknesses such as low electrical conductivity, long-term stability, and cost-effectiveness have limited their efficiency. Furthermore, the use of precious common metals such as SS304 and SS316L, while providing good degradation resistance and excellent conductivity, however, are not economically reasonable due to high costs and difficulties in processing and machining. Therefore, the research for low-cost metal interconnection materials, coatings and production methods with high resistance to electrochemical degradation in stable ICR values, high conductivity as well as long-term stability is necessary to satisfy the DOE target. Despite the continuous and comprehensive efforts on studying the electrochemical and conductivity behaviors of various types of materials and protection techniques for interconnects in PEMFC applications, the limitations of the previous investigations have left knowledge gaps that need to be filled, which is the main focus of this thesis work.

Firstly, it is known that TFSOC based on titania and silica possesses high electrochemical degradation resistance but its ICR is significantly increased due to the isolating properties under the test condition. Such a TFSOC is therefore prepared by the sol-gel method. To achieve desired electrochemical degradation resistance and electrical properties on cost-effective interconnects to realize the economic feasibility of PEMFCs, the effect of different annealing

temperature, atmosphere and number of the coating layer (L) of corrosion-resistant TFSOC on low-cost commercial C45E steel have been investigated for the first time. The effect of these processing parameters on the corrosion resistance of C45E steel is discussed. The main objective of this work is to combine the merits of both the synthesis route and coating procedure to deposit a high-performance Ti-Si-oxide protective layer on the C45E steel substrate as interconnects in PEMFC applications. The results are presented in **Chapter 4**.

Moreover, it is important to assess the potential of TFSOC on the C45E surface to combine the merits of TFSOC and substrate as a low-cost alternative interconnects in PEMFC. Therefore, we focused on producing a cost-effective and environmentally sustainable anti-corrosive TFSOC with long-term stability for use as interconnects in PEMFC applications. In addition, it has been shown that the charge carrier concentration and, thus, the electrical conductivity of various low or semiconductor TFSOC can be strongly enhanced by extrinsic dopants. Consequently, in the case of such mixed oxides to be as potential conductive TFSOC, Nb is most commonly used as doping agents (donor materials) to achieve high n-type conductivity while maintaining high electrochemical degradation resistance. For this purpose, TiSiNb as conductive TFSOC were deposited via a sol-gel process on C45E steel substrates. The influence of Nb concentration and annealing temperature on the morphology of the thin films were examined. The microstructure and phase of obtained TFSOC were investigated. The electrochemical degradation behavior and long term stability utilizing over the potential application and electrical conductivity of TFSOC through impedance analysis were also investigated. The results are presented in **Chapter 5**.

Chapter 4

Effect of Processing Conditions on the Structural Properties and Corrosion Behavior of TiO_2-SiO_2 Multilayer Coatings Derived via the Sol-gel Method

Abstract: TiO_2-SiO_2 multilayer protective coatings were prepared via the sol-gel method on a C45E steel substrate. The influences of the number of layers, annealing temperature and annealing atmosphere on the corrosion resistance were investigated. Electrochemical characterization showed correlations between the processing parameters and the corrosion resistance. A maximum polarization resistance of 61 kΩ cm^2 was achieved with coatings of three layers annealed at 900 °C in air compared to just 2 kΩ cm^2 for the uncoated C45E steel sample. This research revealed the possibility of preparing a dense corrosion-resistant layer on C45E steel with minimal surface defects by optimizing the processing parameters.

4.1. Introduction

Most metals and alloys are vulnerable to corrosion due to their unstable electrochemical properties, resulting in substantial economic losses [265-267]. With scientific advancements, corrosion on protective coatings for metal and alloys can be controlled or sometimes prevented. The utilization of chromate compounds in protective coatings on metal substrates has an extensive history and background [268,269]. These compounds, however, are no longer been utilized today due to their carcinogenic nature and their adverse environmental impact. Hence, in recent decades, extensive research efforts have focused on developing affordable and environmentally friendly coating materials for corrosion resistance [270,271]. Corrosion-resistant coatings create a physical barrier on the applied surface against corrosive agents and are generally used to protect steel with low corrosion resistance [272-275]. C45E steel (AISI/SAE 1045) is a widely used engineering material because of its low cost and good formability. However, its low corrosion resistance limits its application under corrosive conditions [190,276,277]. Metal-, oxide-, carbide- and composite-based coatings have been used to increase the mechanical properties and corrosion resistance of steels [278,279]. Some of the widely used oxide-based coatings are TiO_2- [280], SiO_2- [281], TiO_2-RuO_2-La_2O_3- [282], SiO_2-Y_2O_3- [283], SiO_2-Al_2O_3- [284], SiO_2-TiO_2-ZrO_2-Bi_2O_3- [285] and TiO_2-SiO_2-based [286] coatings. TiO_2- based coatings are well-known for their chemical stability, photocathodic protection, low thermal expansion coefficient, self-cleaning properties and oxidation protection [287-293]. TiO_2 coatings successfully improved the corrosion resistance of a Ti alloy [294]. TiO_2 has thus been proven to be an effective protection layer for AISI 316 stainless steel and carbon steel [295,296]. In contrast, SiO_2-based coatings have high corrosion resistance, thermal stability, and excellent mechanical strength [297,298]. Moreover, SiO_2-based coatings have superior and long-term anti-corrosion properties on Mg alloys [299], titanium alloys [300], carbon steel [301] and stainless steel [302]. To summarize, TiO_2-SiO_2-based ceramic coatings are expected to be effective in enhancing wear resistance, hardness and corrosion resistance.

Recently, the corrosion properties of TiO_2-SiO_2 coatings derived by the sol-gel and anodization techniques and crystallized at low temperatures on a Ti alloy and 316L stainless steel, respectively, have been extensively studied. These coatings demonstrated enhanced protection against corrosive attacks on the aforementioned metallic substrates [286,303].

Gas and liquid phase methods are common techniques to deposit ceramic-based corrosion-resistant coatings. Evaporation [304], sputtering [305], pulsed laser deposition [306], chemical vapor deposition and chemical spray pyrolysis [307,308] are some of the widely used gas-phase routes to produce protective coatings. The most common liquid-phase methods are the sol-gel and electroplating processes [309-311]. Sol-gel methods are simple and cost-effective techniques compared to other sophisticated techniques requiring high vacuum conditions that will increase the production cost of the protective coatings. The sol-gel technique can be adopted on a variety of substrates such as metals, glass, ceramics and plastics substrates [312-316] to coat them with high purity protective coatings. Furthermore, the sol-gel method facilitates the cost-effective achievement of superior chemical and mechanical properties of coatings by the careful selection of chemical composition and tuning of the synthesis parameters. Dip-coating, spin-coating and spraying methods have been used to produce coatings on substrates using sol-gel derived coating materials [317-319]. Among these, dip coating is an effective procedure for applying thin films with different thicknesses on substrates with large areas, which is advantageous for the commercial production of protective coatings. In the present work, the effects of different annealing temperatures, atmospheres and numbers of the coating layer (L) of corrosion-resistant coatings derived by sol-gel synthesis and produced by the dip-coating method on low-cost commercial C45E steel were investigated for the first time. The effects of these processing parameters on the corrosion resistance of C45E steel are discussed. The main objective of this work is to combine the merits of both the synthesis route and the coating procedure to deposit a high-performance TiO_2-SiO_2 protective layer on a C45E steel substrate. The chemical composition and the structural and physical

properties of the coatings were investigated by a combination of TGA-DTA, FTIR, SEM-EDX and XRD on all compositions. The corrosion behavior of the coatings was investigated using potentiodynamic electrochemical polarization (PEP) and electrochemical impedance spectroscopy (EIS).

4.2. Experimental Procedure

4.2.1. Materials and Preparation of the Substrate

Tetra-n-butyl Orthotitanate (TBOT, $C_{16}H_{36}O_4Ti$, Merck, 98% purity) and tetraethyl orthosilicate (TEOS, $Si(OC_2H_5)_4$, Merck, 99% purity) were utilized as titanium oxide and silicon oxide precursors respectively. Ethanol, distilled water, and 69% nitric acid were used as the solvent, hydrolysis agent and catalyst respectively. Initially, separate TiO_2 and SiO_2 based sols were prepared. To prepare the TiO_2 sol, 40 mL of ethanol was poured into a beaker and stirred at room temperature (RT). Then, 10 mL of TBOT was added to the beaker and continuously stirred for one hour. To prepare the hydrolysis agent, 5 mL of water and 2 mL of nitric acid were mixed in a glass beaker, and 10 mL of ethanol was subsequently added and stirred for 30 minutes at RT to form a homogeneous solution. The prepared hydrolysis agent was added dropwise to the TiO_2 sol. The SiO_2 sol was prepared following the same procedure, using 6.7 mL of TEOS. The prepared TiO_2 and SiO_2 sols were stirred separately for one additional hour each at RT. Finally, the TiO_2-SiO_2 sol was synthesized by dropwise addition of the SiO_2 sol into the TiO_2 sol. The molar concentrations of Ti and Si at this step were equal (Ti=0.2 mol/L and Si=0.2 mol/L). During the hydrolysis reactions, the TiO_2-SiO_2 sol was stirred at RT for 3 hours. A pH of 2 to 3 was measured at this step. After the hydrolysis reaction, the TiO_2-SiO_2 sol was aged for 24 hours at RT.

The chemical composition of the substrate used in this investigation is summarized in Table 4.1. Before applying the coatings, the surface of the substrate was grinded using different silicon carbide grit papers from 80 to 4000. A polishing was then performed using an alumina suspension with grain sizes of 1µm and 3µm and finally a colloidal silica suspension (OP-S).

After polishing, the substrate was cleaned in an ultrasonic bath of acetone for 20 min. C45E steel without the ceramic coating was taken as a reference sample (RS). To directly compare the RS against the performance of the coated samples, the RS was annealed at different temperatures and atmospheres that are used to produce ceramic-coated steel samples.

Table 4.1. The chemical composition of the RS (C45E), wt.%.

Elements	***Al***	***Ni***	***Mn***	***Mo***	***Cr***	***S***	***C***	***Si***	***Fe***
wt.%	0.01	0.09	0.65	0.02	0.09	<0.030	0.45	0.25	Balance

4.2.2. Preparation of TiO_2-SiO_2 Protective Coating

For deposition of the TiO_2-SiO_2 films by dip-coating, the steel substrate was dipped at a constant rate of 20 cm/min in the aged TiO_2-SiO_2 sol. After complete immersion, the samples were kept in the sol for 5 min and pulled out at a rate of 20 cm/min. For coating more than one layer (two and three), the sample was dried at RT for 30 minutes (first drying) after every layer of coating. Final drying was carried out by heating the samples to 120 °C at a heating rate of 1 °C/min for 30 minutes (second drying). The dried samples were annealed for 1 hour using a heating and cooling rate of 4 °C/min at different temperatures and in different atmospheres as summarized in Table 4.2.

Table 4.2. Different processing parameters of the investigated protective ceramic coatings on a C45E steel substrate.

Annealing Atmosphere	***Argon***	
Number of Layers	Temperature	Sample name
1 Layer (1L)	700 °C-800 °C-900 °C	1L700Ar-1L800Ar-1L900Ar
2 Layer (2L)	700 °C-800 °C-900 °C	2L700Ar-2L800Ar-2L900Ar
3 Layer (3L)	700 °C-800 °C-900 °C	3L700Ar-3L800Ar-3L900Ar
Annealing Atmosphere	***Air***	
Number of Layers	Temperature	Sample name
1 Layer (1L)	700 °C-800 °C-900 °C	1L700Ai-1L800Ai-1L900Ai
2 Layer (2L)	700 °C-800 °C-900 °C	2L700Ai-2L800Ai-2L900Ai
3 Layer (3L)	700 °C-800 °C-900 °C	3L700Ai-3L800Ai-3L900Ai

4.2.3. Characterization of Coatings

Simultaneous thermal analysis (STA) including thermal gravimetric analysis (TGA) and differential thermal analysis (DTA) were used to investigate the structural degradation of the precursors and to determine the appropriate annealing temperature for the coatings. To do so, approximately 90 mg of the TiO_2-SiO_2 gel that had dried for 1 hour at 100 °C was placed in a ceramic crucible and measured with the TGA instrument (model Netzsch 449-F1 Jupiter, Selb, Germany). The analysis was performed from RT to 1000 °C at a heating rate of 5 °C/min in an air atmosphere. The infrared spectrum with Fourier transform (FT-IR) was obtained with a Bruker Alpha FT-IR spectrometer equipped with ALPHA‘s Platinum single reflection diamond ATR module in the range of 375-7500 cm^{-1} and at a resolution of <2 cm^{-1}. In vibrational spectroscopy, the principles are based on measuring the vibrational frequency of interatomic chemical types. The functional groups and the type of transplantation in the molecule were investigated based on FT-IR spectroscopy.

To determine the surface morphology of the thin films, scanning electron microscopy (TESCAN field emission scanning electron microscope) was used. To prevent electric charging, the samples were carbon-coated. The phase and crystalline structure of the coating were characterized by the X-ray diffraction analysis (Philips Xpert model), operated at a voltage of 40 kV and a current of 35 mA (radiation with CuKα radiation, λ =1.5406 Å). Coatings were measured over the 2θ range of 20˚-80˚ with a step size of 0.02˚. The XRD results were analyzed by PANalytical XPert HighScore Plus software.

To investigate the corrosion behavior of the thin films and uncoated sample (RS), PEP and EIS tests were carried out in an electrochemical cell in an aqueous solution of 3.5 wt. % NaCl (1000 mL). An over-saturated calomel electrode (SCE) was employed as a reference electrode, and a platinum electrode was used as an auxiliary electrode. Coated C45E and RS were used as working electrodes (WEs) with a 2.01 cm^2 surface area. The experiments were carried out based on ASTM G3-14 [320] to determine the corrosion potential (E_{corr}), corrosion current

density (I_{corr}) and polarization resistance (R_p) with a scanning rate of 1 mV/s from an initial potential of -250 to 1700 mV versus open circuit potentials. EIS tests were carried out at RT for 2 hours in a 3.5 wt.% NaCl aqueous solution. The measurements were conducted using AC signals at an amplitude of 10 mV and measurement frequencies from 10 mHz to 100 kHz at the stable open circuit potential (OCP). The values of the capacitive, diffusional and resistive elements were illustrated in three different equivalent electric circuits. ZSimpWin 3.22 software was used to analyze the EIS results. All electrochemical experiments were performed using an autolab device (model PGSTAT302N) and Nova 1.11 software.

4.3. Results and Discussions

4.3.1. Thermal Gravimetric and Differential Thermal Analysis

Figure 4.1 shows the TGA and DTA curves of the TiO_2-SiO_2 gel dried in air and the FT-IR spectrum of a coating deposited on RS annealed at 900 °C in argon (a) and air (b) atmospheres. The total weight loss percentage is detected as 75% of the primary precursor weight, which occurred in three steps. The gross weight loss of approximately 73.8% occurs from 100 °C to 140 °C is attributed to the evaporation of residual water and ethanol as well as most of the organics from TOBT and TEOS. Between 200 °C and 425 °C, two overlapping steps with a weight loss of 1.6% are observed (cf. inset Figure 4.1), which is a consequence of the decomposition of the remaining organic compounds. A small step accounting for a 0.04% weight loss could be attributed to the decomposition of nitrates from the hydrolysis agent. A broad endothermic peak is observed at 125 °C in the DTA thermogram, which coincides with the massive weight loss below 140 °C and supports the assumption of the evaporation of water and organic compounds. A relatively smaller but broader endothermic peak appears at approximately 250 °C, which coincides with the two aforementioned mass steps and supports the assumption of the decomposition of residual alkyl groups. As shown in curves (a) and (b), the volatile components in the precursor decompose. The absorption numbers in 466 cm^{-1} and 613 cm^{-1} are associated with the Ti-O and Ti-O-Ti bonds, respectively [286]. The vibration of

951 cm^{-1} corresponds to the vibration of the Si-O-Ti graft. Further, the wavenumbers 1086 cm^{-1} corresponded to the Si-O-Si bond [321,322].

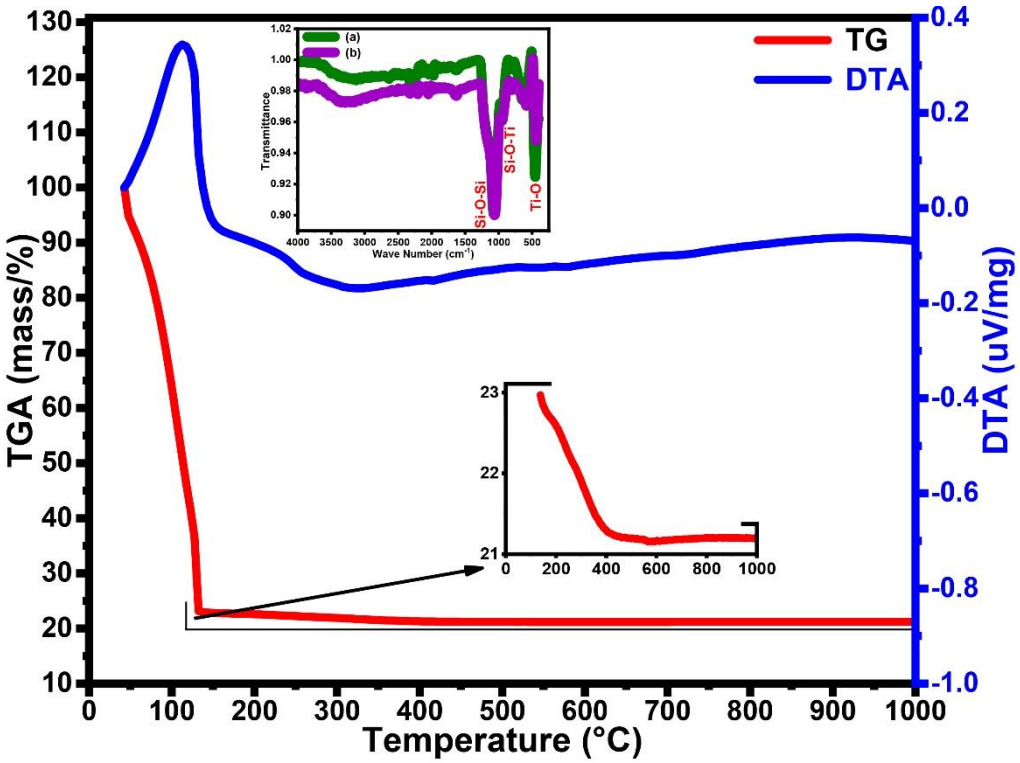

Figure 4.1. The thermal gravimetric analysis (TGA) and differential thermal analysis (DTA) curves of dried TiO_2-SiO_2 gel and the FTIR spectrum of coatings annealed at 900 °C in argon (**a**) and air (**b**) atmospheres.

4.3.2. SEM-EDX Analysis

The SEM micrographs were recorded for all the investigated protective coatings summarized in Table 4.2. The surface morphology was similar irrespective of the number of coating layers, so only 3L coatings are reported in Figure 4.2, which shows that the SEM micrographs of the TiO_2-SiO_2 3L coating at annealing temperatures of 700 °C (a,b), 800 °C (c,d) and 900 °C (e,f) in an argon atmosphere at different magnifications. It is evident from Figure 4.2 that the surface morphology is significantly influenced by the annealing temperatures. It is not feasible to obtain a continuous ceramic coating for samples annealed at 700 °C, and this is evident in Figure 4.2. The thickness of these discontinuous islets of ceramic coatings was estimated to be approximately 1µm. At 800 °C (b) and 900 °C (f), the boundaries between these islands are still present, but the surface is now covered by a dense layer. By comparing the micrographs (a), (c) and (e), it can be stated that increasing the annealing temperature led to a reduction in cracks and imperfections in the coatings. At higher magnification, it becomes visible that the coating annealed at 700 °C (b) exhibits nanometric porosity. Increasing the annealing to 800 °C (d) and then to 900 °C (f) causes progressive coagulation of the nanometric pores and enhanced grain growth. Figure 4.3 shows the SEM micrographs of the TiO_2-SiO_2 3L coatings annealed at 700 °C (a,b), 800 °C (c,d) and 900 °C (e,f) in an air atmosphere at different magnifications. The ceramic coating surface annealed at 700 °C (a) was again discontinuous with obvious cracks that are filled with material and that have grown from the substrate. This material is expected to be an iron oxide, which is proven by X-ray diffraction in the subsequent section (cf. Figure 4.5). At an annealing temperature of 800 °C (c), the surface is homogeneously covered by a nanoporous layer. Samples annealed at 900 °C (f) exhibit a heavily structured surface with deep voids, which might be caused by the coagulation of the nanopores. In both atmospheres, the surface microstructure changed as the annealing temperature increased, which is probably due to the growth of the coating components.

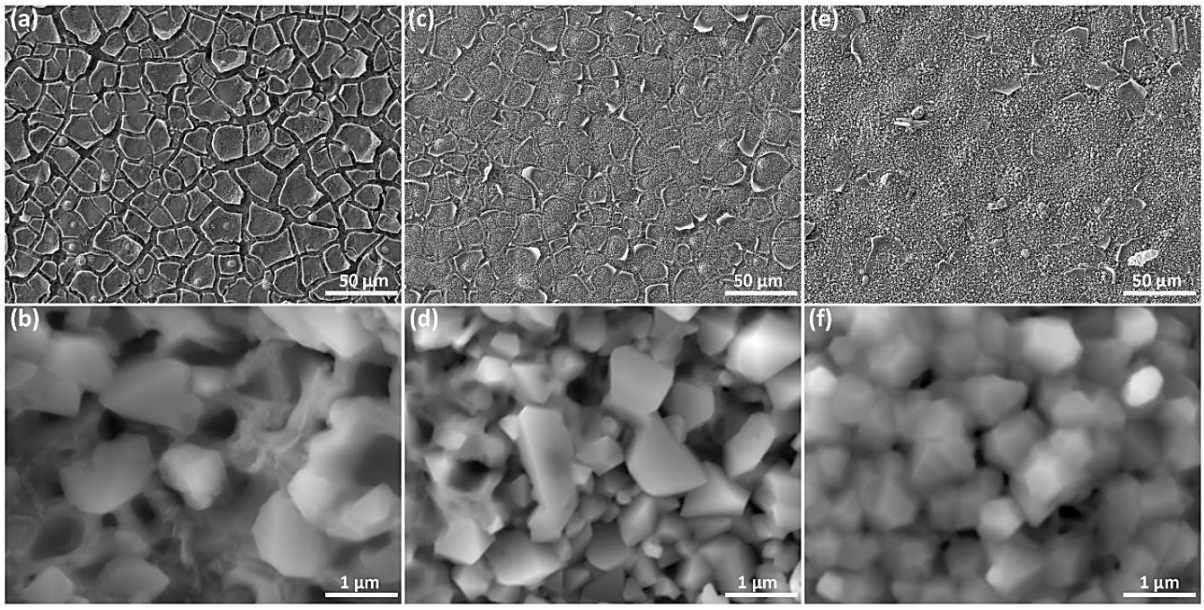

Figure 4.2. SEM micrographs of TiO_2-SiO_2 3L coatings annealed at (**a,b**) 700 °C, (**c,d**) 800 °C and (**e,f**) 900 °C in an argon atmosphere.

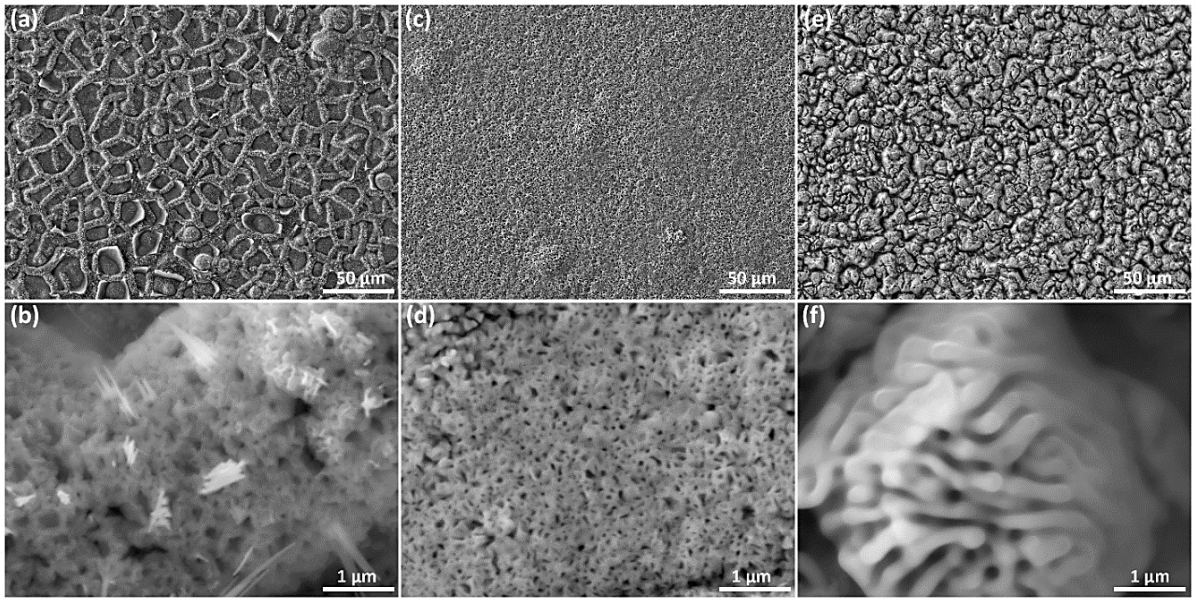

Figure 4.3. SEM micrographs of TiO_2-SiO_2 3L coatings annealed at (**a,b**) 700 °C, (**c,d**) 800 °C and (**e,f**) 900 °C in an air atmosphere.

To determine the thickness of the coating, cross-sections of the 3L coating at 900 °C under argon (a,b) and air (c) atmospheres were prepared. The films are well crystallized and dense. Three different coating layers placed one above the other are clearly identified in Figure 4.4a. As shown in Figure 4.4b, the previous cracks and pores are not seen in the cross-section of the layers. It can be said that such porosities are superficial, do not penetrate into the coating depth and are not expected to reach the substrate surface. Moreover, as shown in Figure 4.4c, the

thickness of the dense coating in the SEM cross-section was found between 3 and 4 µm. The EDX analysis of the coatings at 800 °C in the argon (a) and air (b) atmospheres is shown in Figure 4.5. TiK, SiK, FeK and OK lines were identified in the spectrum. In the coating annealed in air, more Fe is detected. This might indicate stronger oxidation of the substrate and a reaction with the TiO_2-SiO_2 compounds compared to the coating annealed in argon.

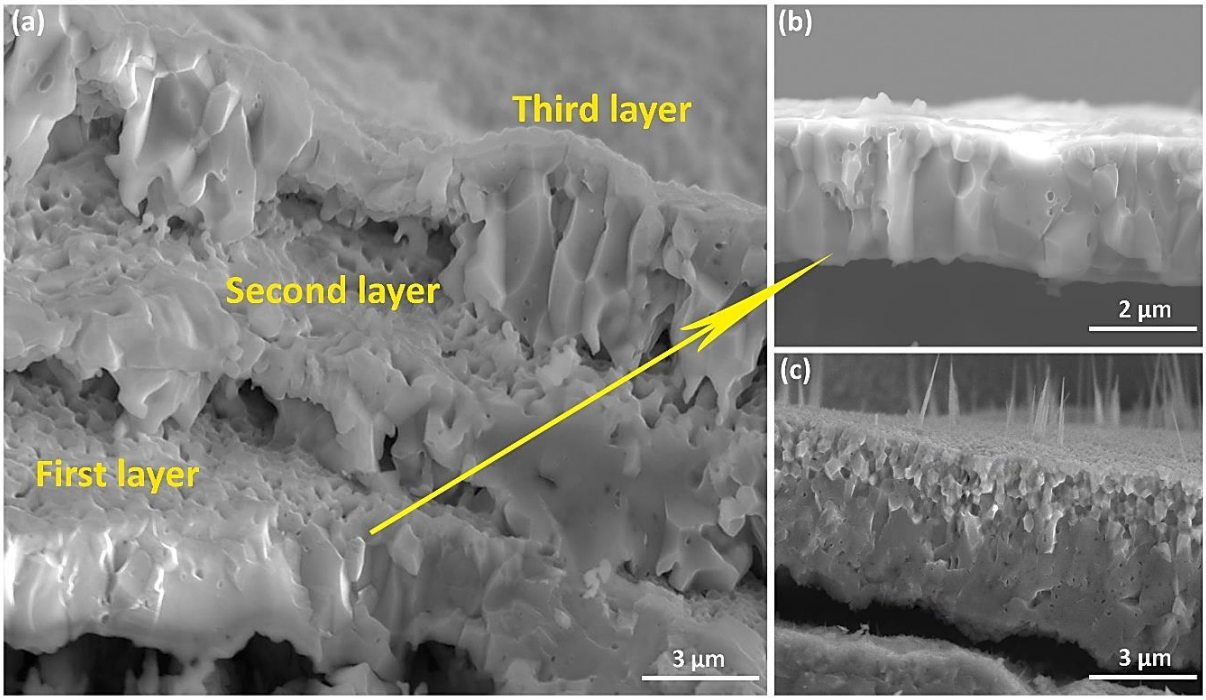

Figure 4.4. Cross-section micrographs of the TiO_2-SiO_2 3L coating annealed at 900 °C in argon (**a,b**) and air (**c**) atmospheres.

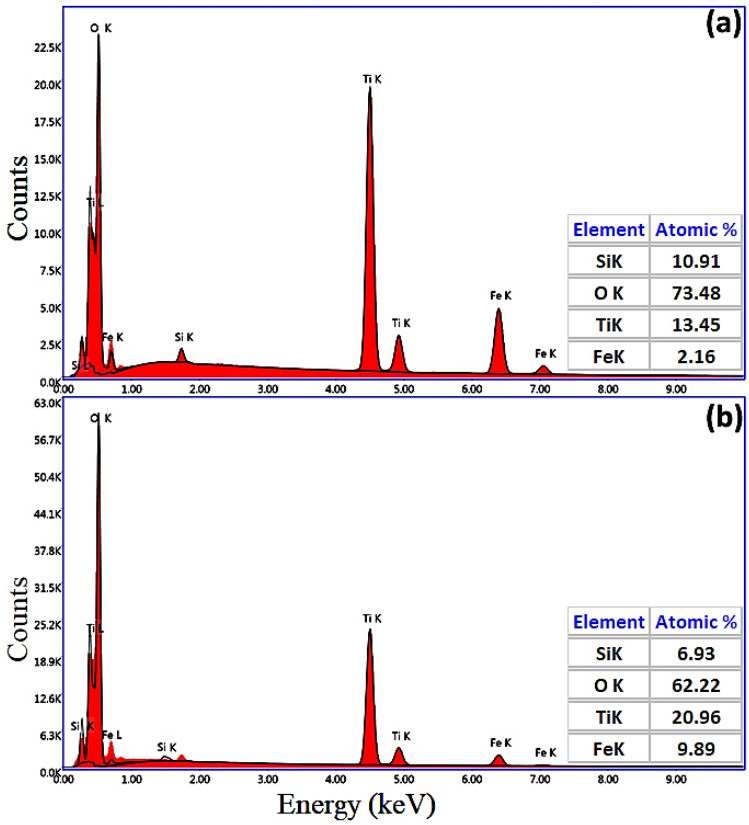

Figure 4.5. EDX analysis of TiO_2-SiO_2 3L coatings at 800 °C in argon (**a**) and air (**b**) atmospheres.

4.3.3. X-ray Diffraction Analysis

Figure 4.6 shows the X-ray diffraction patterns of the 3L TiO_2-SiO_2 coatings under the argon (a) and air (b) atmospheres and the TiO_2-SiO_2 gel (c) and RS (d), which were both annealed at 900 °C in an air atmosphere. The coating annealed in argon (Figure 4.6a) at this temperature includes two phases of hematite (Fe_2O_3, 00-024-0072) and magnetite (Fe_3O_4, 01-089-0688). If we include titanium (which was found by EDX) into the search database, we could also match a pattern of $Fe_{2.75}Ti_{0.25}O_4$, which is identical to Fe_3O_4. The narrow XRD peaks reflect the high crystallinity of the coatings. On changing the annealing atmospheres, the relative intensity of the peaks changes. The coating annealed in the air (Figure 4.6b) at this temperature shows mainly Fe_2O_3 (00-024-0072), with only faint traces of Fe_3O_4, which is an effect of the higher oxygen partial pressure. Annealing the TiO_2-SiO_2 gel in air at 900 °C yielded a powder with an anatase phase pattern (01-078-2486, Figure 4.6c). Because no TiO_2- or SiO_2-related phases

were detected in the coatings, one can conclude that solid solutions are formed with the present iron oxides. After annealing the RS in air at 900 °C only peaks of iron could be identified.

The results demonstrate that the properties of the iron oxides formed on the surface are affected by the pH of the TiO_2-SiO_2 sol and the annealing conditions at high temperatures. According to the pH-potential diagram of the iron-water system with 10^{-6} M iron at 25 °C [323], as the pH increases, compact and passive iron oxides can be gradually formed on the C45E steel surface (RS) when iron reacts with electrolytes such as the TiO_2-SiO_2 sol. These iron oxides grow during annealing depending on the oxygen partial pressure (more in the air atmosphere, less in the argon atmosphere). Then, the newly formed iron oxides mix with the TiO_2-SiO_2. Before the dipping process, there are no activation reactions, therefore, the XRD result of the RS shows only iron peaks.

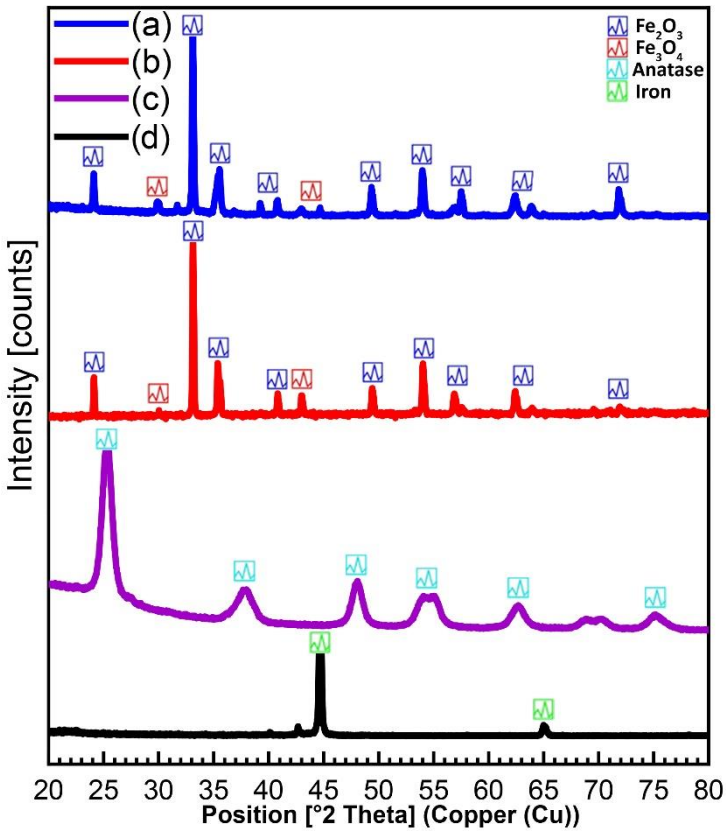

Figure 4.6. XRD patterns of TiO_2-SiO_2 3L coatings in argon (**a**) and air (**b**), TiO_2-SiO_2 gel annealed at 900 °C (**c**) and RS (**d**) annealed at 900 °C in air atmosphere.

4.3.4. Corrosion Behavior

4.3.4.1. Linear Polarization

The corrosion behavior of the TiO_2-SiO_2 coatings in a 3.5 wt.% NaCl aqueous solution was investigated by a PEP test and compared to the corrosion behavior of RS. The Tafel plots of all the investigated protective coatings are shown in Figure 4.7. The analysis of the Tafel plots yielded the slope of the cathodic curve (β_c), the slope of the anodic curve (β_a), I_{corr} and E_{corr}. These parameters were used to determine the R_p from the Stern-Geary Equation (4.1) [303].

$$R_p = \frac{\beta_a \times \beta_c}{2.303 \times (\beta_a + \beta_b) \times I_{corr}} \qquad \text{(Eq 4.1)}$$

The values derived from Figure 4.7 using Equation (4.1) are summarized in Table 3 and shown in Figure 4.8. First, the corrosion resistance of RS (uncoated C45E steel, heat-treated) was investigated. After heat treatment at 900 °C in argon, the PEP measurement of the RS yielded an R_p value of 1075 Ω cm^2, whereas heat treatment at 900 °C in air yielded a value of 2346 Ω cm^2 (cf. Table 4.3). As seen in Table 4.3, the application of the TiO_2-SiO_2 coating on the C45E steel substrate reduced the corrosion current density by approximately one order of magnitude and increased the polarization resistance of the samples. The highest Rp value of 42 kΩ cm^2 was achieved for RS coated with a TiO_2-SiO_2 ceramic protective coating consisting of 3 deposited layers annealed at 900 °C in an argon atmosphere. In the samples with TiO_2-SiO_2 coatings annealed in an argon atmosphere, the lowest corrosion current density and the highest polarization resistance were related to the coating of 3L at 700 °C, 800 °C and 900 °C. The PEP results of the coated samples are listed in Table 4.3.

Figure 4.7d,e,f shows the PEP results of all the investigated TiO_2-SiO_2-based protective coatings, as summarized in Table 4.2. As shown in Table 4.3, the lowest I_{corr} and the highest R_p were measured for 3L at 700 °C, 800 °C and 900 °C. The corrosion current density in these coatings is 5.4×10^{-6} A/cm^2, 2.6×10^{-6} A/cm^2 and 4.9×10^{-7} A/cm^2, respectively. Furthermore, among all coatings annealed in the air atmosphere, the highest R_p value is applicable to the 3L

coatings produced at 900 °C (cf. Table 4.3). The coating R_p value was approximately 61 kΩ cm^2, which is 25 times the measured values for a RS under similar conditions. Therefore, it can be concluded that by applying coatings on the RS, the E_{corr} became more positive, lowering the I_{corr} and increasing the polarization resistance. Obviously, increasing the number of layers prevents the corrosive process from extending down to the substrate surface and ultimately increases the corrosion resistance. As shown in Figure 4.8, the R_p value increased as the annealing temperature increased. This is possibly due to the increase in the grain size, the decrease of the number of grain boundaries and the increase in the density of the films. Furthermore, at all temperatures, the use of the air atmosphere increased the R_p value compared to argon atmosphere, which may be due to differences in the created microstructures and the difference in the total layer thickness. The formation of iron oxides during the annealing of the coatings is confirmed through XRD. The improved corrosion resistance is due to the stabilization of these compounds by reaction with TiO_2-SiO_2. As shown in the EDX result (Figure 4.5a), annealing in the air atmosphere increases the iron and titanium oxides, which increases the corrosion resistance.

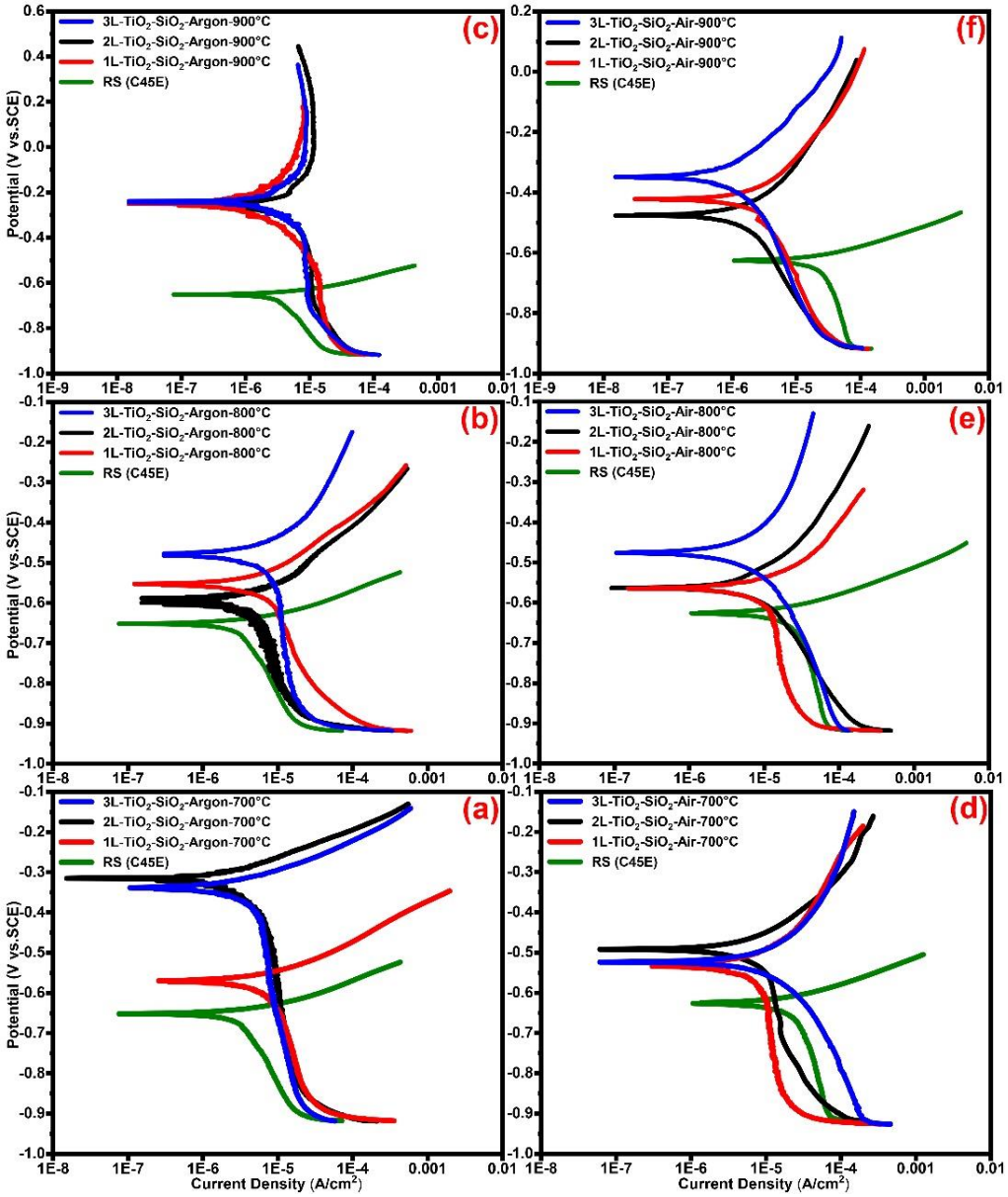

Figure 4.7. PEP curves of C45E steel substrate with TiO_2-SiO_2 coatings of 1, 2 and 3L in argon and air atmospheres at 700 °C (**a,d**), 800 °C (**b,e**) and 900 °C (**c,f**).

Table 4.3. Electrochemical parameters of RS and 1, 2 and 3L TiO_2-SiO_2 coatings annealed in argon and air atmospheres at different annealing temperatures in 3.5 wt.% NaCl aqueous solution.

Parameters		***β_a (V/dec)***	***β_c (V/dec)***	***E_{corr} (V)***	***I_{corr} (A/cm^2)***	***R_p ($\Omega\ cm^2$)***
Samples		*Argon atmosphere*				
RS		0.47	0.07	-0.59	1.5×10^{-5}	1075
700 °C	1L	0.07	0.27	-0.57	5.3×10^{-6}	4521
	2L	0.07	0.17	-0.31	3.3×10^{-6}	6305
	3L	0.06	0.21	-0.34	2.1×10^{-6}	8386
800 °C	1L	0.13	0.25	-0.55	5.1×10^{-6}	7381
	2L	0.08	0.20	-0.60	2.7×10^{-6}	9319
	3L	0.02	0.02	-0.79	4.2×10^{-7}	10431
900 °C	1L	0.30	0.28	-0.25	2.8×10^{-6}	22010
	2L	0.20	0.17	-0.24	1.5×10^{-6}	26162
	3L	0.28	0.20	-0.25	1.2×10^{-6}	41913
Samples		*Air atmosphere*				
RS		0.05	0.43	-0.65	4.8×10^{-6}	2346
700 °C	1L	0.04	0.05	-0.45	1.9×10^{-6}	5021
	2L	0.03	0.04	-0.49	1.3×10^{-6}	6548
	3L	0.27	0.11	-0.47	5.4×10^{-6}	6649
800 °C	1L	0.05	0.07	-0.80	5.9×10^{-6}	2162
	2L	0.10	0.08	-0.56	3.0×10^{-6}	6423
	3L	0.12	0.11	-0.48	2.6×10^{-6}	9386
900 °C	1L	0.11	0.19	-0.42	1.1×10^{-6}	26916
	2L	0.10	0.13	-0.47	7.4×10^{-7}	35383
	3L	0.14	0.13	-0.35	4.9×10^{-7}	60920

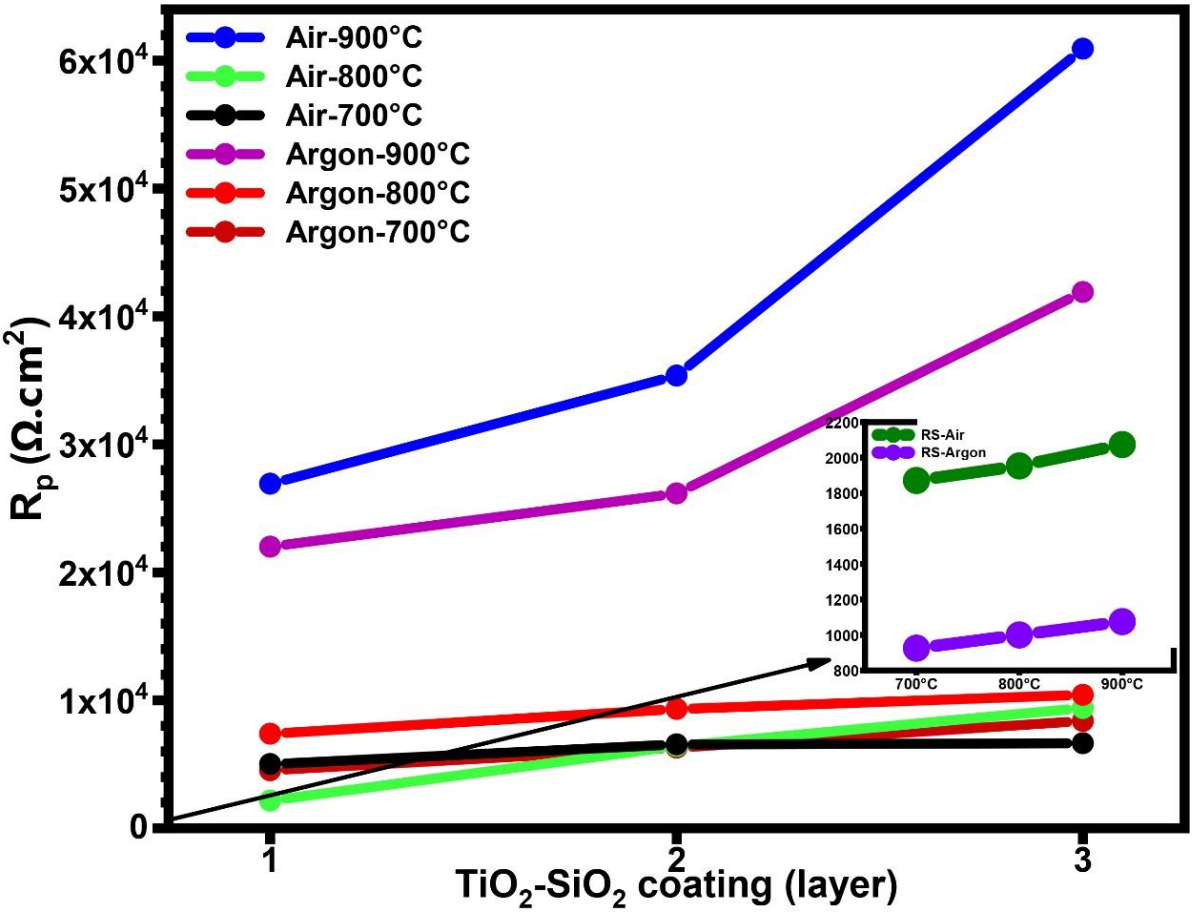

Figure 4.8. Graphical representation of TiO_2-SiO_2 1, 2 and 3L coatings and RS in argon and air atmospheres at 700 °C, 800 °C and 900 °C.

4.3.4.2. Electrochemical Impedance Spectroscopy

EIS was used to inspect the corrosion behavior of the TiO_2-SiO_2 coatings and the RS. In Figure 4.9, Nyquist diagrams from EIS for 1L, 2L and 3L coatings at different annealing temperatures in argon (a,b,c) and air (d,e,f) atmospheres are compared with the RS in a 3.5 wt.% NaCl aqueous solution. It is clear from all the Nyquist diagrams that compared to the RS, the addition of the TiO_2-SiO_2 coatings increases the semicircular diameters, which indicates an increase in corrosion resistance. It is seen that changing L and annealing at different temperatures and atmospheres change the shape and diameter of the semicircles, which indicates a change in the corrosion behavior of the coatings. The equivalent electrical circuit was used to obtain the values for the Nyquist chart parameters in the EIS test. The most suitable circuit that conforms very closely to the results obtained from the impedance tests of the coatings is schematically illustrated in Figure 4.10, while the highest equivalent circuit parameters values are listed in Tables 4.3 and 4.4. In general, three different circuitries were obtained for the coatings produced under different conditions. Figure 4.10a shows the equivalent circuit related to the RS and the coatings with codes, 1L annealed at 700 °C, 800 °C and 900 °C in argon and air atmospheres. According to the equivalent circuit, (R_s) represents the solution resistance, (R_{ct}) is the coating resistance and (CPE) is a constant phase element. An indication of the resistance to load transfer resistance, (Q) and (n) displays magnification and power of the CPE. In the equivalent circuit, the constant phase element Q, which represents a non-faradic electrode component, is in parallel with the load transfer resistance R_{ct}, and the entire series is set with the dissolved R_s resistance. In this equivalent circuit, there is a constant phase which is a function of the frequency angle (ω). The identity and impedance of this element are given by Equation (4.2) and Equation (4.3).

$$Y_{CPE} = Y_0 \times (j\omega) \qquad \text{(Eq 4.2)}$$

$$Z_{CPE} = \frac{1}{Y_0 \times (j\omega)^n} \qquad \text{(Eq 4.3)}$$

where (j) is an imaginary number, $j=-1^{1/2}$ and $\omega=2\pi f$ is the frequency angle. Factor n specifies the CPE power, with parameters between (-1) and (1). n=1 for pure capacitive behavior, n=-1 for pure inductive behavior and n=0 for pure resistance behavior. If n is between 0 and 1, the element has a constant phase of the resistor-capacitor behavior (RC), and if n is between 0 and -1, then the element has a constant phase of the resistor-inductor behavior (RL). According to all coatings, Tables 4.4 and 4.5 and the n values, it can be concluded that because the CPE power is between 0 and 1, the behavior of the constant element is RC [324,325]. This power is close to one in samples with coatings, and thus, the constant phase element shows capacitive behavior. In Figure 4.10b, the equivalent circuit for the TiO_2-SiO_2 coatings are related to 2L annealed at 700 °C, 800 °C and 900 °C in argon and air. Furthermore, Figure 4.10c shows the equivalent circuit for coatings with codes 3L annealed at 700 °C, 800 °C and 900 °C in argon and air, which consists of three load transfer resistances and three elements of the phase element. Adding these elements indicates the entry of ions and a corrosive solution to the lower layers of the coating, which is due to the presence of cracks and holes in the coatings. In other words, the lower barrier layers counteract the passage of the corrosive material to the substrate, which increases the corrosion resistance. By comparing the impedance spectra in all the coatings and the values obtained, it can be noted that the Nyquist diagrams for the coatings produced at 900 °C in argon and air included a larger circular diameter, indicating the higher corrosion resistance of such coatings. Finally, it can be concluded that the Nyquist diagrams obtained from the EIS tests were consistent with the PEP results to a great extent.

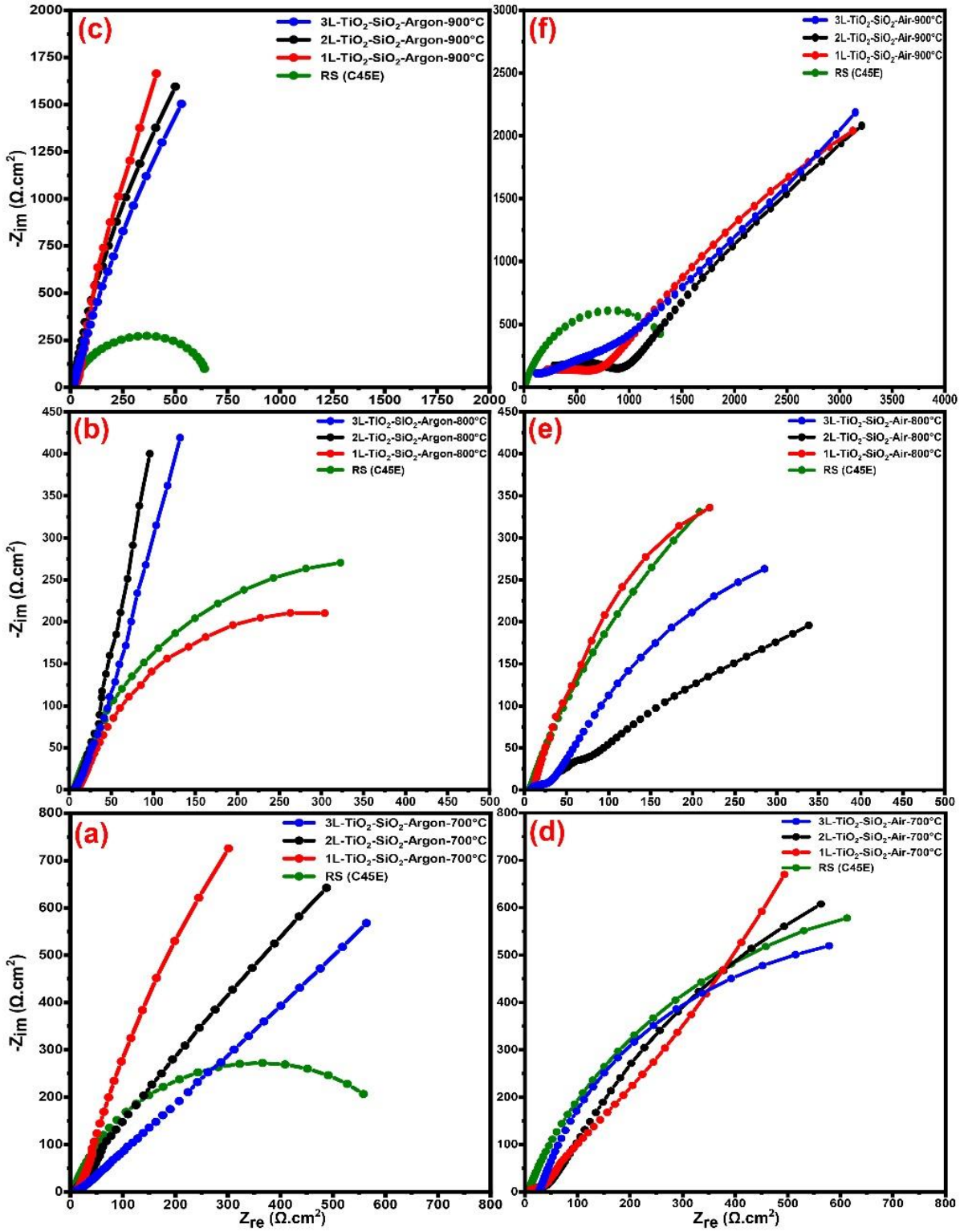

Figure 4.9. EIS of 1, 2 and 3L TiO_2-SiO_2 coatings annealed at 700 °C (**a,c**), 800 °C (**b,d**) and 900 °C (**c,f**) in argon and air atmospheres compared to the uncoated to the RS.

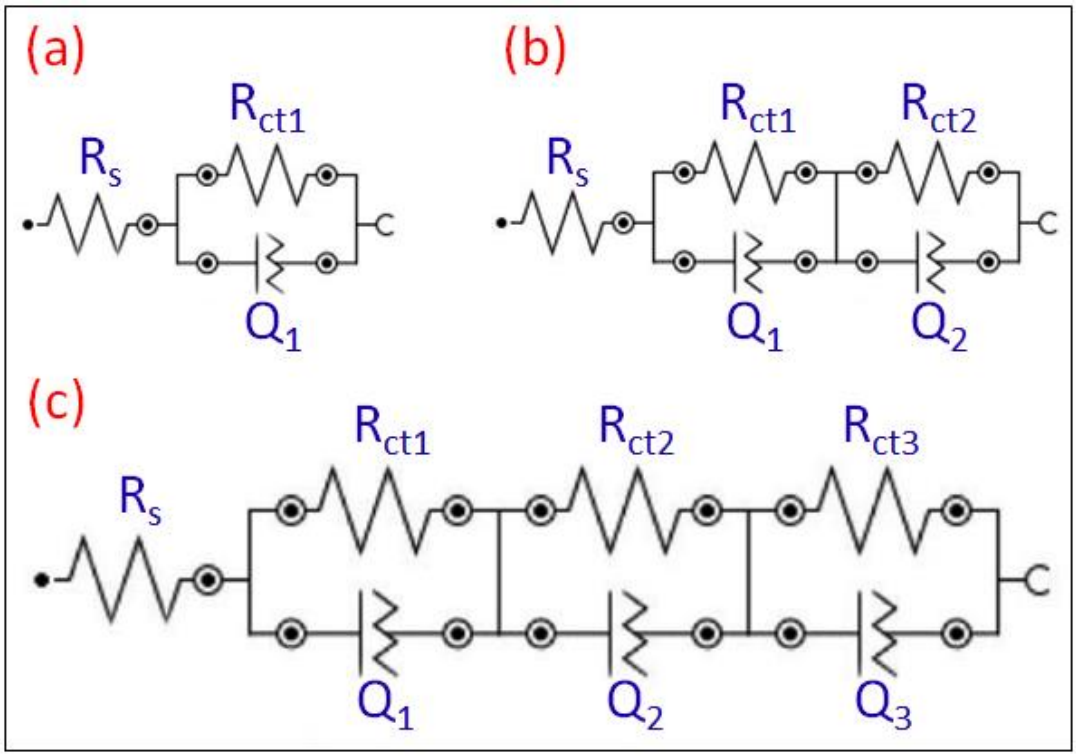

Figure 4.10. Equivalent electrical circuits for impedance data: 1L (a), 2L (b) and 3L (c) and RS annealed at 700 °C, 800 °C and 900 °C in argon and air.

Table 4.4. The values of the equivalent circuit elements coinciding with the impedance spectra of 3L of TiO_2-SiO_2 coatings annealed at 700 °C, 800 °C and 900 °C in an argon atmosphere compared to the RS.

Temperatures	***900 °C***	***700 °C***	***800 °C***	***900 °C***
Samples	*RS*	*3L*	*3L*	*3L*
R_s ($\Omega\ cm^2$)	3	1.1	7	8
Q_1 ($S\ cm^2\ s^n$)	1.4×10^{-3}	1.0×10^{-3}	4.6×10^{-4}	2.1×10^{-3}
n_1	0.8	0.5	1	0.6
R_{ct1} ($\Omega\ cm^2$)	346.4	1.4×10^{4}	1127	6181
Q_2 ($S\ cm^2\ s^n$)		1.8×10^{-2}	9.9×10^{-4}	1.1×10^{-8}
n_2		0.1	0.6	0.9
R_{ct2} ($\Omega\ cm^2$)		1.0×10^{21}	9534	5.3×10^{10}
Q_3 ($S\ cm^2\ s^n$)		1.8×10^{-13}	1.9×10^{-4}	2.6×10^{-4}
n_3		0	0.8	0.8
R_{ct3} ($\Omega\ cm^2$)		1377	1.3×10^{16}	1.6×10^{4}

Table 4.5. The values of the equivalent circuit elements coinciding with the impedance spectra of 3L of TiO_2-SiO_2 coatings annealed at 700 °C, 800 °C and 900 °C in air atmospheres compared to the RS.

Temperature	***900 °C***	***700 °C***	***800 °C***	***900 °C***
Sample	*RS*	*3L*	*3L*	*3L*
R_s (Ω cm^2)	3	6.6	7	0.1
Q_1 (S cm^2 s^n)	9.1×10^{-4}	2.3×10^{-3}	2.7×10^{-4}	6.4×10^{-5}
n_1	0.8	1	0.7	0.5
R_{ct1} (Ω cm^2)	788.3	5497	887	9657
Q_2 (S cm^2 s^n)		1.0×10^{-4}	2.8×10^{-3}	1.2×10^{-6}
n_2		0.6	0.8	0.6
R_{ct2} (Ω cm^2)		163	664	7761
Q_3 (S cm^2 s^n)		2.0×10^{-3}	1.2×10^{-2}	9.1×10^{-4}
n_3		0.5	0.4	0.8
R_{ct3} (Ω cm^2)		1.9×10^{13}	1198	7.8×10^{11}

4.4. Conclusions

In the current study, TiO_2-SiO_2 coatings (molar ratio Ti:Si=50:50) were prepared on a C45E steel substrate by dip-coating and synthesized via the sol-gel method. The effects of the number of coating layers, annealing temperatures and atmospheres of TiO_2-SiO_2 protective coatings on the structural properties and corrosion behavior of C45E steel were investigated. This systematic investigation resulted in the following observations:

- It is demonstrated that the sol-gel technique is a simple and beneficial method for preparing coatings on metal substrates.
- TGA-DTA analyses of the TiO_2-SiO_2 precursors and coatings revealed that most organic compounds are decomposed below 150 °C. Additional steps with minor weight losses were observed until 425 °C.
- The results of surface morphology imaging by SEM show that increasing the annealing temperature in both argon and air atmospheres caused a change in the surface morphology. For the annealed TiO_2-SiO_2 3L coatings in argon atmospheres, increasing the annealing temperature reduced the extent of surface cracking. The topography of the coatings is affected by annealing temperatures and atmospheres. EDX analysis confirmed the presence of Ti and Si in the coating.
- XRD analysis of the TiO_2-SiO_2 composite films revealed the presence of the Fe_2O_3 and Fe_3O_4 phases for the films annealed in argon. Annealing in air resulted in Fe_2O_3, with only small traces of Fe_3O_4. It is presumed that iron oxides, which might react with the TiO_2-SiO_2 coating are formed during the annealing process.
- In contrast to pure iron oxide coatings, which are known not to be effective against progressive corrosion, these coatings successfully served as physical and electrochemical protective barriers against corrosive attacks on the steel substrate. The results of the potentiodynamic electrochemical polarization tests indicated a significant

improvement in corrosion resistance in all coatings compared to the RS. The annealing temperatures plays a crucial role in tuning the corrosion resistance of protective coatings. Corrosion resistance is also enhanced with an increase in the number of protective coatings layers compared with the RS. The highest corrosion resistance of 61 kΩ cm^2 was obtained for the TiO_2-SiO_2 3L coating annealed at 900 °C in an air atmosphere (cf. Table 4.3).

Chapter 5

Electrochemical and Structural Property of TiSiNb TFSOC on Affordable Interconnects in Proton Exchange Membrane Fuel Cell Applications

Abstract: High cost and low electrochemical stability of the interconnection in Proton Exchange Membrane Fuel Cell (PEMFC) in the presence of H_2SO_4 are one of the main issues hindering the commercialization of these devices. This manuscript presents the utilization of cost-effective steel in an attempt to minimize the PEMFC interconnection costs with a thin-film solid oxide coating (TFSOC) providing sufficient corrosion resistance for efficient long-term operation. Novel $Ti_{0.50-y/2}Si_{0.50-y/2}Nb_{y1,2}O_2$ as TFSOC was deposited on the C45E steel as a metal interconnect utilizing a sol-gel process at various annealing temperatures. The analysis of the phase and surface morphology demonstrates that lower annealing temperatures developed nanometric crystallite size of 68 nm, more uniform structure and higher corrosion resistance. Under standard test conditions, the TFSOC demonstrated high polarization resistance (1.3 kΩ cm^2) even after 720 hours (h). Electrical conductivity of the TFSOC as low as 1.4×10^{-2} $(\Omega\ m)^{-1}$ and activation energy of 0.20 eV were achieved, which helps to maintain the PEMFC output power.

5.1. Introduction

Proton Exchange Membrane Fuel Cells (PEMFC) are getting significant attention with the growing need for renewable energy and are expected to play a key role in the energy economy that is aiming for a green energy future [119]. A PEMFC is an electrochemical device that uses a hydrated Nafion membrane which is capable of converting hydrogen and oxygen to electrical energy. Schematic representation of a single stack cell of PEMFC with the highlighting of vital components and processes involved is shown in Figure 5.1a.

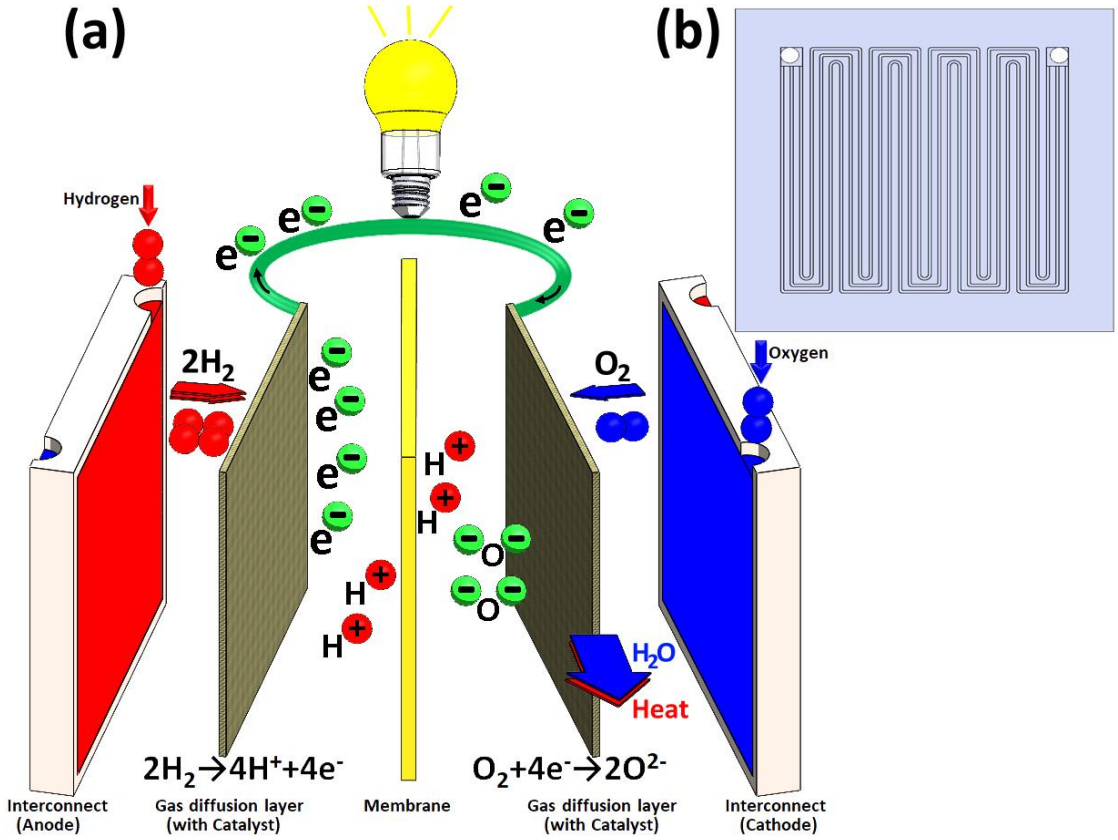

Figure 5.1. Schematic of Proton Exchange Membrane (PEM) fuel cell components (**a**) and front plane of Proton Exchange Membrane Fuel Cells ($PEMFC_{MI}$) (**b**).

In this whole energy conversion process, water is the only produced by-product, making it of great interest to alternative energy research and to replace fossil fuels [326]. Having this in mind, the development and utilization of economical and reliable fuel cells are considered to be critical aspects of attaining genuinely green or sustainable energy [327]. PEMFC is regarded as a safe and most suitable cell of choice for industrial purposes because of its modest operation

temperature. Currently available PEMFC can be operated between 80 °C and 200 °C [328]. The PEMFC interconnector ($PEMFC_I$), also known as the flow field or separator is a vital component of the PEMFC stack (depicted in Figure 5.1b) both in terms of weight and cost of the PEMFC encompassing about 80% of the total weight and 45% of the production cost of the stack [163]. These interconnectors are designed to perform several functions, such as gas flow channels, prevent hydrogen and oxygen from mixing in the fuel cell, water, and heat transmission, preventing leakage of reactants and coolant in addition to ultimately provide electrical connections [329]. The investigation of suitable and low-cost material for interconnect has emerged as a key factor in the development of the PEMFC stack. Additionally, it is important that the $PEMFC_I$ is manufactured with lightweight materials using cost-effective techniques to keep the total cost of the cell stack low. At present, materials such as electro graphite [221], carbon-carbon composite [179], flexible graphite foil [330], polymer composite [331] and metallic sheets [174] are used for $PEMFC_I$ applications. When it comes to commercial graphite $PEMFC_I$, they show outstanding resistance to corrosion and favorable electrical and thermal conductivity. However, the low density, weak mechanical strength, material and processing cost restrict its usage [195,332,333]. Metal plate-based interconnectors are usually coated with various protective materials to enhance their corrosion resistance [56,334]. The common steel compositions used for PEMFC metal interconnects ($PEMFC_{MI}$) are 304 and 316 stainless steel, which demonstrate reasonable resistance to corrosion but are costly [334]. On the other hand, these materials with good mechanical and thermal properties with a thickness of approximately 1–3 mm can significantly improve the performance and energy density of the cells [335] making the $PEMFC_{MI}$ the best potential materials for PEMFC interconnects [336]. Nevertheless, one of the serious drawbacks of $PEMFC_{MI}$ is its vulnerability to corrosion in a harsh PEMFC environment containing SO_4^{2-}, Cl^-, F^-, etc. [174] that limits the efficient long-term performance of PEMFC [185]. The corrosion of the $PEMFC_{MI}$ leads to contamination of the membrane electrodes. It can be suppressed by

passivation that in turn increases the interfacial contact resistance (ICR) and decreases the efficiency of the fuel cell stack. In recent studies, $PEMFC_{MI}$ coated with carbon-based material has been reported as a cost-effective approach to improving corrosion resistance while keeping the ICR low [238,239]. Electrically conductive polymers (ECP) were studied as potential coating materials due to their chemical and electrochemical stability [45,240]. The presence of micro-defects, as a matter of the main disadvantage of ECP, can be used as migration channels for corrosive ions to penetrate to the substrate surface and passivate interconnect, which could further increase the ICR [241,242]. Recently, some chemical inert conductive coatings, for instance, thin-film metallic glass coating (TFMGs) [243] and thin-film solid oxide coating (TFSOC) [244] have been considered as the most promising candidate coatings for $PEMFC_{MI}$ applications. The TFMGs increase the price of PEMFC due to the high cost of equipment operating and limited area [337]. TFSOC has been primarily developed to resist tribal-corrosive degradation of metal surfaces in corrosive environments. Consequently, TFSOC can be a successful applicant to satisfy the clearly stated requirements to improve the corrosion resistance of the $PEMFC_{MI}$ [220,338]. Therefore, developing cheap corrosion-resistant thin-film with appropriate electrical properties is crucial to keep the cost of PEMFC affordable. Nowadays, some TFSOC such as graphene/TiO_2 [220] chitosan-tin oxide composite film [338], Ta_2O_5 [261], Nb-TiO_2 [339], SnO_2 [260], FTO [262], Cr_2O_3/C [340], PbO_2 [341] and Zn-Ni-Al_2O_3 [342] have been investigated. These coatings have shown promising results in $PEMFC_{MI}$ applications due to their high performance as efficient corrosion inhibitors. Nevertheless, further work needs to be done to improve TFSOC to achieve a reliable and affordable coating for application in PEMFC. So far there are some studies on the application of TiO_2-SiO_2 TFSOC for corrosion protection of different substrates [286,343]. TiNb-oxide TFSOC has shown reasonable conductivity and high chemical stability at room temperature (RT) [263,344]. To summarize, the TiO_2, SiO_2 and Nb_2O_5 protective coatings have become anti-corrosive and conductive modifier materials due to of their non-toxic characteristic,

pollution-free, inexpensive and good chemical stability [263,286,343,344]. Sol-gel is proven to be a fairly simple and economical method for fabricating different organic and inorganic TFSOC for corrosion protection [345]. One main advantage of this method is its flexibility to coat large substrates of metal, glass, ceramics and plastic with a high purity protective layer using the dip-coating sol-gel technique [346]. The C45E carbon steel (AISI/SAE1045) is a commercial low-cost material (economic efficiency) commonly used due to its high strength and combination of formability that makes it easy to shape into sheets. However, several studies have been successfully performed to improve its electrochemical weakness such as corrosion resistance due to lack of chromium deficiency to operate under harsh conditions [190]. Our previous study has shown that TiO_2-SiO_2 TFSOC and its combination with C45E iron oxides after the heat treatment process have successfully served as high physical and electrochemical protective barriers (61 kΩ cm^2 compare to the 2 kΩ cm^2 as polarization resistance for the bare C45E steel) against corrosive attacks [74]. Bai et al. [192] applied chromate coating on a C45E steel surface for application as a $PEMFC_{MI}$ due to its excellent mechanical and cost-effective properties. The results demonstrated substantial protection at low and most stable corrosion current density with the lowest interfacial contact resistance of 5.9 kΩ cm^2, which indicated that the coated C45E has a significant potential to be used as $PEMFC_{MI}$ applications. Therefore, it is important to assess the potential of TFSOC on C45E surface to combine the merits of TFSOC and substrate as a low-cost alternative interconnects in PEMFC. In this work, we focused on producing a cost-effective and environmentally sustainable anti-corrosive TFSOC with long-term stability for use in $PEMFC_{MI}$ applications. For this purpose, $Ti_{0.50-y/2}Si_{0.50-y/2}Nb_{y1,2}O_2$ (TiSiNb) as TFSOC were deposited via a sol–gel process on C45E steel substrates. The influence of Nb concentration and annealing temperature (500 °C, 600 °C and 700 °C) on the morphology of the thin films were examined. The microstructure and phase of obtained TFSOC were investigated. The electrochemical

degradation behavior by means of over potential application and electrical conductivity of TFSOC through impedance analysis were also investigated.

5.2. Experimental Procedure

5.2.1. Materials and Substrate Preparation

Tetra-n-butyl orthotitanate (TBOT, $C_{16}H_{36}O_4Ti$, 98%, Merck, Billerica, MA, US), Tetraethyl orthosilicate (TEOS, $C_8H_{20}O_4Si$ 99%, Merck, Billerica, MA, US) and Niobium (V) ethoxide ($C_{10}H_{25}NbO_5$, 99.95%, Sigma-Aldrich, Taufkirchen, Germany) were used as precursors for titanium, silicone and niobium, respectively. As a solvent, hydrolysis agent and catalyst ethanol (C_2H_5OH, 99.99%, Merck, Billerica, MA, US), distilled water and nitric acid (HNO_3, 99.99%, Merck, Billerica MA, US) were used, respectively. The C45E steel with the chemical composition in accordance with EN 10083-2:2006 standard as illustrated in Table 5.1 was used as the reference sample (RS). Different silicon carbide abrasive papers (80 ground up to 4000 grit) and alumina with grain sizes of 1 μm and 3 μm (for surface polishing) were used to prepare the RS surface before applying TFSOC. Eventually, ethanol was used to clean the polished RS surface using an ultrasonic bath for 30 minutes (min).

Table 5.1. The C45E substrate chemical composition (wt.%).

Elements	***Mn***	***C***	***Si***	***Cr***	***Ni***	***S***	***P***	***Fe***
wt.%	0.65	0.45	0.27	0.25	0.25	0.02	0.04	balance

5.2.2. Preparation of TiSiNb Sol

Two $Ti_{0.50-y/2}Si_{0.50-y/2}Nb_{y1,2}$ (y = 0.01 and 0.02) sols with different Niobium (V) ethoxide (Nb) content (0.01 and 0.02) were prepared via the sol-gel method at RT. To synthesize coatings sols, TBOT, TEOS and Nb were used as precursors. Initially, to prepare the solution (A), 10 mL of TBOT was mixed with 20 mL absolute ethanol by utilizing a magnetic stirrer for 1 hour (h) at RT. The solution (B) comprising 5.8 mL of TEOS and 11.6 mL absolute ethanol was mixed in the beaker and stirred for 1 h at RT. In two separate beakers, two hydrolysis agents containing 5 mL distilled water and 2 mL nitric acid with 10 mL of absolute ethanol under severe agitation conditions (agent A) and 2.9 mL distilled water, 1.16 mL nitric acid and 5.8 mL of absolute ethanol (agent B) were stirred for 30 min at RT. Subsequently, the hydrolysis agents were added drop-wise under stirring to the A and B sols, respectively. In this step, 132 µL (y_1 = 0.01) of Nb was added dropwise to the sol (A). Following the same procedure as before, the same sols and hydrolysis agents have been prepared for another doped Nb (y_2 = 0.02) with 266 µL (pH-3 was measured). Eventually, the sols were maintained under intense stirring for 2 h to hydrolyze the precursors and aged for 24 h before deposited on the RS surfaces as TFSOC at RT.

5.2.3. Preparation of TFSOC on the Substrate

In order to deposit novel TiSiNb TFSOC, the layer-by-layer (LbL) technique [347] was used as an appropriate multi-layer coating production method due to its low cost, flexibility and durability. For this purpose, the cleaned RS was dipped at a constant rate of 10 cm/min in the TiSiNb aged sol. Following the full immersion after 2 min, the samples were pulled out from aged sol at the same constant rate speed and dried for 10 min at RT. To create the TiSiNb TFSOC three-layer (3L) this process was repeated three times. Eventually, after drying at 100 °C (3 °C/min) for 15 min the samples were annealed for 2 h at different annealing temperatures in a nitrogen atmosphere (N_2) using a heating and cooling rate of 3 °C/min as outlined in Table 5.2.

Table 5.2. Different annealing conditions and processing of the thin-film solid oxide coating (TFSOC) on the reference sample (RS) sample.

Annealing temperature	***Annealing atmosphere***	***RS***	***$Nb_{0.01}$***	***$Nb_{0.02}$***
700 °C	Nitrogen	RS-700 °C	$TiSiNb_{0.01}$-700 °C	$TiSiNb_{0.02}$-700 °C
600 °C		RS-600 °C	$TiSiNb_{0.01}$-600 °C	$TiSiNb_{0.02}$-600 °C
500 °C		RS-500 °C	$TiSiNb_{0.01}$-500 °C	$TiSiNb_{0.02}$-500 °C

5.2.4. Characterization of TFSOC

To identify the chemical decomposition of TiSiNb TFSOC precursors, thermal gravimetric analysis (TGA) and differential thermal analysis (DTA) were used. Approximately 10 mg of pre-basic material (dried gel at 100 °C for 12 h) was put within the TGA instrument (Model Netzsch, Selb, Germany) to determine the sample thermal stability and appropriate the annealing temperature. The experiment was conducted in the air atmosphere at RT up to 1000 °C (3 °C/min). In order to investigate the functional groups and molecule transplantation type of the chemical structure, an Alpha FT-IR spectrometer (Model ALPHA, Bruker, Ettlingen Germany) was acquired for the Fourier Transform Infrared Spectrum (FT-IR), which is equipped with a single-reflection ATR diamond module from ALPHA Platinum. Data were gathered between 400 to 4000 wavenumbers (cm^{-1}) with a nominal resolution of 2 cm^{-1} in a total of 200 spectra. The composition of annealed gel (powder) and TFSOC were identified by using X-ray diffraction (XRD) (MiniFlex 600 Rigaku, Tokyo, Japan) using Cu Kα radiation operated at an accelerated potential of 40 kV and the current of 15 mA with the range of 2θ = 20–80° and step width of 0.01°. The outcomes were analyzed utilizing PANalytical XPert HighScore software to accurately determine the phases and measure the crystal-size obtaining in the full width at half maximum (FWHM). The surface morphology of TFSOC was investigated by using electron microscopy (TESCAN EDS + EBSD field emission) in the secondary electron mode (10 kV). Energy-dispersive X-ray spectroscopy (EDS) was utilized to obtain microanalysis of Rs and TFSOC. To investigate the RS and SOTFC corrosion behavior, potentiodynamic electrochemical polarization (PEP) with an initial potential scanning rate of −200 to 1000 mV (1 mV/s) versus open circuit potentials (OCP) and

electrochemical impedance spectroscopy (EIS) tests were performed in standard condition solution (SCS) of 0.5 M H_2SO_4 with 2 ppm HF solution in 80 °C after 1, 24, 360 and 720 h. The over-saturated calomel electrode (SCE), platinum electrode and RS with and without TFSOC (surface area = 0.95 cm^2) were employed as a reference electrode, auxiliary electrode and working electrode (WE), respectively. The EIS measurements were carried out at the stable OCP using AC signals (amplitude of 10 mV) and measurement frequencies from 10 mHz to 100 kHz. This technique focuses on the calculation of alternating current (ac) impedance across in the frequency range for corrosion velocity analysis. Therefore, small potential time variables were applied sinusoidally around the corrosion potential to measure the impedance (Z) of the system. The PEP and EIS of the RS and TFSOC were performed according to ASTM G3-14 [348] using Autolab model PGSTAT302N, Nova 1.11 and ZSimpWin 3.22 software to determine the corrosion current density (I_{corr}), corrosion potential (E_{corr}) in the range of ±25 mV, polarization resistance (R_p) and TFSOC resistance (R_{ct}). To analyze the conductivity and activation energy (Ea) of $Ti_{0.50-y/2}Si_{0.50-y/2}Nb_{y1,2}O_2$, the Ti-Si-Nb gel was dried, compacted to pellets of 13 mm diameter by uniaxial pressing and fired at 700 °C in N_2 atmosphere. After that, gold pads were vapor-deposited on the surfaces of the pellets and impedance measurements at different temperatures between 100 °C and 700 °C were performed. A Novo control Concept 80 broadband dielectric spectrometer was used, which covered a frequency range from 0.1 Hz to 10 MHz. The conductivity was frequency independent up 1 MHz. The temperature was controlled by a thermocouple, which was positioned near the surface of the sample. For the determination of the conductivity at each temperature, the resulting Nyquist plots were fitted by a constant phase element (CPE) in parallel with a resistance element using the software ZView.

5.3. Results and Discussions

5.3.1. Thermal Gravimetric and Differential Thermal Analysis

Figure 5.2 demonstrates TGA-DTA curves of TiSiNb dried gel for 12 h at 80 °C containing different Nb content. Due to the low amount of niobium compared to other elements the results of 0.01 and 0.02 were not substantially different. The results indicate that the decomposition process of dried gel occurs in three steps. Over three steps, the overall weight loss percentage was approximately 23% of the primary precursor weight. Notwithstanding the aforementioned quantity, another weight loss occurred as a result of the removal of residual water from the TiSiNb gel in the drying process [349]. However, in the first step, approximately 3.79% of weight loss through evaporation of ethanol or combustion of organic compounds occurred between 75 °C to 175 °C [350]. The second step in 175 °C to 275 °C with a weight loss of 5.93% is ascribed to the removal of residual Ti–OH and Si–OH (unreacted hydroxyl groups) as well as carbonization [351]. The final step was a maximum weight reduction of around 12.73% at 400 °C up to 900 °C, which represents the transition of a crystalline titanium phase and physically releases water molecules bound to the silica–titanium interface region [352]. DTA data showed three significant changes (Exothermic peaks), which were contributed to the mass reduction in the dried gel. The oriented peaks at 76 °C and 150 °C were attributed to evaporation of physically adsorbed water [353] and approximately at 570 °C, the greatest peak was caused by the phase transformation of titanium from amorphous to anatase [354]. Consequently, TGA-DTA dried gel analysis may infer that the TiSiNb TFSOC transmission phase (annealing temperature) ought to be between 500 °C and 600 °C.

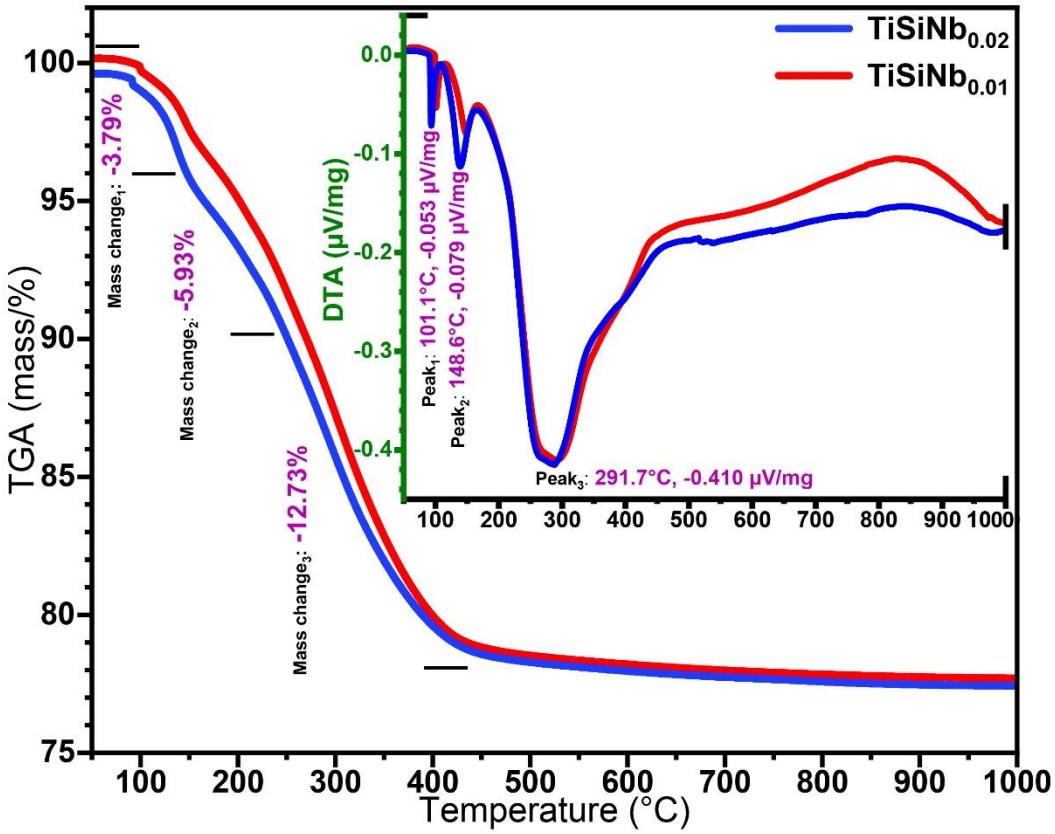

Figure 5.2. Thermal gravimetric analysis (TGA)-differential thermal analysis (DTA) curves of the TiSiNb dried gel at 100 °C for 12 h with different Nb contents.

5.3.2. FT-IR Spectra of TiSiNb TFSOC

The most recommended technique for evaluating Ti–Si bands is infrared absorption spectroscopy (FT-IR). The FT-IR spectra of TFSOC are shown in Figure 5.3.

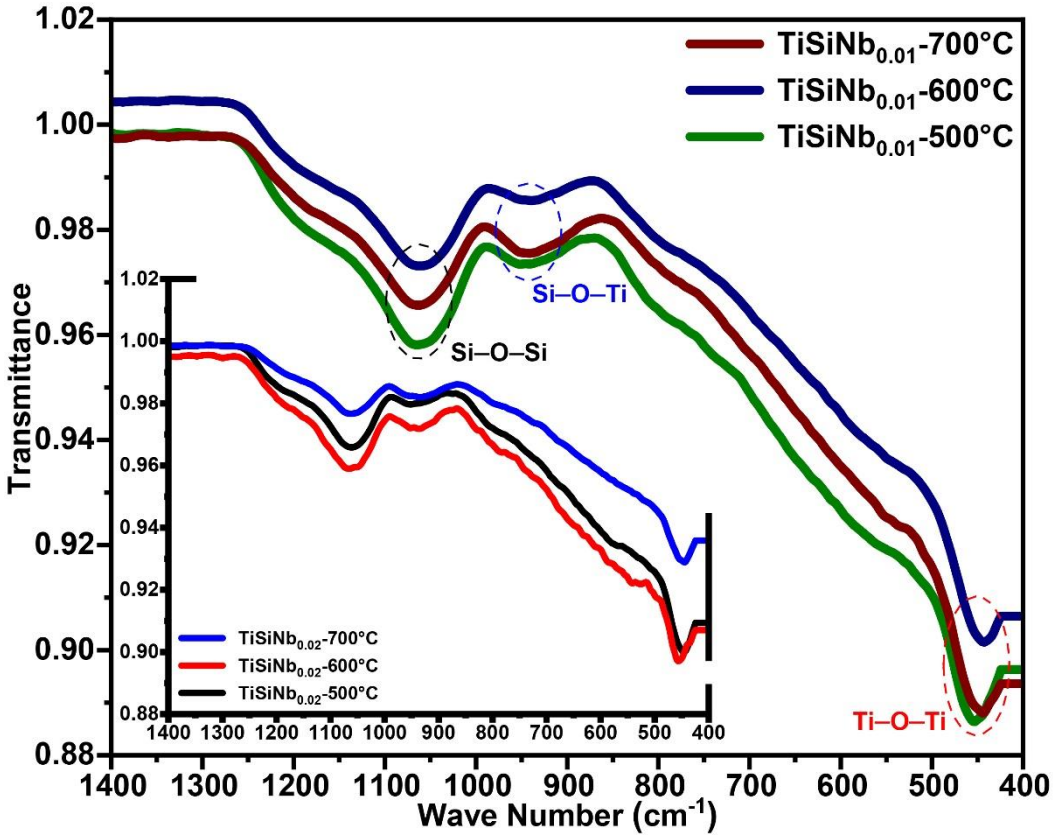

Figure 5.3. FT-IR spectra of TiSiNb annealed gel in N_2 atmosphere at different temperatures and Nb contents.

No peaks were observed in the range of 1400 cm^{-1} to 4000 cm^{-1}. It is commonly accepted that surface water adsorbed as well as the stretching vibration of OH and H_2O bands are accessible in this range [286]. This indicates that a significant fraction of the aforementioned groups exists but they have not manifested because of the low intensity of peaks and annealing atmosphere, which allows water to gradually escape the pores. The vibrations of the Ti–O–Ti and Ti–O bands connection in titanium (anatase) were assigned between 463 cm^{-1} to 468 cm^{-1} and 517 cm^{-1}, respectively [286,355]. Hydrolysis of the alcoholic group to produce Ti–OH occurs as a result of nucleophilic substitution of alkyl groups such as O–R. According to Equations (5.1)–(5.3) the –OH hydroxyl and condensation groups of Ti–OH might be produced the Ti–O–Ti with H_2O and ROH, which contributed to the formation of the gel.

$$Ti(OR)_n + nH_2O \rightarrow Ti(OH)_n + nROH \quad \text{(Eq 5.1)}$$

$$Ti(OH)_n \rightarrow Ti(O_{n/2}) + n/2\ H_2O \quad \text{(Eq 5.2)}$$

$$TiOR + TiOH \rightarrow TiO_2 + ROH \quad \text{(Eq 5.3)}$$

Furthermore, the peaks identified at 920 cm^{-1} and 950 cm^{-1} are correlated with the Si–O–Ti and Si–OH tensile vibration and the signal at 1050 cm^{-1} is referred to the Si–O–Si band, respectively [356,357]. The lack of Nb–O peak could be attributed to the low content of Niobium (V) ethoxide precursor in the sol. Therefore, all of the above results collected from the FT-IR analysis demonstrate that TiO_2 and SiO_2 have been copolymerized contributing to the formation of a homogenous inorganic hybrid xerogel.

5.3.3. SEM-EDS Analysis

SEM micrographs have been obtained for TFSOC in various annealing temperatures. Examination of either micrograph confirmed that increase the niobium content from 0.01 to 0.02 did not affect the surface morphology owing to its low content. Therefore, only the micrographs of $TiSiNb_{0.02}$ TFSOC annealed at 500 °C (a), 600 °C (b) and 700 °C (c,d) are reported in Figure 5.4.

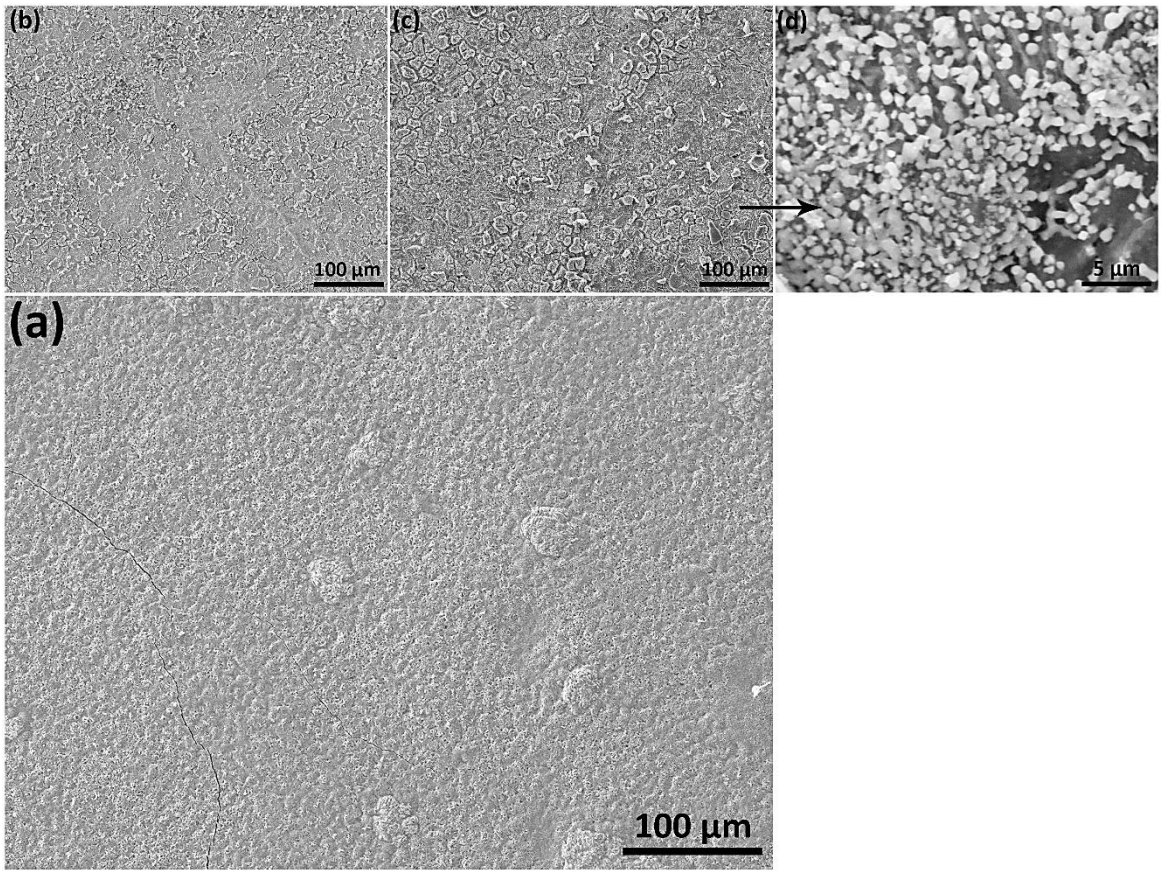

Figure 5.4. SEM micrographs of $TiSiNb_{0.02}$ TFSOC: (**a**) annealed at 500 °C, (**b**) 600 °C and (**c,d**) 700 °C in N_2 atmosphere.

Figure 5.4a reveals that the annealed TFSOC at 500 °C comprises continuous coating with just a few hairline micro-cracks, which demonstrated excellent thermal shock resistance at this temperature. However, as the annealing temperature increases from 600 °C (Figure 5.4b) to 700 °C (Figure 5.4c), the mesh of narrow elongated pits and cracks were observed in the TFSOC surfaces. As shown in Figure 5.4c, the second layer was also observed, from which might be concluded that different layers (multilayer) can be applied on the surface by the LbL

technique to raise the thickness of the TFSOC composite [286]. The other reported that the annealing temperature can be effective on the pores and cavities of the coating surface as a significant factor [358]. The size of these network cracks (12-18 μm) is increased through raising the annealing temperature probably due to the release of –OH and water bonds to the surface (cf. TGA-DTA and FTIR analysis) [359]. These results do, however, demonstrate that the RS substrate is protected inhomogeneously by the massive flaky scale of TFSOC, which may have been manufactured due to surface tension between the TiSiNb gel and atmosphere through the drying and annealing process. The researchers have also shown that during the heat treatment process in the sol-gel technique the capillary forces produced are ultimately able to establish surface fractures [359-361]. Figure 5.4d demonstrates a TFSOC micrograph which specifically illustrates that the uniform coat of nanoparticles was constructed after annealing of 700 °C. In accordance with the FT-IR (cf. Figure 5.3) and XRD (further presented in section 5.3.4) analyses, these observations might be attributed to titanium particles (anatase phase) mixed with iron oxide with an approximate size of 600 nm. Figure 5.5a indicates the cross-sectional SEM micrograph of grinded RS doped with TFSOC annealed at 700 °C in an N_2 atmosphere.

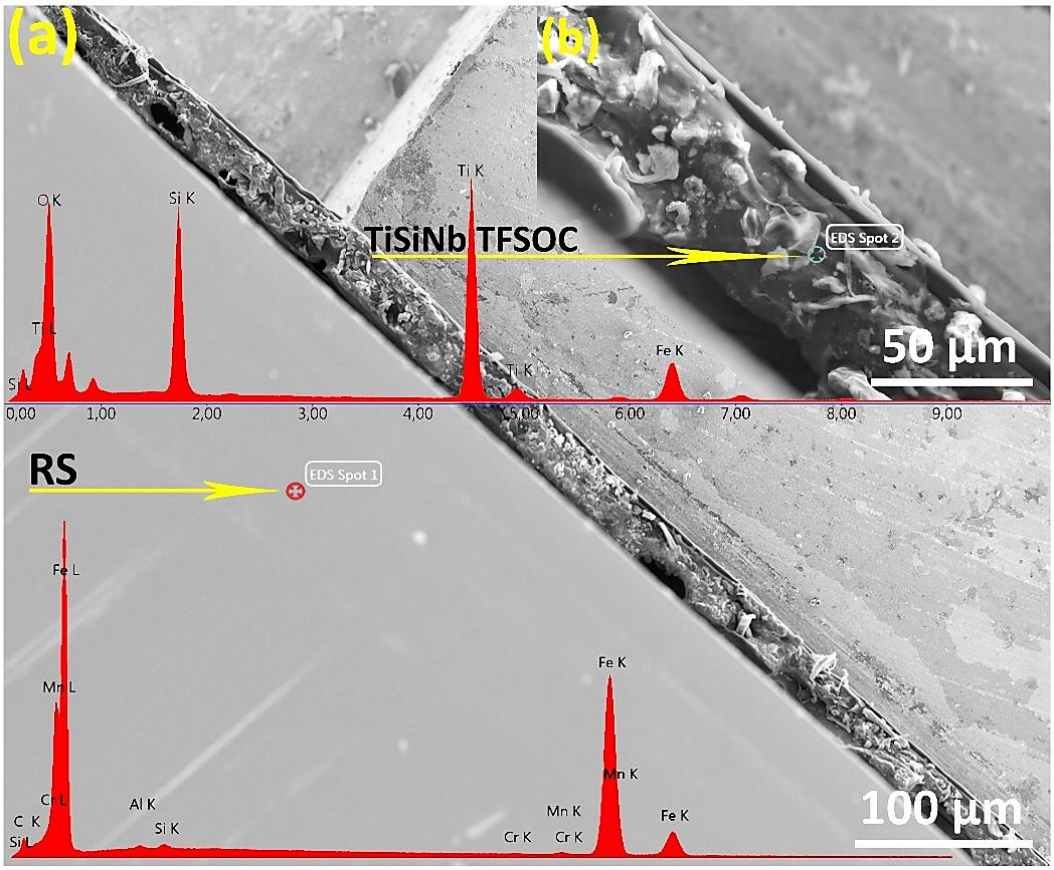

Figure 5.5. SEM micrograph (**a**) and an insert referred as (**b**) with EDS analysis of the polished cross-section of $TiSiNb_{0.02}$ TFSOC annealed at 700 °C in N_2 atmosphere.

As shown in Figure 5.5b, the cross-sections approximately reveal 76 µm of TFSOC dense structure and microcrystals of titanium anatase phase (approx. 10 µm) which is also evident on the surface (Figure 5.4d). In addition Figure 5.5a shows that the substrate is uniformly protected by TFSOC. There are also cavities between RS and TFSOC, which were randomly distributed in various sections. Since they did not reach on the surface, the area and length of these cavities are incalculable. It can be concluded that these microcavities were created during the LbL and drying steps by trapping decomposition products. This figure demonstrates also the EDS spectrum of cross-sectional RS (EDS spot 1) and TFSOC (EDS spot 2) annealed at 700 °C under N_2 atmosphere. The EDS result of the RS was matched with Table 5.1. The regular and homogeneous surface morphology of TFSOC with Ti, Si and Fe compositions at the micro-level were observed. The results show the excellently-defined peak of 0.525 keV for OK element (At%: 29.96) that demonstrated the formation of solid oxide thin-film. TiK peaks at

4.5 keV and 4.75 keV were identified which indicate the titanium dioxide existence (At%: 33.05). The peaks at 0.2 keV and 1.75 keV were identified to confirm the presence of SiK (At%: 30.59). In addition, the peak was defined at 6.45 keV to confirm FeK (At%: 6.40), which indicated that the RS penetrates to the TFSOC owing to the high temperature of the annealing process. The TFSOC compositions obtained by EDS analysis corroborate that the overall Ti:Si ratios were identical to the ratios of the corresponding sols.

5.3.4. X-ray Diffraction Analyses

The XRD patterns of TiSiNb powders (a) and TFSOC (b) annealed at various temperatures and Nb content in the N_2 atmosphere are shown in Figure 5.6.

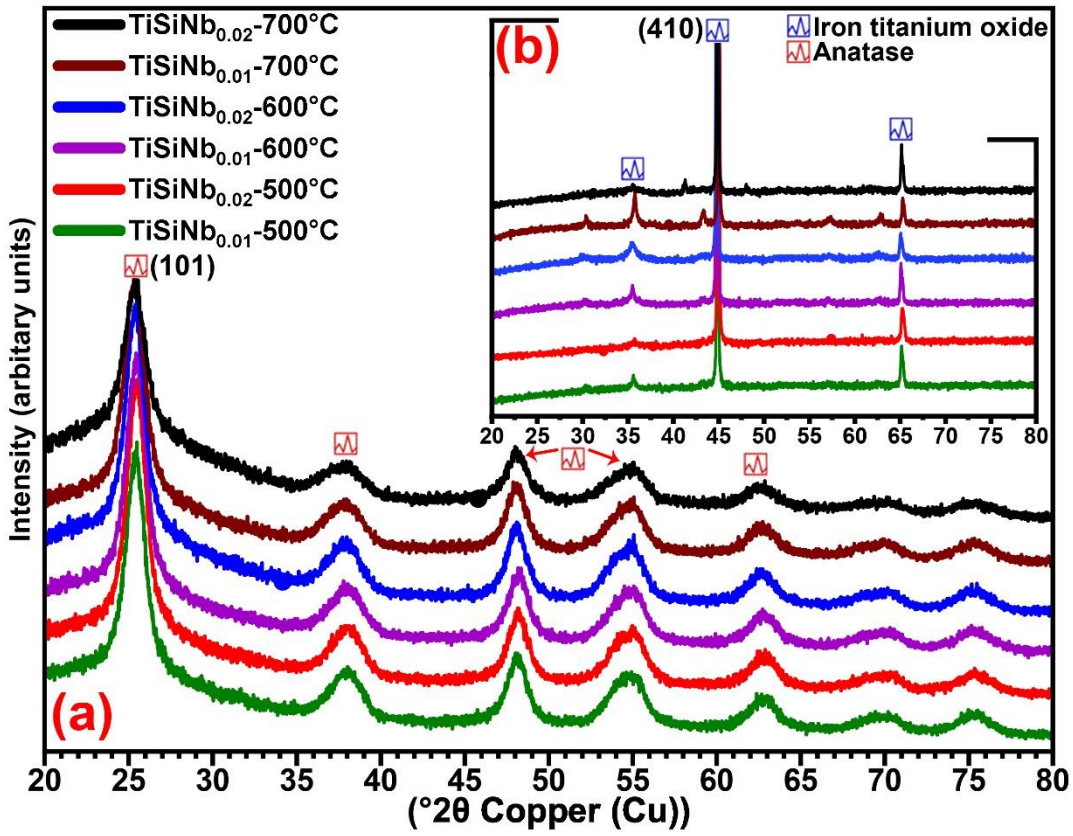

Figure 5.6. XRD patterns of TiSiNb powders (**a**) and TFSOC (**b**) at different annealing temperatures in N_2 atmosphere.

In compositions of TiSiNb powders (a), the results show that the increased temperature from 500 °C to 700 °C did not affect the peaks generated, which might be correlated with the formation and variations temperature in titanium and silicon phases [362]. It is evident that the increase in the annealing temperature resulted in increasing the intensity of the peaks and consequently forming crystallization. Only titanium oxide was detected and well-matched with the tetragonal anatase phase (01-071-1166) while silicon dioxide was not identified. In both Nb contents at the mentioned annealing temperature, the sharper peaks at 2θ = 25.34° were revealed to the (101) orientations. Considering the fact that the EDS analysis evidence demonstrates that coverings contain substantial quantities of silicon (At%: 30.59), however, due to the high annealing temperature, it can be concluded that the lack of silica composition in the XRD analysis might be attributed to its amorphous structure. To quantify the average size of TFSOC and TiSiNb nano-crystallite (L), the Scherrer Equation (5.4) [363] was utilized by K as a constant related to crystallite shape that is normally taken as 0.9 and XRD radiation of wavelength λ (nm) from measuring the full width at half maximum of peaks (β) in radian located at any 2θ in the pattern.

$$L=\frac{K\times\lambda}{\beta\times Cos\theta} \quad \text{(Eq 5.4)}$$

The average grain size of TiSiNb powders in different annealing temperatures (approx. 15 nm), was not changed with the increase of Nb content. Figure 5.6b demonstrates the XRD patterns of TFSOC at different annealing temperatures at two different Nb contents. The TFSOC XRD results were similar in all mentioned annealing temperatures. The results show that the Maghemite, titanium phase ($Fe_{2.18}O_4Ti_{0.42}$, 01-084-1595), which demonstrates the iron oxide was formed on the surface. The combination of iron oxide and titanium phases was influenced by the pH of sol precursors in accordance with the pH-potential diagram of the iron–water system at RT [364] and annealing temperature. Low carbon steel such as C45E can progressively produce passive iron oxides in precursors with high pH [365]. Consequently,

under the processes of annealing, these iron oxides were extracted and combined with TFSOC. Moreover, the XRD results of TFSOC shows that the transformation phases have not changed with increasing the annealing temperature and Nb content. The crystallite size of the maximum narrow peaks, which represented the high crystallinity of TFSOC was increased from 68 nm to 71 nm through increasing annealing temperature.

5.3.5. Studies on Corrosion

5.3.5.1. Tafel Polarization Technique and Electrochemical Behavior

In all electrochemical techniques, I_{corr} can be used to determine the rate of corrosion from the measures of polarization. The R_p of annealed RS and TFSOC at different temperatures in SCS immersion after 1, 24, 360 and 720 h were determined using the Tafel extrapolation method from the intersection of cathodic and anodic Tafel curves. For this purpose, R_p was measured using the I_{corr}, anodic (β_a) and cathodic (β_c) Tafel constants from the Stern-Geary Equation (5.5) as one of the most effective techniques.

$$R_p = \frac{\beta_a \times \beta_c}{2.303 \times (\beta_a + \beta_b) \times I_{corr}} \qquad \text{(Eq 5.5)}$$

In order to compare the corrosion behavior between the uncoated and coated RS, firstly the RS has been annealed at all mentioned temperatures in the N_2 atmosphere. Then, the PEP and EIS tests of the annealed RS were performed in the SCS after 1, 24, 360 and 720 h immersion time. After 96 h of immersion, the results showed that the uncoated RS started to oxidatize and reduce the non-uniformity of the surface which can be assumed that the localized corrosion [258] occurred in the form of irregular and deep pitting. It can be concluded that this corrosion was primarily induced by the active-passive behavior of iron due to the pH environment, regeneration of the hydrogen ion, lack of protective black oxides such as Fe_3O_4 and chromium elements in the RS (cf. Figure 5.5 and Figure 5.6). Therefore, in PEP analyses under the assumption that the distribution of anode sites is uniform and its area is equivalent to the total

sample surface area, the examination of the corrosion behavior has not yielded accurate due to the RS surface oxidation and formation of the pitting corrosion [366]. Consequently, to compare the bare and coated RS, the PEP curves of the sample after 1 h immersion in the SCS were reported in Figure 5.7a and the results are shown in Table 5.3.

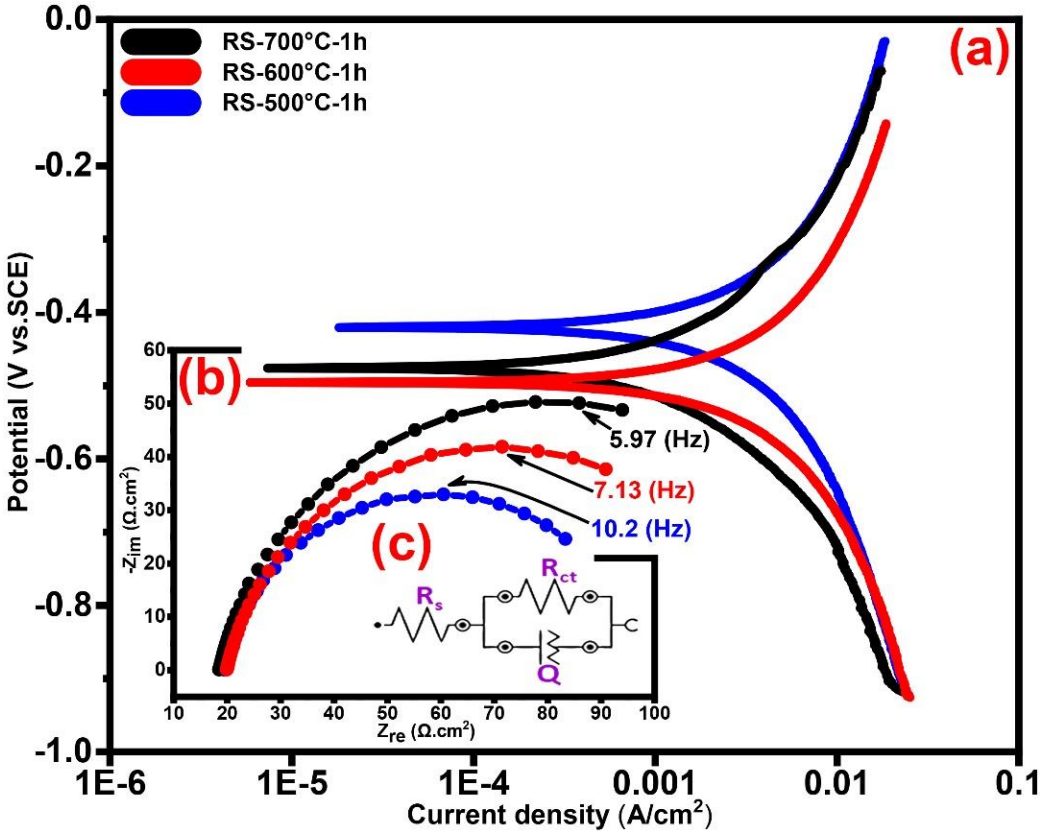

Figure 5.7. Potentiodynamic electrochemical polarization (PEP) (**a**), electrochemical impedance spectroscopy (EIS) (**b**) curves with equivalent electrical circuit (EEC) (**c**) of annealed RS at 500 °C, 600 °C and 700 °C in N_2 atmosphere after 1 h immersion in standard condition solution (SCS).

Table 5.3. Electrochemical parameters of annealed RS and TFSOC in N_2 atmospheres at mentioned temperatures after immersion for 1, 24, 360 and 720 h in SCS.

Sample	*Immersion time*	*Parameters*				
		E_{corr} *(V)*	β_a *(V/dec)*	β_c *(V/dec)*	I_{corr} *(A/cm²)*	R_p *(Ω cm²)*
$TiSiNb_{0.02}$-700 °C	720 h	−0.29.4	2.8×10^{-2}	3.2×10^{-2}	6.9×10^{-7}	9262
$TiSiNb_{0.02}$-600 °C		−0.29.5	3.3×10^{-2}	3.3×10^{-2}	7.1×10^{-7}	9681
$TiSiNb_{0.02}$-500 °C		−0.28.9	3.8×10^{-2}	4.1×10^{-2}	6.5×10^{-7}	13,285
$TiSiNb_{0.02}$-700 °C	360 h	−0.29.6	2.9×10^{-2}	3.1×10^{-2}	7.2×10^{-7}	9038
$TiSiNb_{0.02}$-600 °C		−0.29.6	4.1×10^{-2}	4.2×10^{-2}	9.5×10^{-7}	9581
$TiSiNb_{0.02}$-500 °C		−0.28.4	2.7×10^{-2}	3.1×10^{-2}	2.8×10^{-7}	21,050
$TiSiNb_{0.02}$-700 °C	24 h	−0.29.2	2.9×10^{-2}	3.3×10^{-2}	7.1×10^{-7}	9345
$TiSiNb_{0.02}$-600 °C		−0.28.7	3.9×10^{-2}	4.1×10^{-2}	7.1×10^{-7}	12,423
$TiSiNb_{0.02}$-500 °C		−0.27.9	3.6×10^{-2}	4.2×10^{-2}	3.7×10^{-7}	23,152
$TiSiNb_{0.02}$-700 °C	1 h	−0.29.5	3.1×10^{-2}	3.9×10^{-2}	7.1×10^{-7}	10,523
$TiSiNb_{0.02}$-600 °C		−0.29.4	3.6×10^{-2}	4.1×10^{-2}	6.1×10^{-7}	13,588
$TiSiNb_{0.02}$-500 °C		−0.28.1	2.9×10^{-2}	3.5×10^{-2}	2.6×10^{-7}	26,533
RS-700 °C		−0.47.5	4.9×10^{-2}	5.9×10^{-2}	5.8×10^{-6}	2030
RS-600 °C		−0.47.9	5.9×10^{-2}	6.5×10^{-2}	1.6×10^{-5}	854
RS-500 °C		−0.48.4	5.6×10^{-2}	3.7×10^{-2}	3.1×10^{-5}	326

The results indicate that the increased annealing temperature from 500 °C to 700 °C has improved the R_p from 326 Ω cm^2 to 2030 Ω cm^2, respectively. Therefore, it is conceivable to conclude that the increase in the annealing temperature resulted in the formation of the passive layer and thereby improved the RS corrosion resistance. Figure 5.8a,c,e,g shows the PEP curves of TFSOC with a different value of Nb annealed at 500 °C, 600 °C and 700 °C which were immersed in SCS for 1 (a), 24 (c), 360 (e) and 720 h (g), respectively. As the curves indicate, increasing the niobium dopant content is effective in improving the corrosion behavior of TFSOC due to its comprehensive performance such as excellent anti-corrosive performance. Therefore, based on the assumption that the results are almost the same only $y_2 = 0.02$ is reported in Table 5.3.

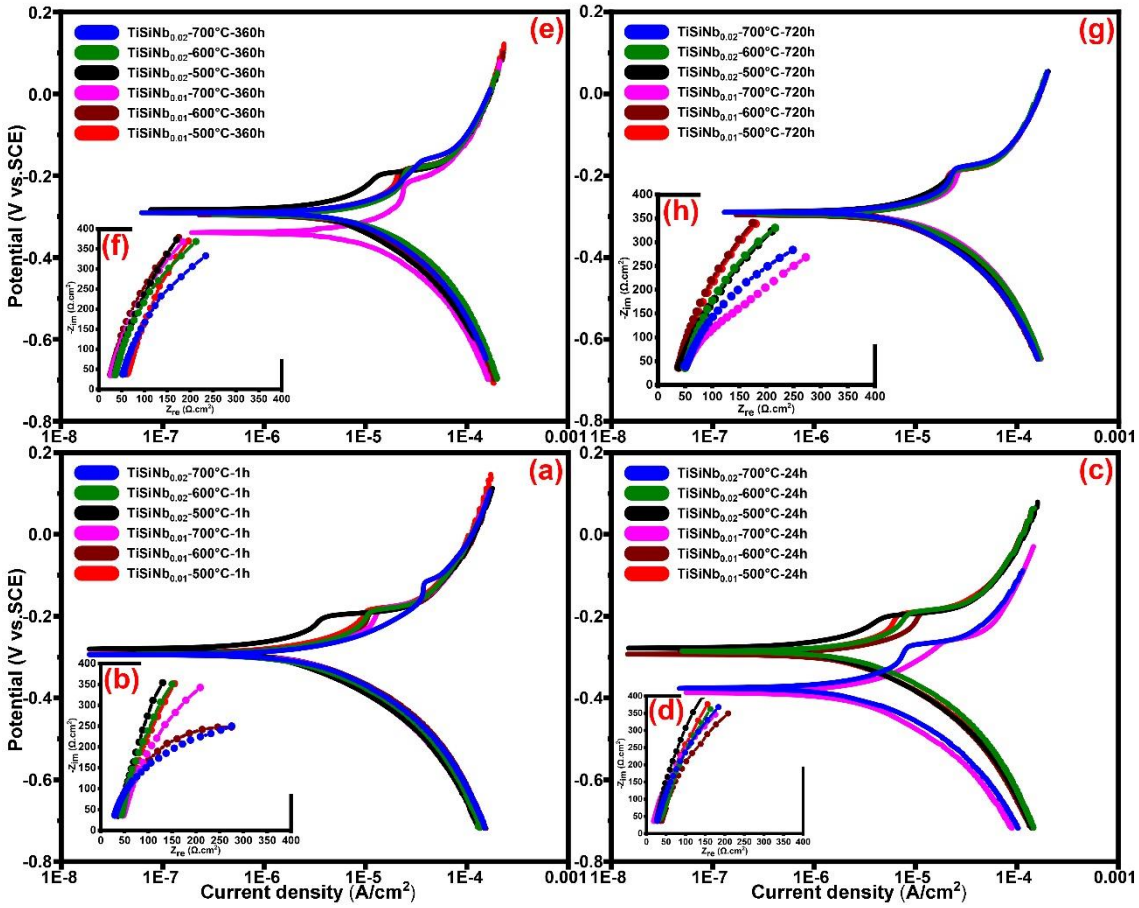

Figure 5.8. PEP (**a**,**c**,**e**,**g**), EIS (**b**,**d**,**f**,**h**) curves of annealed TFSOC at 500 °C, 600 °C and 700 °C in N_2 atmospheres after immersion in SCS for 1, 24, 360 and 720 h.

Figure 5.8a shows the PEP curves of immersed TFSOC in SCS after 1 h. As can be seen, increasing the annealing temperature from 500 °C to 600 °C and 700 °C was decreased the E_{corr} from -28.1 V to -29.4 V and -29.5 V, respectively. Therefore, the R_p of TFSOC was decreased from 26,533 Ω cm^2 to 13,588 Ω cm^2 and 10,523 Ω cm^2, respectively. The SEM micrograph reveals that TFSOC annealed at 500 °C (cf. Figure 5.4a) has fewer cracks compared to the rest of the samples. Therefore, there is the highest R_p of 26,533 Ω cm^2 at this annealing temperature due to the non-cracking surface as one of the most important subjects to acts as a barrier and prevent corrosive ions from penetrating to the substrate. Figure 5.8b indicates the PEP curves of TFSOC after 24 h immersion in the SCS, which similarly decreased the R_p from 23,152 Ω cm^2 to 9345 Ω cm^2 by increasing the annealing mentioned temperature, respectively. As can be seen in Table 5.3 the similar results were obtained from 360 h (Figure 5.8e) and 720 h

(Figure 5.8g) immersion in the SCS. Generally, the results demonstrated that the highest R_p of TFSOC was obtained from 500 °C annealed after being immersed in SCS for 1, 24, 360 and 720 h, respectively. Furthermore, as shown in Figure 5.8 and Table 5.3, after 720 h immersion, the maximum volume of decreased R_p was attributed to the TFSOC annealed at 500 °C. However, by comparing the other annealed temperatures, it can be concluded that the R_p has not decreased significantly after increasing the immersion time and their remains almost unchanged. As the annealing temperature increased, silicon dioxide is formed during the oxidation of silicon single crystal (cf. EDS result), as well as the titanium and iron oxide phases are grown. Then, due to the instability of silicon dioxide as a barrier the substrate oxides penetrated to the TFSOC surface through the nanoporous and cracks in the form of the combined titanium oxides (cf. Figure 5.6). Ultimately, to preserve the R_p stable, maybe such oxide phases behave similarly relying on the following mechanisms:

The long-term stability and superior corrosion resistance property of this TFSOC during the long-term immersion might be dependent on a variety of factors such as heat treatment atmosphere as well as the function of their electrochemical behavior in the test environment. On the other hand, the researchers have realized that the process of heat treatment in the N_2 atmosphere can increase the corrosion resistance of the bare substrate and coating [367,368]. Further, the reduction of dissolved N_2 according to Equation (5.6) can immediately be absorbed on the surface of TFSOC during the immersion in an acidic environment consumes hydrogen ions and prevents acidification of the TFSOC surface by hydrolysis of metal ions and thereby prevents the destruction of TFSOC. As shown in SEM micrograph (Figure 5.5a), there are various cavities between the RS and TFSOC which can be enriched by N_2 through metal ion deposition during RS initial contact with the TiSiNb aged sols (dip-coating process) and film formation in the heat treatment process. Finally, the N_2 is enriched in the metal at the substrate/TFSOC interface via cracks and nano-crevices, thus might be reducing the anodic dissolution rate and thus decreasing the I_{corr} (cf. Table 5.3), as a result, increasing the corrosion

resistance. In the next mechanism, the passive films can be formed on the surface due to the consecutive immersion of the RS into the precursor sols and SCS or even during the PEP and EIS tests. In this case, both anode and cathode reactions are generally assumed as Equation (5.7) and Equation (5.8), respectively. However, rather than the metal and hydroxyl ions immediately combining to form a solid product shown in Equation (5.9), due to the SCS temperature and pH, these reactions (Equations (5.7) and (5.8)) constantly repeated, which resulted in the formation of the passive film. Therefore, firstly the metal ions react with hydroxyl ions and the intermediate complex has formed as shown in Equation (5.10). Then, water molecules surrounded these intermediate ions and the solid film has precipitated after the Equation (5.11) reaction. Resultantly, the water was produced as shown in Equation (5.12) owing to the combined the produced hydrogen ions in Equation (5.11) and remaining hydroxyl ions of cathode reaction from Equation (5.8). Finally, as shown in Equation (5.13) the solid metal hydroxide is converted to metal oxide due to the presence of water ions in the PEMFC operating environment.

$N_2+4H^++3e^-\rightarrow NH_4^+$ (Eq 5.6)

$M\rightarrow M^{+2}+2e^-$ (Eq 5.7)

$1/2O_2+H_2O+2e^-\rightarrow 2OH^-$ (Eq 5.8)

$M^{+2}+2OH^-\rightarrow M(OH_2)$ (Eq 5.9)

$M^{+2}+OH^-\rightarrow M(OH^+)$ (Eq 5.10)

$M(OH^+)+H_2O\rightarrow M(OH)_2+H^+$ (Eq 5.11)

$H^++OH^-\rightarrow H_2O$ (Eq 5.12)

$M(OH)_2\rightarrow MO+H_2O$ (Eq 5.13)

Under this mechanism, freshly oxide formed film can contain a significant amount of water molecules, which can gradually decrease by continuous exposure to SCS. Eventually, the new oxide formed film progressively changes toward that of the metal with the loss of hydrogen

ions. Following the formation of the metal oxide, the metal ions at a rate corresponding to the I_{corr} passed through the passive film. As a result, the corrosion resistance can be constant over a long time in the presence of corrosive ions in the SCS. Finally, it can be concluded that the TFSOC has demonstrated high corrosion and long-lasting resistance in the SCS, which is suitable for $PEMFC_{MI}$ cost-effective applications.

5.3.5.2. Electrochemical Impedance Spectroscopy

The EIS technique was used to investigate the RS and TFSOC corrosion behavior after immersion in SCS. Investigating the characteristics of coatings protective on corrodible metals is one of EIS most usual applications. Figures 5.7b and 5.8b,d,f,h show the Nyquist plots from EIS analyses of annealed RS (5.7b) and TFSOC after immersion in SCS for 1 (b), 24 (d), 360 (f) and 720 h (h) at a mentioned temperature in N_2 atmosphere. As can be seen in Figure 5.7b, the low corrosion resistance of RS has not changed by increasing the annealing temperature. Therefore, because of the rapid oxidation of bare RS in the harsh environment, only the PEP results of 1 h at the mentioned annealing temperature are presented in this work. As shown in Figure 5.8b,d,f,h, the application of TFSOC have modified the shape and diameter of the semi-circles as compared to the RS plot (5.7b) which indicates an improvement of RS coated resistance. Furthermore, the Nyquist TFSOC plots demonstrate that the semicircular diameters were increased, which indicates a notable improvement of the corrosion resistance of the substrates after applying the TFSOC. The equivalent electrical circuit (EEC) has been used to obtain the parameter values of the RS and TFSOC Nyquist plots. As can be observed in Figure 5.1b, the gas and water flow channels are machined or stamped directly on the interconnect surface. Due to the presence of these channels, which are responsible for the homogeneous delivery and distribution of fuels, a significant portion of irreversible losses from ICR of approximately 11%, which clearly reduces PEMFC efficiency [143]. Therefore, to improve the efficiency and commercialization of PEMFCs, it is important to avoid the electrochemical

degradation of the interconnectors. On other hand, good electrical conductivity ought to be the property of $PEMFC_{MI}$. However, it seems that the high value of R_{ct} might have decreased the electroconductivity of $PEMFC_{MI}$, which can have consequences for the efficiency of the interconnectors and eventually reduce the output power of the PEMFC. Therefore, to identify the TFSOC with good load transfer intensity in addition to reasonable corrosion resistance, the lowest values of the equivalent circuit parameter of EIS results, obtained from the curve-fitting method that has been used to model the bare and coated substrates, are compared. The optimum was found for the $TiSiNb_{0.02}$ sample annealed at 700 °C. The data are reported in Table 5.4. The most appropriate circuit which has been matched precisely to the EIS results of RS and TFSOC with a low measurement error of impedance data (rel. std. error ≤0.14%) is schematically illustrated in Figure 5.7c. The Randles equivalent circuit [216] as one of the simplest and most common cell models can be used to extract information of EIS data from different protective thin-films. This model is often the basis for other more complex models which is commonly utilized when the Nyquist plot is in the form of a complete semicircle with no deviation from an ideal state. As shown in Figure 5.7c, the equivalent circuit involves the solution resistance (R_s), charge transfer (R_{ct}) and pseudocapacitance associated with the substrate-electrolyte interface (Q). In general, CPE is used to describe the capacitance, when the underlying electrochemical process is not described by a single relaxation frequency but by dispersion of relaxation frequencies (indicated by a flattened semicircle). It is specified by the (Y_0) and the power index number (n) as provided in (Equation (5.14)); where Y_0 is directly related to the active surface corrosion and electrical conductivity [369] and n is CPE power, which is attributed to the dispersion effects caused most probably by the roughness of the TFSOC surface [370]. Therefore, the identity and impedance of CPE are related to Equations (5.14) and (5.15), respectively.

$$Y_{CPE} = Y_0 \times (j\omega)^n \quad \text{(Eq 5.14)}$$

$$Z_{CPE} = \frac{1}{Y_0 \times (j\omega)^n} \qquad \text{(Eq 5.15)}$$

where $\omega = 2\pi f$ (rad/s) as an angular frequency and $j = -1^{1/2}$ represents the imaginary constant. Furthermore, the parameters Y_0 or Admittance (Ω^{-1} cm^2 s^n) and n ($-1 \leq n \geq 1$) are independent of frequency. In general, the pure inductive, resistance and capacitive behaviors (RC) are attributed to the CPE with n value of −1, 0 and 1, respectively. As can be seen from Table 5.4, the TFSOC has the highest R_{ct} of 3.3×10^3 Ω cm^2 compared to the RS (179.15 Ω cm^2) after 1 h immersion in the SCS. Over time, this value gradually decreased to 2.7×10^3 Ω cm^2 (after 720 h), which caused a decrease in load transfer resistance.

Table 5.4. EIS fitting parameters of annealed RS at 500 °C and TFSOC at 700 °C after immersion in SCS.

Sample Name	***RS-500°C***	***TiSiNb$_{0.02}$-700 °C***			
Immersion Time	*1 h*	*1 h*	*24 h*	*360 h*	*720 h*
R_s (Ω cm^2)	19.5	16.4	18.1	18.3	18.9
Y_0 (Ω^{-1} cm^2 s^n)	2.9×10^{-4}	2.4×10^{-3}	6.9×10^{-3}	6.5×10^{-4}	1.5×10^{-3}
n	0.9	0.6	0.6	0.8	0.7
R_{ct} (Ω cm^2)	179.1	3.3×10^3	2.8×10^3	2.5×10^3	2.7×10^3

Formation of the high protective TFSOC with titanium oxide phase and its enhancement by iron oxide (cf. EDS and XRD) as well as the formation of the protective passive film (cf. PEP analyses) have resulted in the good constant resistance over the long immersion time. Decreasing the Y_0 to 6.9×10^{-3} (Ω^{-1} cm^2 s^n) after 24 h immersion indicates that a small area on the TFSOC surface has participated in the corrosion process. Furthermore, according to the n values (between 0 and 1) as shown in Table 5.4, it can be concluded that the behavior of the CPE is a RC-type [343]. Hence, it can be assumed that owing to the thickening of the passive layers the R_{ct} value has not changed with increasing immersion time. Figure 5.9a,b show Bode plots and Bode phase diagrams of TFSOC at different immersion times in SCS, respectively. As shown in Bode plots of TFSOC three different regions as high ($\geq 10^3$ Hz), medium ($0.1–10^3$ Hz) and low ($<10^3$ Hz) frequencies indicate the R_s properties, RC-type behavior and R_{ct} process at the SCS/electrode interface, respectively. As can be seen, despite long immersion time, the

impedance parameters of the TFSOC were not significantly changed except that phase angle tended to decrease at low frequency. This slight decrease is due to the formation of pores/cracks in TFSOC surfaces (cf. Figure 5.4) which allows the occurrence of the localized corrosion in the SCS harsh environment. Nonetheless, as concluded by the EIS and PEP results, the SCS electrolyte cannot be used to diffuse and attack the substrate from these corrosion points. According to the passivation mechanism (cf. PEP studies), the passive layer of TFSOC generated by the corrosion products offered an extra protective barrier to the substrate, thereby hinder and retard electrolyte diffusion. It can be inferred that the TFSOC shows capacitive behavior with a significant phase angle between low/mid-frequency regions which can be correlated with thin-film insulation and compactness. Therefore, it can be concluded that the Nyquist plots from the EIS analyses were largely compatible with the PEP result and TFSOC can effectively protect the RS with little degradation of cathode working potential.

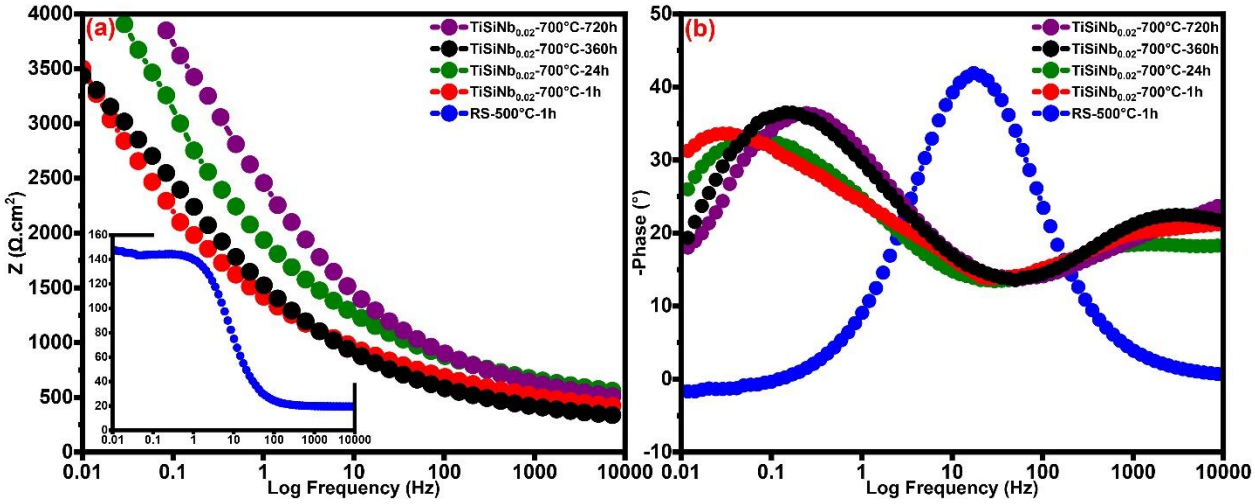

Figure 5.9. Bode plots (**a**) and Bode phase diagrams (**b**) for RS and TFSOC for different immersion time in SCS.

5.3.6. Computation and Evaluation of Conductivity and Activation Energy

Figure 5.10 illustrates the Arrhenius representation of $Ti_{0.50-y/2}Si_{0.50-y/2}Nb_{y1,2}O_2$ with two different Nb contents. It can be seen that for both samples the activation energy is around 0.20 eV. However, it appears that the concentration of Nb acts inversely on the TFSOC resistivity. If Nb as donor dopant would be compensated completely electronically, an increase of conductivity would be expected. From the decrease of conductivity with higher Nb content, it can be concluded that Nb at the higher content level is partially compensated by the formation of cation vacancies ($V_{Ti}^{\prime\prime\prime\prime}$). The activation energy of the conductivity gives evidence that the electrons generated by donor doping are trapped by either the formation of Ti^{3+} ions (in Kröger–Vink-notation $Ti_{Ti}^{\prime}$) or the association with oxygen vacancies. Since the number of oxygen vacancies in doped donor oxides should be very low, the first assumption seems more plausible. These trapped electrons are released either by hopping (polaronic motion) to neighbouring Ti^{4+} ions or by excitation to the conduction band. Unfortunately, the activation energy found in the literature for such Ti^{3+}/Ti^{4+} hopping differs by one order of magnitude. Shan Yang et al. [371] estimated the activation energy for the intrinsic electron small polaron in rutile Ti oxide from electron paramagnetic resonance measurements as 0.024 eV, which would mean that these defects are thermally unstable at very low temperatures and would be fully ionized at ambient conditions. Di Valentin et al. [372], however, calculated the activation energy for the excitation of an electron from a six-fold-coordinated Ti_{6c}^{3+} ion as 0.3 eV. One may take into account that the activation energy for polaron motion in a solid solution of Ti and Si oxides is increased because of the local distortion of the lattice due to the difference in the ionic radii and therefore is well above the suggested 0.024 eV of pure Ti oxide.

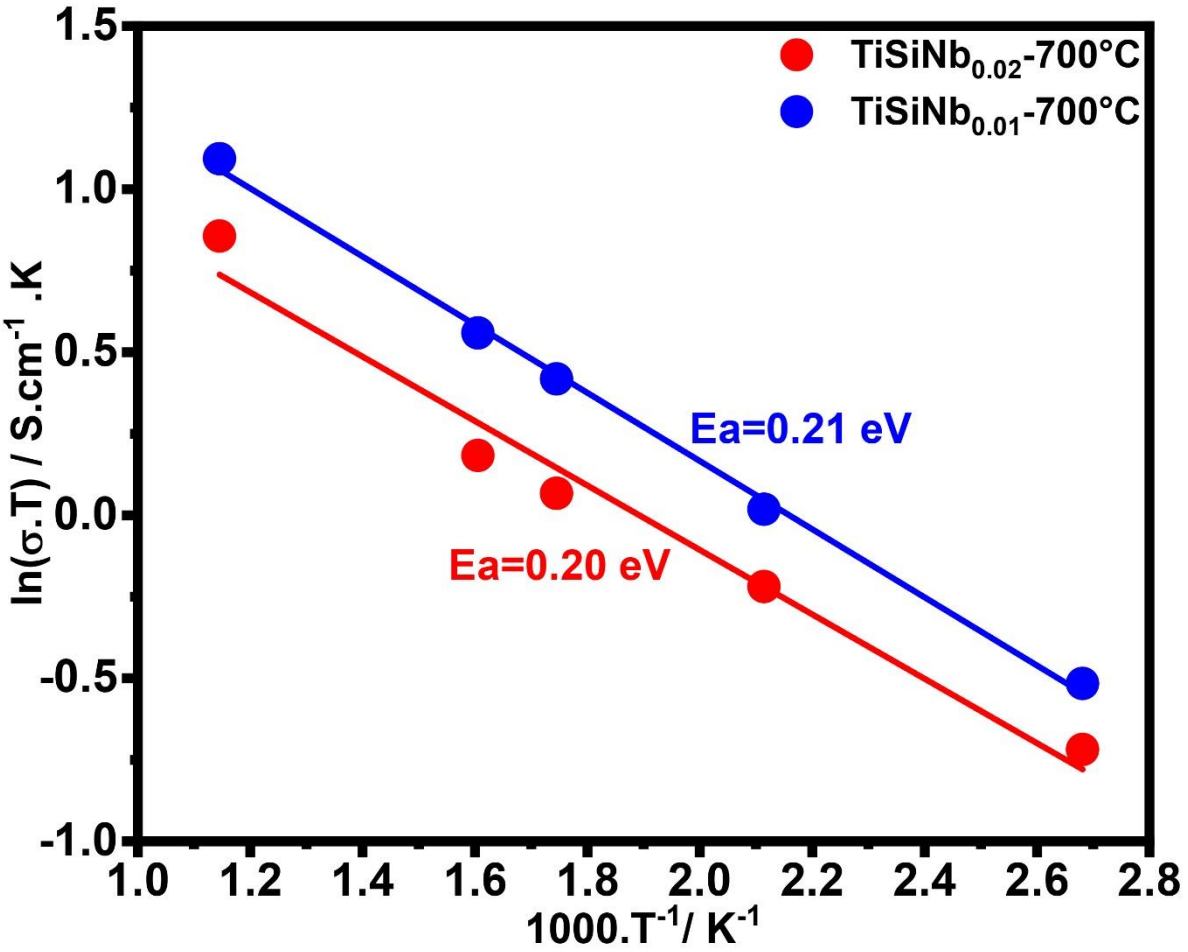

Figure 5.10. Arrhenius-plot of TiSNb with different Nb content annealed at 700 °C in N_2 atmosphere.

5.4. Conclusion

The TiSiNb TFSOC has been developed to improve the conductivity and electrochemical degradation resistance of C45E used as metal interconnects in PEMFC applications. Most parameters such as thermal stability, OH groups, phases and crystallite sizes can be controlled by the sol-gel method and annealing temperature. The SEM analysis shows the presence of a compact and homogeneous TFSOC mixed with iron oxide as evidenced by EDS and XRD analyses. The use of an N_2 atmosphere and high annealing temperature leads to an increase in the self-protective and long-term stability of the TFSOC. To define their anti-corrosion efficiency, the highest long-term anti-corrosion activity after 720 h (1.33 kΩ cm^2) immersion in SCS using the PEP has been obtained in comparison to RS. EIS data also further confirmed that the cheap C45E steel coated can play a significant function in improving the interconnect resistance. Due to the low activation energy, the material composition and heat treatment conditions could be optimized further to improve the conductivity. Owing to its homogeneity and high corrosion resistance in the PEMFC environment and cost-effective materials and method, the coated moderate C45E carbon steel can be considered as a cheap effective combination for interconnect in the future PEMFC technologies, which is effective for considerably increasing the PEMFC output power.

Acknowledgments: The authors are thankful to Viktor Hacker from Institute of Chemical Engineering and Environmental Technology for valuable discussion of PEMFC. Authors are thankful to Daniel Rettenwander and Qamar Abbas for their help in determination of conductivity and advisory support, respectively.

Chapter 6

Summary and Future Prospects

6.1. Summary

Proton exchange membrane fuel cells (PEMFC) with a massive reduction of pollution are sustainable, low-cost and environmentally friendly alternative energy sources that can be the best supplement or replace fossil fuels. However, PEMFC is too expensive and exhibited poor durability and stability compared to conventional power sources. Replacement of conventional materials such as graphite and polymer with different types of metallic interconnects has been widely considered as a promising alternative route to achieving a reduction in the cost of PEMFC. Metals are, however, not satisfactory in electrochemical degradation resistance in the PEMFC harsh environment and exhibit unacceptable interfacial contact resistance with the gas diffusion layer resulting in unacceptable fuel cell performance. Hence, metals require cost-effective surface modification to be viable materials for interconnectors with long term stability in PEMFC applications.

The work presented in this thesis explored the electrochemical degradation resistance and electrical conductivity of adhesive Titania-based thin film solid oxide coating (TFSOC) on cost-effective C45E steel and their long-term stabilities of corrosion behavior and interfacial contact resistance (ICR) in the simulated PEMFC working environments. Since the different protective coatings reported in the literature experience significant TFSOC during the long-term degradation resistance, the surface nitriding modification is used on conductive TFSOC to improve its effectiveness. Firstly, TiO_2-SiO_2 multi-layers coating was prepared by a facile and green sol-gel process on C45E through a dip-coating technique. It is demonstrated that the sol-gel technique as a straightforward and successful technique compared with other synthesis techniques allows the preparation of different TFSOC on metal substrates. To produce a low cost-high performance coating with the highest resistance of the metal to electrochemical degradation, a different number of coating layers in different annealing temperatures and atmospheres have been prepared. Layers of protective TiO_2-SiO_2 forms on the surface of the substrate and thus inhibits further corrosion of the underneath coating and subsequently limits

the coating degradation during the PEP test. TiO_2-SiO_2 combines the high electrochemical degradation resistance of TiO_2 and excellent wear resistance of SiO_2 to best utilize the individual merit of a two-component-system as a coating on the substrate. The annealing temperatures and atmosphere as significant parameters play a crucial role in layer properties in tuning the electrochemical degradation resistance of protective coatings. The results of the PEP tests indicated a significant improvement in degradation resistance in all coated RS as affordable Interconnects in PEMFC application. Compared with the argon atmosphere, TiO_2-SiO_2 annealed in the air atmosphere exhibits a significantly enhanced degradation resistance and thus a little increase in ICR after the PEP and EIS tests. The results have also shown that degradation resistance is enhanced due to the formation of convoluted multi-layer iron-titanium oxide.

Furthermore, to balance the electrochemical degradation resistance and electrical conductivity of the TFSOC, multilayer TiSiNb coatings with different Nb content were prepared on C45E steel as cost-effective and easily formable interconnects in PEMFC applications using the sol-gel technique in a nitrogen atmosphere. The use of nitrogen as an excellent element for chemical doping results in the formation of a dense, thick and adhesive oxide layer composite (TiSiNb), which decreases the electrochemical degradation of the underneath substrate and the coating oxidation during the long period of immersion in harsh environment and subsequently limits the total thickness increase of the oxide layers. A thirty-day exposure experiment indicates that the Nb leads to better electrical conductivity, excellent electrochemical stability and higher electrochemically active surface, which may be due to that the doping of Nb ions reduces the micro-poles. The above two studies demonstrate that nitrogen, argon and oxygen atmosphere can be useful as a surface modification treatment to incorporate different elements and atoms or to implement TFSOC as a feasible strategy to improve the electrochemical degradation resistance while maintaining considerable electrical conductivity at the same time. Proposed mechanisms point to an efficient direction to prepare the electrically conductive

TFSOC with high degradation resistance in PEMFC harsh environment. Additionally, considering the fact that metal interconnects experience long-term cycling in PEMFC harsh conditions, TiSiNb coatings, the formation of the iron oxides on the surface and passive film have significantly improved the degradation resistance. The quite low electrochemical degradation current and the mitigated morphological degradation due to the excellent structural properties and formation of a conductive self-passivating film of the coated specimens confirm that the TiSiNb TFSOC can effectively restrain the anodic dissolution caused by the harsh operating PEMFC environment. Analysis of the Energy-dispersive X-ray spectroscopy (EDS) of the oxide layer suggests that a protective coating mixed with iron oxide substrate due to the more O binding based on original-OH contributes to the improved degradation resistance of metal-based interconnects. Eventually, the enriched N_2 in the metal at the substrate/TFSOC interface may reduce the anodic dissolution rate and thus increase the resistance to electrochemical degradation by decreasing the current of corrosion. Lastly, the passive formed film progressively changes toward that of the conductive metal with the loss of hydrogen ions without the change in thickness due to the presence of N_2 and Nb elements, as a result, the degradation resistance can be constant over a long time in the presence of the passive film and constant value of corrosion potential in PEMFC environment.

In conclusion, the results of this study suggest that 1) both annealing temperature and atmosphere have a significant impact on corrosion current density and passive current density, 2) argon and air have a more negative obvious impact on the electrical conductivity of TFSOC than nitrogen, 3) a high synergistic effect between N_2 and annealing temperature and TFSOC on the current densities are observed at the intermediate open circuit potential and polarization resistance range because the N_2 can be effected on the metal ions of passivation film when it is present in SCS after low annealing temperature.

6.2. Future Prospects

Several suggestions are listed as follows as a reference for the researchers who will further work on the electrochemical degradation resistance TFSOC with acceptable electrically conductive on metal-base interconnects in PEMFC applications to satisfy the target values set by the United States Department of Energy (DOE) in the near future.

1) Usage of cost-effective metals with high resistance to electrochemical degradation.

Weak electrochemical properties including degradation and rust resistance due to lack of chromium, make common metal-based interconnects inapt to operate under harsh conditions of the PEMFC environment. Therefore, it is of vital interest to assess the potential of conductive TFSOC deposited on new steel with low cost, high strength, ease of machining and shaping into thin sheets that contain chromium element to establish inexpensive alternative interconnects in PEMFC to satisfy the target values set by the DOE target. As a result, the objective of new researches in the future can be focused on implementation and development of the low-cost and new generation of low alloyed steels such as T23 and T24 and austenitic-ferritic duplex stainless steel such as S32101 and links to their electrical and electrochemical properties under conditions typical for PEMFCs.

2) Controllable oxidation of semi-conductive TFSOC.

Several Titania-based coatings have been extended in the recent time for electrochemical degradation-resistant and electrically conductive protective coating on metal-based interconnects for use in a harsh PEMFC environment. However, the Titania-based coating prepared by traditional techniques such as sol-gel dip-coating still tends to suffer electrochemical degradation in the long-term under the severe acidic conditions of PEMFC and results in the fast surface attack and increase of ICR over time. A TFSOC with the structural integrity as hard coatings with improved electrochemical degradation resistance but without compromising its electronic or even ionic conductivity is an ideal solution for metal-based interconnects in PEMFC applications. In this case, conductive elements especially Zirconium,

Lithium, Indium and Tantalum are the potential candidates for sacrificial protection. The challenge here is to accurately control the oxidation of the elements with different annealing atmosphere as a surface modification or control the content of oxygen and conductively-doped atoms introduced to the mentioned conductive elements.

3) Balancing the ICR and degradation resistance.

Over a long period of operating under real PEMFC conditions, the ICR of TFSOC increases, which can result in suffering electrochemical degradation on the surface of TFSOC and consequently decrease the PEMFC output power. Therefore, it is very meaningful to adjust the increase of ICR through balancing with the electrochemical degradation resistance of protective TFSOC. Despite extensive research is focusing on the preparation of high electrochemical degradation resistance coatings with acceptable conductivity, however, limited work has been considered to control or prepare low-ICR coatings or surfaces of coated interconnectors under the long-term operation of the PEMFC stack in the harsh acidic environment. It is, therefore, necessary to develop oxide-based coatings with high degradation resistance that can provide good electronic or ionic conductivity during the PEMFC stack service in a long-period to keep ICR low.

4) Dynamic loading induced degradation of the metal interconnector.

Operating PEMFC stack experiences dynamic loading/output and the consequence of potential changes. Since metal interconnects are electronically connected with the electrodes, they will suffer degradation induced by dynamic potential changes. Previous work in literature used the PEP test at the normal work potential (0.6 V vs. Ag/AgCl) to simulate the potential at constant loading or energy output. Unfortunately, this is a less adequate simulation for the practical situation, especially for the PEMFC stack. Therefore, the electrochemical degradation behavior of PEMFC metal interconnector under dynamic potential changes in the simulated environment of PEMFC is worth studying.

References

[1] Koçak B, Fernandez AI, Paksoy H. Review on sensible thermal energy storage for industrial solar applications and sustainability aspects. Sol Energy 2020;209:135–69. https://doi.org/10.1016/j.solener.2020.08.081

[2] Menberg K, Heberle F, Bott C, Brüggemann D, Bayer P. Environmental performance of a geothermal power plant using a hydrothermal resource in the Southern German Molasse Basin. Renew Energy 2020. https://doi.org/10.1016/j.renene.2020.11.028

[3] Malek ABMA, Hasanuzzaman M, Abd Rahim N. Prospects, progress, challenges and policies for clean power generation from biomass resources. Clean Technol Environ Policy 2020:1–25. https://doi.org/10.1007/s10098-020-01873-4

[4] Ogungbemi E, Wilberforce T, Ijaodola O, Thompson J, Olabi AG. Selection of proton exchange membrane fuel cell for transportation. Int J Hydrogen Energy 2020. https://doi.org/10.1016/j.ijhydene.2020.06.147

[5] Dawood F, Anda M, Shafiullah GM. Hydrogen production for energy: An overview. Int J Hydrogen Energy 2020;45:3847–69. https://doi.org/10.1016/j.ijhydene.2019.12.059

[6] Valente A, Iribarren D, Candelaresi D, Spazzafumo G, Dufour J. Using harmonised life-cycle indicators to explore the role of hydrogen in the environmental performance of fuel cell electric vehicles. Int J Hydrogen Energy 2020;45:25758–65. https://doi.org/10.1016/j.ijhydene.2019.09.059

[7] Karanfil G. Importance and applications of DOE/optimization methods in PEM fuel cells: A review. Int J Energy Res 2020;44:4–25. https://doi.org/10.1002/er.4815

[8] Carcadea E, Varlam M, Ismail M, Ingham DB, Marinoiu A, Raceanu M, et al. PEM fuel cell performance improvement through numerical optimization of the parameters of the porous layers. Int J Hydrogen Energy 2020;45:7968–80. https://doi.org/10.1016/j.ijhydene.2019.08.219

[9] Usai L, Hung CR, Vásquez F, Windsheimer M, Burheim OS, Strømman AH. Life cycle assessment of fuel cell systems for light duty vehicles, current state-of-the-art and future impacts. J Clean Prod 2020:125086. https://doi.org/10.1016/j.jclepro.2020.125086

[10] Stančin H, Mikulčić H, Wang X, Duić N. A review on alternative fuels in future energy system. Renew Sustain Energy Rev 2020;128:109927. https://doi.org/10.1016/j.rser.2020.109927

[11] Martínez S FH, Ariza HM. Low cost, high performance fuel cell energy conditioning system controlled by neural network. Telkomnika 2020;18. https://doi.org/10.12928/telkomnika.v18i6.16426

[12] Dong P, Xie G, Ni M. The mass transfer characteristics and energy improvement with various partially blocked flow channels in a PEM fuel cell. Energy 2020;206:117977. https://doi.org/10.1016/j.energy.2020.117977

[13] Xu Z, Qiu D, Yi P, Peng L, Lai X. Towards mass applications: A review on the challenges and developments in metallic bipolar plates for PEMFC. Prog Nat Sci Mater Int 2020. https://doi.org/10.1016/j.pnsc.2020.10.015

[14] Dickinson EJF, Smith G. Modelling the Proton-Conductive Membrane in Practical Polymer Electrolyte Membrane Fuel Cell (PEMFC) Simulation: A Review. Membranes (Basel) 2020;10:310. https://doi.org/10.3390/membranes10110310

[15] Haider R, Wen Y, Ma Z-F, Wilkinson DP, Zhang L, Yuan X, et al. High temperature proton exchange membrane fuel cells: progress in advanced materials and key technologies. Chem Soc Rev 2020. https://doi.org/10.1039/D0CS00296H

[16] Porstmann S, Wannemacher T, Drossel W-G. A comprehensive comparison of state-of-the-art manufacturing methods for fuel cell bipolar plates including anticipated future industry trends. J Manuf Process 2020;60:366–83. https://doi.org/10.1016/j.jmapro.2020.10.041

[17] Li DG, Chen DR, Liang P. Influences of plastic strain and strain rate on corrosion behavior of 316L stainless steel in simulated cathodic environment of proton exchange membrane fuel cell. Int J Hydrogen Energy 2020. https://doi.org/10.1016/j.ijhydene.2020.11.177

[18] Wang X-Z, Fan H-Q, Muneshwar T, Cadien K, Luo J-L. Balancing the corrosion resistance and through-plane electrical conductivity of Cr coating via oxygen plasma treatment. J Mater Sci Technol 2020;61:75–84. https://doi.org/10.1016/j.jmst.2020.06.012

[19] Li Y, Wang H, Priest C, Li S, Xu P, Wu G. Advanced Electrocatalysis for Energy and Environmental Sustainability via Water and Nitrogen Reactions. Adv Mater 2020:2000381. https://doi.org/10.1002/adma.202000381

[20] Açıkkalp E, Ahmadi MH. Performance evaluation of PEM fuel cell-chemical heat pump-absorption refrigerator hybrid system. Int J Ambient Energy 2020:1–9. https://doi.org/10.1080/01430750.2020.1712238

[21] Li Y, Zheng Z, Chen X, Liu Y, Liu M, Li J, et al. Carbon corrosion behaviors and the mechanical properties of proton exchange membrane fuel cell cathode catalyst layer. Int J Hydrogen Energy 2020;45:23519–25. https://doi.org/10.1016/j.ijhydene.2020.06.170

[22] Liu Z, Lian X, Liu T, Yang Y, Zhu J, Dong H. Effects of rare earth elements on corrosion behaviors of low-carbon steels and weathering steels. Mater Corros 2020;71:258–66. https://doi.org/10.1002/maco.201911150

[23] Alaefour I, Shahgaldi S, Zhao J, Li X. Synthesis and Ex-Situ characterizations of diamond-like carbon coatings for metallic bipolar plates in PEM fuel cells. Int J Hydrogen Energy 2020. https://doi.org/10.1016/j.ijhydene.2020.09.259

[24] Kahyarian A, Brown B, Nešić S. The unified mechanism of corrosion in aqueous weak acids solutions: a review of the recent developments in mechanistic understandings of mild steel corrosion in the presence of carboxylic acids, carbon dioxide, and hydrogen sulfide. Corrosion 2020;76:268–78. https://doi.org/10.5006/3474

[25] Jain P, Patidar B, Bhawsar J. Potential of nanoparticles as a corrosion inhibitor: a review. J Bio-and Tribo-Corrosion 2020;6:1–12. https://doi.org/10.1007/s40735-020-00335-0

[26] Deyab MA. Anticorrosion properties of nanocomposites coatings: A critical review. J Mol Liq 2020:113533. https://doi.org/10.1016/j.molliq.2020.113533

[27] Ettefagh AH, Guo S, Raush J. Corrosion performance of additively manufactured stainless steel parts: A review. Addit Manuf 2020:101689. https://doi.org/10.1016/j.addma.2020.101689

[28] Daniyal M, Akhtar S. Corrosion assessment and control techniques for reinforced concrete structures: a review. J Build Pathol Rehabil 2020;5:1. https://doi.org/10.1007/s41024-019-0067-3

[29] Parvasi P, Mohammad Jokar S, Basile A, Iulianelli A. An on-board pure H_2 supply system based on a membrane reactor for a fuel cell vehicle: A theoretical study. Membranes (Basel) 2020;10:159. https://doi.org/10.3390/membranes10070159

[30] Liu S, Chen T, Zhang C, Xie Y. Study on the performance of proton exchange membrane fuel cell (PEMFC) with dead-ended anode in gravity environment. Appl Energy 2020;261:114454. https://doi.org/10.1016/j.apenergy.2019.114454

[31] Chapman A, Itaoka K, Farabi-Asl H, Fujii Y, Nakahara M. Societal penetration of hydrogen into the future energy system: Impacts of policy, technology and carbon targets. Int J Hydrogen Energy 2020;45:3883–98. https://doi.org/10.1016/j.ijhydene.2019.12.112

[32] Shanbhag S, Joshi G. Parametric review on Fuel Cells and their Applications. IOP Conf. Ser. Mater. Sci. Eng., vol. 810, IOP Publishing; 2020, p. 12065. https://doi.org/10.1088/1757-899X/810/1/012065

[33] Chaubey N, Qurashi A, Chauhan DS, Quraishi MA. Frontiers and advances in green and sustainable inhibitors for corrosion applications: A critical review. J Mol Liq 2020:114385. https://doi.org/10.1016/j.molliq.2020.114385

[34] Hossain N, Asaduzzaman Chowdhury M, Kchaou M. An overview of green corrosion inhibitors for sustainable and environment friendly industrial development. J Adhes Sci Technol 2020:1–18. https://doi.org/10.1080/01694243.2020.1816793

[35] Rodrigues R, Gaboreau S, Gance J, Ignatiadis I, Betelu S. Reinforced concrete structures: A review of corrosion mechanisms and advances in electrical methods for corrosion monitoring. Constr Build Mater 2020:121240. https://doi.org/10.1016/j.conbuildmat.2020.121240

[36] Sharma S, Kumar A. Recent advances in metallic corrosion inhibition: A review. J Mol Liq 2020:114862. https://doi.org/10.1016/j.molliq.2020.114862

[37] Maier HJ, Julmi S, Behrens S, Klose C, Gartzke A-K, Wriggers P, et al. Magnesium Alloys for Open-Pored Bioresorbable Implants. JOM 2020:1–11. https://doi.org/10.1007/s11837-020-04078-8

[38] Guan Z, Linsley CS, Hwang I, Yao G, Wu BM, Li X. Novel zinc/tungsten carbide nanocomposite as bioabsorbable implant. Mater Lett 2020;263:127282. https://doi.org/10.1016/j.matlet.2019.127282

[39] Khan MM, Deen KM, Shabib I, Asselin E, Haider W. Controlling the dissolution of Iron through the development of nanostructured Fe-Mg for biomedical applications. Acta Biomater 2020. https://doi.org/10.1016/j.actbio.2020.06.014

[40] Zhao T, Zhang J, Teng L, Yang Y. High-Temperature Oxidation Performance of Niobium-Containing Ferritic Stainless Steel for Exhaust Manifold. Trans Indian Inst Met n.d.:1–12. https://doi.org/10.1007/s12666-020-02139-9

[41] Meisner KJ, Opila EJ. Hot Corrosion of Shipboard Gas Turbine Blades. Oxid Met 2020:1–22. https://doi.org/10.1007/s11085-020-09990-7

[42] Obot IB, Onyeachu IB, Umoren SA, Quraishi MA, Sorour AA, Chen T, et al. High temperature sweet corrosion and inhibition in the oil and gas industry: Progress, challenges and future perspectives. J Pet Sci Eng 2020;185:106469. https://doi.org/10.1016/j.petrol.2019.106469

[43] Rahimi-Esbo M, Rahgoshay SM, Hassani MM, Firouzjaei KD. Novel design and numerical evaluating of a cooling flow field in PEMFC with metallic bipolar plates. Int J Hydrogen Energy 2020. https://doi.org/10.1016/j.ijhydene.2020.07.066

[44] Sadhasivam T, Ajeya K V, Kim YA, Jung H-Y. An experimental investigation of the feasibility of Pb based bipolar plate material for unitized regenerative fuel cells system. Int J Hydrogen Energy 2020. https://doi.org/10.1016/j.ijhydene.2020.03.023

[45] Jadi S Ben, El Jaouhari A, Aouzal Z, El Guerraf A, Bouabdallaoui M, Wang R, et al. Electropolymerization and corrosion resistance of polypyrrole on nickel bipolar plate for PEM fuel cell application. Mater Today Proc 2020;22:52–6. https://doi.org/10.1016/j.matpr.2019.08.072

[46] Xu M, Kang S, Lu J, Yan X, Chen T, Wang Z. Properties of a Plasma-Nitrided Coating and a CrNx Coating on the Stainless Steel Bipolar Plate of PEMFC. Coatings 2020;10:183. https://doi.org/10.3390/coatings10020183

[47] Bai H. Mechanism analysis, anti-corrosion techniques and numerical modeling of corrosion in energy industry. Oil Gas Sci Technol d'IFP Energies Nouv 2020;75:42. https://doi.org/10.2516/ogst/2020031

[48] Abdeen DH, Atieh MA, Merzougui B. Corrosion Behaviour of 316L Stainless Steel in CNTs–Water Nanofluid: Effect of Temperature. Materials (Basel) 2021;14:119. https://doi.org/10.3390/ma14010119

[49] Khayatazad M, De Pue L, De Waele W. Detection Of Corrosion On Steel Structures Using Automated Image Processing. Dev Built Environ 2020:100022. https://doi.org/10.1016/j.dibe.2020.100022

[50] Latif J, Khan ZA, Stokes K. Structural monitoring system for proactive detection of corrosion and coating failure. Sensors Actuators A Phys 2020;301:111693. https://doi.org/10.1016/j.sna.2019.111693

[51] Seo M. Special issue on Recent advances in corrosion science: celebrating the 90th birthday of Professor Norio Sato. Corros Rev 2018;36:1–2. https://doi.org/10.1515/corrrev-2017-0125

[52] Loto CA, Loto RT, Popoola AP. Performance evaluation of zinc anodes for cathodic protection of mild steel corrosion in HCL. Chem Data Collect 2019;24:100280. https://doi.org/10.1016/j.cdc.2019.100280

[53] Fadl AM, Abdou MI, Laila D, Sadeek SA. Fabrication and characterization of novel p-Phenylamine-N (4-chloro salicylaldenemine) ligand and its metal complexes and evaluation their anti-corrosion and chemical resistance properties in epoxy/SiO_2 nanocomposite for steel surface coating. Chem Eng J 2020;384:123390. https://doi.org/10.1016/j.cej.2019.123390

[54] Chen Y, Lu X, Lamaka S V, Ju P, Blawert C, Zhang T, et al. Active protection of Mg alloy by composite PEO coating loaded with corrosion inhibitors. Appl Surf Sci 2020;504:144462. https://doi.org/10.1016/j.apsusc.2019.144462

[55] Vallimanalan A, Babu SPK, Muthukumaran S, Murali M, Gaurav V, Mahendran R. Corrosion behaviour of thermally sprayed Mo added AlCoCrNi high entropy alloy coating. Mater Today Proc 2020;27:2398–400. https://doi.org/10.1016/j.matpr.2019.09.149

[56] Chen Z, Zhang G, Yang W, Xu B, Chen Y, Yin X, et al. Superior conducting polypyrrole anti-corrosion coating containing functionalized carbon powders for 304 stainless steel bipolar plates in proton exchange membrane fuel cells. Chem Eng J 2020:124675. https://doi.org/10.1016/j.cej.2020.124675

[57] Chalhoub C, François R, Carcasses M. Effect of Cathode–Anode distance and electrical resistivity on macrocell corrosion currents and cathodic response in cases of chloride induced corrosion in reinforced concrete structures. Constr Build Mater 2020;245:118337. https://doi.org/10.1016/j.conbuildmat.2020.118337

[58] Miyamoto H, Yoshimura K, Mimaki T, Yamashita M. Behavior of intergranular corrosion of <011> tilt grain boundaries of pure copper bicrystals. Corros Sci 2002;44:1835–46. https://doi.org/10.1016/S0010-938X(01)00158-5

[59] Li YZ, Wang X, Zhang GA. Corrosion behaviour of 13Cr stainless steel under stress and crevice in 3.5 wt.% NaCl solution. Corros Sci 2020;163:108290. https://doi.org/10.1016/j.corsci.2019.108290

[60] Tamura H. The role of rusts in corrosion and corrosion protection of iron and steel. Corros Sci 2008;50:1872–83. https://doi.org/10.1016/j.corsci.2008.03.008

[61] Mundhenk N, Carrero S, Knauss KG, Wonneberger R, Undisz A, Wu Y. Kinetic and thermodynamic analysis of high-temperature CO_2 corrosion of carbon steel in simulated geothermal NaCl fluids. Corros Sci 2020:108597. https://doi.org/10.1016/j.corsci.2020.108597

[62] Bao H, Xu G, Wang Q, Peng Y, Liu J. Study on the deterioration mechanism of cement-based materials in acid water containing aggressive carbon dioxide. Constr Build Mater 2020;243:118233. https://doi.org/10.1016/j.conbuildmat.2020.118233

[63] Okewale AO, Adebayo T. Investigation of pumpkin pod extract as corrosion inhibitor for carbon steel in HCl Solution. Niger J Technol 2020;39:173–81. https://doi.org/10.4314/njt.v39i1.19

[64] Eid J, Takenouti H, Saadi BA, Taibi S. Electrochemical studies of steel rebar corrosion in clay: Application to a raw earth concrete. Corros Sci 2020:108556. https://doi.org/10.1016/j.corsci.2020.108556

[65] Bancroft WD. Electrolytic Theory of Corrosion. J Phys Chem 2002;28:785–871. https://doi.org/10.1021/j150242a001

[66] Luo S, Guo H, Wang Z, Li X, Wang J, Yan G. The electrochemical performance and reaction mechanism of coated titanium anodes for manganese electrowinning. J Electrochem Soc 2019;166:E502. https://doi.org/10.1149/2.1071914jes

[67] Kasian O, Geiger S, Li T, Grote J-P, Schweinar K, Zhang S, et al. Degradation of iridium oxides via oxygen evolution from the lattice: correlating atomic scale structure with reaction mechanisms. Energy Environ Sci 2019;12:3548–55. https://doi.org/10.1039/C9EE01872G

[68] Zhang S, Lu Q, Xu Y, He K, Liang K, Tan Y. Corrosion Behaviour of 316L Stainless Steel in Boric Acid Solutions. Int J Electrochem Sci 2018;13:3246–56. https://doi.org/10.20964/2018.04.33

[69] Zhu M, Zhang Q, Yuan YF, Guo SY, Chen YB. Study on the Microstructure and Alternating Current Corrosion Behavior of SAF2507 Super-Duplex Stainless Steel in 3.5% NaCl Solution. J Mater Eng Perform 2020;29:1366–74. https://doi.org/10.1007/s11665-020-04624-0

[70] Wei H, Chen Y, Yu W, Su L, Wang X, Tang D. Study on corrosion resistance of high-strength medium-carbon spring steel and its hydrogen-induced delayed fracture. Constr Build Mater 2020;239:117815. https://doi.org/10.1016/j.conbuildmat.2019.117815

[71] Permeh S, Lau K, Tansel B, Duncan M. Surface conditions for microcosm development and proliferation of SRB on steel with cathodic corrosion protection. Constr Build Mater 2020;243:118209. https://doi.org/10.1016/j.conbuildmat.2020.118209

[72] Fu X, Ji Y, Cheng X, Dong C, Fan Y, Li X. Effect of grain size and its uniformity on corrosion resistance of rolled 316L stainless steel by EBSD and TEM. Mater Today Commun 2020:101429. https://doi.org/10.1016/j.mtcomm.2020.101429

[73] Lipińska M, Bazarnik P, Lewandowska M. The influence of severe plastic deformation processes on electrical conductivity of commercially pure aluminium and 5483 aluminium alloy. Arch Civ Mech Eng 2016;16:717–23. https://doi.org/10.1016/j.acme.2016.04.013

[74] Ralston KD, Birbilis N. Effect of grain size on corrosion: a review. Corrosion 2010;66:75005. https://doi.org/10.5006/1.3462912

[75] Olugbade T. Datasets on the corrosion behaviour of nanostructured AISI 316 stainless steel treated by SMAT. Data Br 2019;25:104033. https://doi.org/10.1016/j.dib.2019.104033

[76] Tang Z, Jiang F, Long M, Jiang J, Liu H, Tong M. Effect of annealing temperature on microstructure, mechanical properties and corrosion behavior of Al-Mg-Mn-Sc-Zr alloy. Appl Surf Sci 2020:146081. https://doi.org/10.1016/j.apsusc.2020.146081

[77] Robertson J. The mechanism of high temperature aqueous corrosion of stainless steels. Corros Sci 1991;32:443–65. https://doi.org/10.1016/0010-938X(91)90125-9

[78] Shin H, Zhan R, Dhindsa KS, Pan L, Han T. Electrochemical Performance of Recycled Cathode Active Materials Using Froth Flotation-based Separation Process. J Electrochem Soc 2020;167:20504. https://doi.org/10.1149/1945-7111/ab6280

[79] Ryu S, Kwon YJ, Kim Y, Lee JU. Corrosion protection coating of three-dimensional metal structure by electrophoretic deposition of graphene oxide. Mater Chem Phys 2020:123039. https://doi.org/10.1016/j.matchemphys.2020.123039

[80] Hong S, Shi G, Zheng F, Liu M, Hou D, Dong B. Characterization of the corrosion profiles of reinforcement with different impressed current densities by X-ray micro-computed tomography. Cem Concr Compos 2020:103583. https://doi.org/10.1016/j.cemconcomp.2020.103583

[81] Hong S, Zheng F, Shi G, Li J, Luo X, Xing F, et al. Determination of impressed current efficiency during accelerated corrosion of reinforcement. Cem Concr Compos 2020;108:103536. https://doi.org/10.1016/j.cemconcomp.2020.103536

[82] Bower AF, Guduru PR, Sethuraman VA. A finite strain model of stress, diffusion, plastic flow, and electrochemical reactions in a lithium-ion half-cell. J Mech Phys Solids 2011;59:804–28. https://doi.org/10.1016/j.jmps.2011.01.003

[83] Vacchi GS, Silva R, Plaine AH, Suhuddin UFH, Alcântara NG, Sordi VL, et al. Refill friction stir spot welded AA5754-H22/Ti-6Al-4V joints: Microstructural characterization and electrochemical corrosion behavior of aluminum surfaces. Mater Today Commun 2020;22:100759. https://doi.org/10.1007/s11665-018-3694-y

[84] Pyun S-I. Strategies of metal corrosion protection. ChemTexts 2021;7:1–27. https://doi.org/10.1007/s40828-020-00121-y

[85] Kim S, Le T-H, Park CS, Park G, Kim KH, Kim S, et al. A solution-processable, nanostructured, and conductive graphene/polyaniline hybrid coating for metal-corrosion protection and monitoring. Sci Rep 2017;7:1–9. https://doi.org/10.1038/s41598-017-15552-w

[86] Hasanbeigi S, Tabaian SH, Yazdani S. Effect of Manufacturing Parameters on the Corrosion Behavior of AZ31 Coated by Mg–Al Layered Double Hydroxide. Met Mater Int 2020:1–14. https://doi.org/10.1007/s12540-020-00692-y

[87] Sah SP. Corrosion of 304 stainless steel in carbonates melt–a state of enhanced dissolution of corrosion products. Corros Sci 2020:108535. https://doi.org/10.1016/j.corsci.2020.108535

[88] Shrivastava V, Gupta GK, Singh IB. Heat treatment effect on the microstructure and corrosion behavior of Al-6061 alloy with influence of α-nanoalumina reinforcement in 3.5% NaCl solution. J Alloys Compd 2019;775:628–38. https://doi.org/10.1016/j.jallcom.2018.10.111

[89] Gao M, Zhang J, Liu Q, Li J, Zhang R, Chen G. Effect of the alkyl chain of quaternary ammonium cationic surfactants on corrosion inhibition in hydrochloric acid solution. Comptes Rendus Chim 2019;22:355–62. https://doi.org/10.1016/j.crci.2019.03.006

[90] Sabzi M, Dezfuli SM, Mirsaeedghazi SM. The effect of pulse-reverse electroplating bath temperature on the wear/corrosion response of Ni-Co/tungsten carbide nanocomposite coating during layer deposition. Ceram Int 2018;44:19492–504. https://doi.org/10.1016/j.ceramint.2018.07.189

[91] Ettefagh AH, Wen H, Chaichi A, Islam MI, Lu F, Gartia M, et al. Laser surface modifications of Fe-14Cr ferritic alloy for improved corrosion performance. Surf Coatings Technol 2020;381:125194. https://doi.org/10.1016/j.surfcoat.2019.125194

[92] Gong K, Wu M, Liu G. Comparative study on corrosion behaviour of rusted X100 steel in dry/wet cycle and immersion environments. Constr Build Mater 2020;235:117440. https://doi.org/10.1016/j.conbuildmat.2019.117440

[93] Hussain RR, Al-Negheimish A, Alhozaimy A, Singh DDN. Corrosion characteristics of vanadium micro-alloyed steel reinforcement bars exposed in concrete environments and industrially polluted atmosphere. Cem Concr Compos 2020:103728. https://doi.org/10.1016/j.cemconcomp.2020.103728

[94] Seddiqi H, Sadatshojaie A, Vaferi B, Yahyazadeh E, Salehi A, Wood DA. Mathematical model for iron corrosion that eliminates chemical potential parameters. Chinese J Chem Eng 2020;28:603–12. https://doi.org/10.1016/j.cjche.2019.09.007

[95] Andrade C. Initial steps of corrosion and oxide characteristics. Struct Concr 2020. https://doi.org/10.1002/suco.201900318

[96] Xu X, Liu S, Smith K, Cui Y, Wang Z. An overview on corrosion of iron and steel components in reclaimed water supply systems and the mechanisms involved. J Clean Prod 2020:124079. https://doi.org/10.1016/j.jclepro.2020.124079

[97] Baghdad M, Ait Saadi B. Electrochemical and characterisation study of corrosion of reinforcing steel embedded in kaolinite: two-year exposure study. Corros Eng Sci Technol 2020:1–15. https://doi.org/10.1080/1478422X.2020.1798677

[98] Xiao K, Li Z, Song J, Bai Z, Xue W, Wu J, et al. Effect of Concentrations of Fe^{2+} and Fe^{3+} on the Corrosion Behavior of Carbon Steel in Cl^- and $SO4^{2-}$ Aqueous Environments. Met Mater Int 2020:1–11. https://doi.org/10.1007/s12540-019-00590-y

[99] Xue J, Gao J, Shen Q, Li Q, Liu X, Jia H, et al. Performance of photocatalytic cathodic protection of 20 steel by α-Fe_2O_3/TiO_2 system. Surf Coatings Technol 2020;385:125445. https://doi.org/10.1016/j.surfcoat.2020.125445

[100] Bell C, Ritter EH, Wolford S. Oil Discoveries, Civil War, and Preventive State Repression. J Peace Res 2020.

[101] Mäkinen S, Mäkinen P. The Good, the Bad and the Ugly: Natural Gas, Oil and Coal. Atmos Clim Sci 2020;10:146–58. https://doi.org/10.4236/acs.2020.102007.

[102] Mostafa MM. Catastrophe Theory Predicts International Concern for Global Warming. J Quant Econ 2020:1–23. https://doi.org/10.1007/s40953-020-00199-8

[103] Ahmadi P, Torabi SH, Afsaneh H, Sadegheih Y, Ganjehsarabi H, Ashjaee M. The effects of driving patterns and PEM fuel cell degradation on the lifecycle assessment of hydrogen fuel cell vehicles. Int J Hydrogen Energy 2020;45:3595–608. https://doi.org/10.1016/j.ijhydene.2019.01.165

[104] Sorlei I-S, Bizon N, Thounthong P, Varlam M, Carcadea E, Culcer M, et al. Fuel Cell Electric Vehicles—A Brief Review of Current Topologies and Energy Management Strategies. Energies 2021;14:252. https://doi.org/10.3390/en14010252

[105] Zagal JH. Electrochemistry, past, present, and future: energy conversion, sensors, and beyond. J Solid State Electrochem 2020:1–3. https://doi.org/10.1007/s10008-020-04707-x

[106] Firouzjaei VK, Rahgoshay SM, Khorshidian M. Planar membrane humidifier for fuel cell application: Numerical and experimental case study. Int J Heat Mass Transf 2020;147:118872. https://doi.org/10.1016/j.ijheatmasstransfer.2019.118872

[107] Taner T. Energy and exergy analyze of PEM fuel cell: A case study of modeling and simulations. Energy 2018;143:284–94. https://doi.org/10.1016/j.energy.2017.10.102

[108] Bianco M, Poitel S, Hong J-E, Yang S, Wang Z-J, Willinger M, et al. Corrosion behaviour of nitrided ferritic stainless steels for use in solid oxide fuel cell devices. Corros Sci 2020;165:108414. https://doi.org/10.1016/j.corsci.2019.108414

[109] Inal OB, Deniz C. Assessment of fuel cell types for ships: Based on multi-criteria decision analysis. J Clean Prod 2020:121734. https://doi.org/10.1016/j.jclepro.2020.121734

[110] Arif M, Cheung SCP, Andrews J. A systematic approach for matching simulated and experimental polarization curves for a PEM fuel cell. Int J Hydrogen Energy 2020;45:2206–23. https://doi.org/10.1016/j.ijhydene.2019.11.057

[111] Al-Hamed KHM, Dincer I. A novel ammonia molten alkaline fuel cell based integrated powering system for clean rail transportation. Energy 2020:117620. https://doi.org/10.1016/j.energy.2020.117620

[112] Alias MS, Kamarudin SK, Zainoodin AM, Masdar MS. Active direct methanol fuel cell: An overview. Int J Hydrogen Energy 2020. https://doi.org/10.1016/j.ijhydene.2020.04.202

[113] Glenn MJ, Allen JA, Donne SW. Carbon electro-catalysis in the direct carbon fuel cell utilising alkali metal molten carbonates: A mechanistic review. J Power Sources 2020;453:227662. https://doi.org/10.1016/j.jpowsour.2019.227662

[114] Zhang J, Guo X, Guo Y, Zhang H, Hou S, Tian Y. Thermodynamic Analyses of a Phosphoric Acid Fuel Cell/Thermoelectric Generator Hybrid System with the Thomson Effect. Int J Electrochem Sci 2020;15:3068–88. https://doi.org/10.20964/2020.04.55

[115] Ren P, Pei P, Li Y, Wu Z, Chen D, Huang S. Degradation mechanisms of proton exchange membrane fuel cell under typical automotive operating conditions. Prog Energy Combust Sci 2020;80:100859. https://doi.org/10.1016/j.pecs.2020.100859

[116] Dwivedi S. Solid oxide fuel cell: Materials for anode, cathode and electrolyte. Int J Hydrogen Energy 2020. https://doi.org/10.1016/j.ijhydene.2019.11.234

[117] Steele BCH, Heinzel A. Materials for fuel-cell technologies. Mater. Sustain. Energy A Collect. Peer-Reviewed Res. Rev. Artic. from Nat. Publ. Gr., World Scientific; 2011, p. 224–31. https://doi.org/10.1142/9789814317665_0031

[118] Ramezanizadeh M, Nazari MA, Ahmadi MH, Chen L. A review on the approaches applied for cooling fuel cells. Int J Heat Mass Transf 2019;139:517–25. https://doi.org/10.1016/j.ijheatmasstransfer.2019.05.032

[119] Rivarolo M, Rattazzi D, Lamberti T, Magistri L. Clean energy production by PEM fuel cells on tourist ships: A time-dependent analysis. Int J Hydrogen Energy 2020. https://doi.org/10.1016/j.ijhydene.2019.12.086

[120] Cao Y, Li Y, Zhang G, Jermsittiparsert K, Nasseri M. An efficient terminal voltage control for PEMFC based on an improved version of whale optimization algorithm. Energy Reports 2020;6:530–42. https://doi.org/10.1016/j.egyr.2020.02.035

[121] Teixeira FC, de Sá AI, Teixeira APS, Ortiz-Martínez VM, Ortiz A, Ortiz I, et al. New modified Nafion-bisphosphonic acid composite membranes for enhanced proton conductivity and PEMFC performance. Int J Hydrogen Energy 2020. https://doi.org/10.1016/j.ijhydene.2020.01.212

[122] Kumar SS, Himabindu V. Hydrogen production by PEM water electrolysis–A review. Mater Sci Energy Technol 2019;2:442–54. https://doi.org/10.1016/j.mset.2019.03.002

[123] Huang B. Fuel Cell Research Based on Electrochemical Analysis. J Electron Res Appl 2020;4. https://doi.org/10.26689/jera.v4i3.1272

[124] Xu J, Zhang C, Fan R, Bao H, Wang Y, Huang S, et al. Modelling and control of vehicle integrated thermal management system of PEM fuel cell vehicle. Energy 2020:117495. https://doi.org/10.1016/j.energy.2020.117495

[125] Nanadegani FS, Lay EN, Sunden B. Computational analysis of the impact of a micro porous layer (MPL) on the characteristics of a high temperature PEMFC. Electrochim Acta 2020;333:135552. https://doi.org/10.1016/j.electacta.2019.135552

[126] Khorshidian M, Sedighi M. A review of the main mechanisms of catalyst layer degradation in polymer electrolyte membrane fuel cell (PEMFC) and different performance recovery methods. Iran J Hydrog Fuel Cell 2019;6:91–115. https://doi.org/10.22104/ijhfc.2019.3625.1190

[127] Borup RL, Kusoglu A, Neyerlin KC, Mukundan R, Ahluwalia RK, Cullen DA, et al. Recent developments in catalyst-related PEM fuel cell durability. Curr Opin Electrochem 2020;21:192–200. https://doi.org/10.1016/j.coelec.2020.02.007

[128] Talukdar K, Ripan MA, Jahnke T, Gazdzicki P, Morawietz T, Friedrich KA. Experimental and numerical study on catalyst layer of polymer electrolyte membrane fuel cell prepared with diverse drying methods. J Power Sources 2020;461:228169. https://doi.org/10.1016/j.jpowsour.2020.228169

[129] Witpathomwong S, Okhawilai M, Jubsilp C, Karagiannidis P, Rimdusit S. Highly filled graphite/graphene/carbon nanotube in polybenzoxazine composites for bipolar plate in PEMFC. Int J Hydrogen Energy 2020. https://doi.org/10.1016/j.ijhydene.2020.08.006

[130] Chakrasali RL. Operation and performance of grid connected proton exchange membrane fuel cell with ultra capacitor. Int J Dyn Control 2020;8:189–96. https://doi.org/10.1007/s40435-019-00535-8

[131] Zhang HK, Wang YF, Wang DH, Wang YL. Adaptive robust control of oxygen excess ratio for PEMFC system based on type-2 fuzzy logic system. Inf Sci (Ny) 2020;511:1–17. https://doi.org/10.1016/j.ins.2019.08.005

[132] Wu Z, Zhu P, Yao J, Tan P, Xu H, Chen B, et al. Thermo-economic modeling and analysis of an NG-fueled SOFC-WGS-TSA-PEMFC hybrid energy conversion system for stationary electricity power generation. Energy 2020;192:116613. https://doi.org/10.1016/j.energy.2019.116613

[133] Wang Y, Wu Q, Mei D, Wang Y. Development of highly efficient methanol steam reforming system for hydrogen production and supply for a low temperature proton exchange membrane fuel cell. Int J Hydrogen Energy 2020. https://doi.org/10.1016/j.ijhydene.2020.06.285

[134] Kannan V, Xue H, Raman KA, Chen J, Fisher A, Birgersson E. Quantifying operating uncertainties of a PEMFC–Monte Carlo-machine learning based approach. Renew Energy 2020. https://doi.org/10.1016/j.renene.2020.05.097

[135] Carton JG, Olabi A-G. Design of experiment study of the parameters that affect performance of three flow plate configurations of a proton exchange membrane fuel cell. Energy 2010;35:2796–806. https://doi.org/10.1016/j.energy.2010.02.044

[136] Singh R, Singh R, Lehana P. Effect of Fuel Concentration on Power Generation in Bio-Fuel Cell. J Sci Tech Adv 2016;2:13–6. https://doi.org/10.3384/ecp110571174

[137] Haji S. Analytical modeling of PEM fuel cell i–V curve. Renew Energy 2011;36:451–8. https://doi.org/10.1016/j.renene.2010.07.007

[138] Chugh S, Chaudhari C, Sonkar K, Sharma A, Kapur GS, Ramakumar SS V. Experimental and modelling studies of low temperature PEMFC performance. Int J Hydrogen Energy 2020. https://doi.org/10.1016/j.ijhydene.2020.01.019

[139] Pan M, Li C, Liao J, Lei H, Pan C, Meng X, et al. Design and modeling of PEM fuel cell based on different flow fields. Energy 2020:118331. https://doi.org/10.1016/j.energy.2020.118331

[140] Hao D, Shen J, Hou Y, Zhou Y, Wang H. An improved empirical fuel cell polarization curve model based on review analysis. Int J Chem Eng 2016;2016. https://doi.org/10.1155/2016/4109204

[141] Kim Y-S, Kim D-W, Lee I-S, Yoon S, Kim D, Jun S, et al. Effect of N^+ Implantation on Surface Characteristics of 316L Stainless Steels for Bipolar Plate in PEMFC. Coatings 2020;10:604. https://doi.org/10.3390/coatings10070604

[142] Yang LX, Liu RJ, Wang Y, Liu HJ, Zeng CL, Fu C. Growth of nanocrystalline β-Nb_2N coating on 430 ferritic stainless steel bipolar plates of PEMFCs by disproportionation reaction of Nb (IV) ions in molten salt. Corros Sci 2020:108862. https://doi.org/10.1016/j.corsci.2020.108862

[143] Gu W, Baker DR, Liu Y, Gasteiger HA. Proton exchange membrane fuel cell (PEMFC) down-the-channel performance model. Handb Fuel Cells 2010. https://doi.org/10.1002/9780470974001.f500044

[144] D'Souza C, Apicella M, El-kharouf A, Stamatakis E, Khzouz M, Stubos A, et al. Thermal characteristics of an air-cooled open-cathode proton exchange membrane fuel cell stack via numerical investigation. Int J Energy Res 2020. https://doi.org/10.1002/er.5785

[145] Pilinski N, Nagappan NK, Satola B, Rastedt M, Dyck A, Wagner P. Comparison of Carbon Based Bipolar Plate Materials for Polymer Electrolyte Membrane Fuel Cells. ECS Trans 2018;86:315. https://doi.org/10.1149/08613.0315ecst

[146] Liu X, Trabold TA. Non-active area water mitigation in PEM fuel cells via bipolar plate surface energy modification. Int J Hydrogen Energy 2018;43:908–20. https://doi.org/10.1016/j.ijhydene.2017.11.018

[147] Wilberforce T, El Hassan Z, Ogungbemi E, Ijaodola O, Khatib FN, Durrant A, et al. A comprehensive study of the effect of bipolar plate (BP) geometry design on the performance of proton exchange membrane (PEM) fuel cells. Renew Sustain Energy Rev 2019;111:236–60. https://doi.org/10.1016/j.rser.2019.04.081

[148] Weil KS, Xia G, Yang ZG, Kim JY. Development of a niobium clad PEM fuel cell bipolar plate material. Int J Hydrogen Energy 2007;32:3724–33. https://doi.org/10.1016/j.ijhydene.2006.08.041

[149] Wang L, Tao Y, Zhang Z, Wang Y, Feng Q, Wang H, et al. Molybdenum carbide coated 316L stainless steel for bipolar plates of proton exchange membrane fuel cells. Int J Hydrogen Energy 2019;44:4940–50. https://doi.org/10.1016/j.ijhydene.2018.12.184

[150] Alo OA, Otunniyi IO, Pienaar Hc, Iyuke SE. Materials for bipolar plates in polymer electrolyte membrane fuel cell: performance criteria and current benchmarks. Procedia Manuf 2017;7:395–401. https://doi.org/10.1016/j.promfg.2016.12.011

[151] Agarwal H, Pandey R, Bhat SD. Improved polymer electrolyte fuel cell performance with membrane electrode assemblies using modified metallic plate: Comparative study on impact of various coatings. Int J Hydrogen Energy 2020;45:18731–42. https://doi.org/10.1016/j.ijhydene.2019.05.243

[152] Sim Y, Kwak J, Kim S-Y, Jo Y, Kim S, Kim SY, et al. Formation of 3D graphene–Ni foam heterostructures with enhanced performance and durability for bipolar plates in a polymer electrolyte membrane fuel cell. J Mater Chem A 2018;6:1504–12. https://doi.org/ 10.1039/C7TA07598G

[153] Alo OA, Otunniyi IO, Pienaar H. Prospects of graphite-polypropylene/epoxy blend composite for high performance bipolar plate in polymer electrolyte membrane fuel cell. IOP Conf. Ser. Mater. Sci. Eng., vol. 655, IOP Publishing; 2019, p. 12035. https://doi.org/10.1088/1757-899X/655/1/012035

[154] Rzeczkowski P, Krause B, Pötschke P. Characterization of highly filled PP/graphite composites for adhesive joining in fuel cell applications. Polymers (Basel) 2019;11:462. https://doi.org/10.3390/polym11030462

[155] Kuan Y-D, Ciou C-W, Shen M-Y, Wang C-K, Fitriani RZ, Lee C-Y. Bipolar plate design and fabrication using graphite reinforced composite laminate for proton exchange membrane fuel cells. Int J Hydrogen Energy 2020. https://doi.org/10.1016/j.ijhydene.2020.08.030

[156] Raunija TSK, Gautam RK, Sharma SC, Verma A. Ultra-thin carbon/silicon carbide composite bipolar plate for advanced fuel cells: Ultradünne Kohlenstoff/Silizium Karbid-Verbundwerkstoff-Bipolarplatte für Brennstoffzellen. Materwiss Werksttech 2018;49:12–20. https://doi.org/10.1002/mawe.201700036

[157] Alavijeh MS, Kefayati H, Golikand AN, Shariati S. Synthesis and characterization of epoxy/graphite/nano-copper nanocomposite for the fabrication of bipolar plate for PEMFCs. J Nanostructure Chem 2019;9:11–8. https://doi.org/10.1007/s40097-019-0293-x

[158] Khaerudini DS, Prakoso GB, Insiyanda DR, Widodo H, Indiyaningsih N. Effect of graphite addition into mill scale waste as potential bipolar plates material of proton exchange membrane fuel cells. J Phys 2017. https://doi.org/10.1088/1742-6596/985/1/012050

[159] Lyons KS, Gould BD. Lightweight titanium metal bipolar plates for PEM fuel cells. Mater. Sci. Forum, vol. 879, Trans Tech Publ; 2017, p. 613–8. https://doi.org/10.4028/www.scientific.net/MSF.879.613

[160] Liu W, Qiu D, Peng L, Yi P, Lai X. Mechanical degradation of proton exchange membrane during assembly and running processes in proton exchange membrane fuel cells with metallic bipolar plates. Int J Energy Res 2020;44:8622–34. https://doi.org/10.1002/er.5550

[161] Nelissen G. Formed Metal Fuel Cell Bipolar Plates. ECS Trans 2017;80:435. https://doi.org/10.1149/08008.0435ecst

[162] Elyasi M, Ghadikolaee HT, Hosseinzadeh M. Fabrication of metallic bipolar plates in PEM fuel cell using semi-stamp rubber forming process. Int J Adv Manuf Technol 2017;92:765–76. https://doi.org/10.1007/s00170-017-0206-4

[163] Jin J, He Z, Zhao X. Formation of a protective TiN layer by liquid phase plasma electrolytic nitridation on Ti–6Al–4V bipolar plates for PEMFC. Int J Hydrogen Energy 2020. https://doi.org/10.1016/j.ijhydene.2020.02.152

[164] Li H, Guo P, Zhang D, Liu L, Wang Z, Ma G, et al. Interface-induced degradation of amorphous carbon films/stainless steel bipolar plates in proton exchange membrane fuel cells. J Power Sources 2020;469:228269. https://doi.org/10.1016/j.jpowsour.2020.228269

[165] Shimpalee S, Lilavivat V, McCrabb H, Khunatorn Y, Lee H-K, Lee W-K, et al. Investigation of bipolar plate materials for proton exchange membrane fuel cells. Int J Hydrogen Energy 2016;41:13688–96. https://doi.org/10.1016/j.ijhydene.2016.05.163

[166] Peng L, Yi P, Lai X. Design and manufacturing of stainless steel bipolar plates for proton exchange membrane fuel cells. Int J Hydrogen Energy 2014;39:21127–53. https://doi.org/10.1016/j.ijhydene.2014.08.113

[167] Zhang H, Cui J, Sun J, He W. Corrosion inhibition of methanol towards stainless steel bipolar plate for direct formic acid fuel cell. Int J Hydrogen Energy 2020. https://doi.org/10.1016/j.ijhydene.2020.08.038

[168] Mandal P, kumar Chanda U, Roy S. A review of corrosion resistance method on stainless steel bipolar plate. Mater Today Proc 2018;5:17852–6. https://doi.org/10.1016/j.matpr.2018.06.111

[169] Dubau L, Castanheira L, Maillard F, Chatenet M, Lottin O, Maranzana G, et al. A review of PEM fuel cell durability: materials degradation, local heterogeneities of aging and possible mitigation strategies. Wiley Interdiscip Rev Energy Environ 2014;3:540–60. https://doi.org/10.1002/wene.113

[170] Zhang W, Yi P, Peng L, Lai X. Strategy of alternating bias voltage on corrosion resistance and interfacial conductivity enhancement of TiCx/aC coatings on metallic bipolar plates in PEMFCs. Energy 2018;162:933–43. https://doi.org/10.1016/j.energy.2018.08.099

[171] Kurnia JC, Sasmito AP, Shamim T. Advances in proton exchange membrane fuel cell with dead-end anode operation: A review. Appl Energy 2019;252:113416. https://doi.org/10.1016/j.apenergy.2019.113416

[172] Wen D, Yin L, Piao Z, Li G, Leng Q. Performance investigation of proton exchange membrane fuel cell with intersectant flow field. Int J Heat Mass Transf 2018;121:775–87.
https://doi.org/10.1016/j.ijheatmasstransfer.2018.01.053

[173] Bing Y, Liu H, Zhang L, Ghosh D, Zhang J. Nanostructured Pt-alloy electrocatalysts for PEM fuel cell oxygen reduction reaction. Chem Soc Rev 2010;39:2184–202.
https://doi.org/10.1039/B912552C

[174] Haye E, Deschamps F, Caldarella G, Piedboeuf M-L, Lafort A, Cornil H, et al. Formable chromium nitride coatings for proton exchange membrane fuel cell stainless steel bipolar plates. Int J Hydrogen Energy 2020.
https://doi.org/10.1016/j.ijhydene.2020.03.248

[175] Ingle A V, Raja VS, Rangarajan J, Mishra P. Corrosion resistant quaternary Al–Cr–Mo–N coating on type 316L stainless steel bipolar plates for proton exchange membrane fuel cells. Int J Hydrogen Energy 2020;45:3094–107.
https://doi.org/10.1016/j.ijhydene.2019.11.119

[176] Yang Y, Guo L, Liu H. Corrosion characteristics of SS316L as bipolar plate material in PEMFC cathode environments with different acidities. Int J Hydrogen Energy 2011;36:1654–63.
https://doi.org/10.1016/j.ijhydene.2010.10.067

[177] Stein T, Ein-Eli Y. Proton exchange membrane (PEM) fuel cell bipolar plates prepared from a physical vapor deposition (PVD) titanium nitride (TiN) coated AISI416 stainless-steel. SN Appl Sci 2019;1:1420.
https://doi.org/10.1007/s42452-019-1475-3

[178] Wang Y, Northwood DO. Effects of O_2 and H_2 on the corrosion of SS316L metallic bipolar plate materials in simulated anode and cathode environments of PEM fuel cells. Electrochim Acta 2007;52:6793–8.
https://doi.org/10.1016/j.electacta.2007.05.001

[179] Simaafrookhteh S, Khorshidian M, Momenifar M. Fabrication of multi-filler thermoset-based composite bipolar plates for PEMFCs applications: Molding defects and properties characterizations. Int J Hydrogen Energy 2020.
https://doi.org/10.1016/j.ijhydene.2020.03.105

[180] Song D, Hao J, Yang F, Chen H, Liang N, Wu Y, et al. Corrosion behavior and mechanism of Cr–Mo alloyed steel: Role of ferrite/bainite duplex microstructure. J Alloys Compd 2019;809:151787.
https://doi.org/10.1016/j.jallcom.2019.151787

[181] Wang H, Turner JA. SnO_2: F coated ferritic stainless steels for PEM fuel cell bipolar plates. J Power Sources 2007;170:387–94.
https://doi.org/10.1016/j.jpowsour.2007.04.028

[182] Bong HJ, Lee J, Kim J-H, Barlat F, Lee M-G. Two-stage forming approach for manufacturing ferritic stainless steel bipolar plates in PEM fuel cell: Experiments and numerical simulations. Int J Hydrogen Energy 2017;42:6965–77. https://doi.org/10.1016/j.ijhydene.2016.12.094

[183] Yan W-M, Chen C-Y, Liang C-H. Comparison of performance degradation of high temperature PEM fuel cells with different bipolar plates. Energy 2019;186:115836. https://doi.org/10.1016/j.energy.2019.07.166

[184] Lan S, Xu Z, Jiang T, Peng L. Thin metallic wave-like channel bipolar plates for proton exchange membrane fuel cells: Deformation behavior, formability analysis and process design. J Power Sources 2019;444:227217. https://doi.org/10.1016/j.jpowsour.2019.227217

[185] Kumar N, Shaik GP, Pandurangan S, Khalkho B, Neelakantan L, Chetty R. Corrosion characteristics and fuel cell performance of a cost-effective high Mn–Low Ni austenitic stainless steel as an alternative to SS316L bipolar plate. Int J Energy Res 2020. https://doi.org/10.1002/er.5422

[186] Cho S, An J-H, Lee S-H, Kim J-G. Effect of pH on the Passive Film Characteristics of Lean Duplex Stainless Steel in Chloride-Containing Synthetic Tap Water. Int J Electrochem Sci 2020;15:4406–20. https://doi.org/10.20964/2020.05.32

[187] Lee SB, Cho KH, Lee WG, Jang H. Improved corrosion resistance and interfacial contact resistance of 316L stainless-steel for proton exchange membrane fuel cell bipolar plates by chromizing surface treatment. J Power Sources 2009;187:318–23. https://doi.org/10.1016/j.jpowsour.2008.11.064

[188] Wu J, Zhang W, Chai K, Yu A. Corrosion Behavior of AISI 1045 Steel in Seawater in the Presence of Flavobacterium sp. Front Microbiol 2020;11:303. https://doi.org/10.3389/fmicb.2020.00303

[189] Bai C-Y, Ger M-D, Wu M-S. Corrosion behaviors and contact resistances of the low-carbon steel bipolar plate with a chromized coating containing carbides and nitrides. Int J Hydrogen Energy 2009;34:6778–89. https://doi.org/10.1016/j.ijhydene.2009.05.103

[190] Nagode A, Jerina K, Jerman I, Vella D, Bizjak M, Kosec B, et al. The effect of sol–gel boehmite coatings on the corrosion and decarburization of C45 steel. J Sol-Gel Sci Technol 2018;86:568–79. https://doi.org/10.1007/s10971-018-4664-4

[191] Szala M, Szafran M, Macek W, Marchenko S, Hejwowski T. Abrasion Resistance of S235, S355, C45, AISI 304 and Hardox 500 Steels with Usage of Garnet, Corundum and Carborundum Abrasives. Adv Sci Technol Res J 2019;13. https://doi.org/10.12913/22998624/113244

[192] Bai C-Y, Wen T-M, Hou K-H, Ger M-D. The bipolar plate of AISI 1045 steel with chromized coatings prepared by low-temperature pack cementation for proton exchange membrane fuel cell. J Power Sources 2010;195:779–86. https://doi.org/10.1016/j.jpowsour.2009.08.036

[193] Bai C-Y, Wen T-M, Hou K-H, Pu N-W, Ger M-D. The characteristics and performance of AISI 1045 steel bipolar plates with chromized coatings for proton exchange membrane fuel cells. Int J Hydrogen Energy 2011;36:3975–83. https://doi.org/10.1016/j.ijhydene.2010.12.110

[194] Chang C-C. Effect of Metal Bipolar Plate Channel Fabrication on Electroplating–Using Nickel Electroplating of AISI 1045 Channel Substrate as an Example. Int J Electrochem Sci 2015;10:1926–39. http://scholars.ntou.edu.tw/handle/123456789/1939

[195] Song Y, Zhang C, Ling C-Y, Han M, Yong R-Y, Sun D, et al. Review on current research of materials, fabrication and application for bipolar plate in proton exchange membrane fuel cell. Int J Hydrogen Energy 2019. https://doi.org/10.1016/j.ijhydene.2019.07.231

[196] Wang H-C, Sheu H-H, Lu C-E, Hou K-H, Ger M-D. Preparation of corrosion-resistant and conductive trivalent Cr–C coatings on 304 stainless steel for use as bipolar plates in proton exchange membrane fuel cells by electrodeposition. J Power Sources 2015;293:475–83. https://doi.org/10.1016/j.jpowsour.2015.05.105

[197] Jinlong L, Tongxiang L, Hongyun L. Effect of grain refinement and electrochemical nitridation on corrosion resistance of the 316L stainless steel for bipolar plates in PEMFCs environment. J Power Sources 2015;293:692–7. https://doi.org/10.1016/j.jpowsour.2015.06.006

[198] Özkan D, Erarslan Y, Kincal C, Gürlü O, Yağci MB. Wear and corrosion resistance enhancement of chromium surfaces through graphene oxide coating. Surf Coatings Technol 2020:125595. https://doi.org/10.1016/j.surfcoat.2020.125595

[199] Tsai L-C, Sheu H-H, Chen C-C, Ger M-D. The preparation of the chromized coatings on AISI 1045 carbon steel plate with the electroplating pretreatment of Ni or Ni/Cr-C film. Int J Electrochem Sci 2015;10:317–31. www.electrochemsci.org/papers/vol10/100100317.pdf

[200] Dong Z, Zhou T, Liu J, Zhang X, Shen B, Hu W, et al. Performance of surface chromizing layer on 316L stainless steel for proton exchange membrane fuel cell bipolar plates. Int J Hydrogen Energy 2019;44:22110–21. https://doi.org/10.1016/j.ijhydene.2019.06.099

[201] Zhang D, Guo L, Duan L, Tuan W-H. Preparation of Cr-based multilayer coating on stainless steel as bipolar plate for PEMFCs by magnetron sputtering. Int J Hydrogen Energy 2011;36:2184–9. https://doi.org/10.1016/j.ijhydene.2010.10.085

[202] Găluşcă DG, Perju MC, Nejneru C, Nergiş DDB, Lăzărescu IE. Aluminum Coating Influence on Nitride Layer Performance Deposited by MO-CVD in Fluidized Bed on Austenitic Stainless Steel Substrate. MS&E 2018;374:12020. https://doi.org/10.1088/1757-899X/374/1/012020

[203] Li R, Dong C, Kong D, Ni X, Zhang L, Ao M, et al. Improved catalytic performance and corrosion resistance of selective laser melted 316L SS in a direct methanol fuel cell by surface anodization. Surf Coatings Technol 2020;399:126172. https://doi.org/10.1016/j.surfcoat.2020.126172

[204] Ysiwata-Rivera AP, Hernández-Hernández E, Cadenas-Pliego G, Ávila-Orta CA, González-Morones P, Jesús JA, et al. Effect of Modified Hexagonal Boron Nitride Nanoparticles on the Emulsion Stability, Viscosity and Electrochemical Behavior of Nanostructured Acrylic Coatings for the Corrosion Protection of AISI 304 Stainless Steel. Coatings 2020;10:488. https://doi.org/10.3390/coatings10050488

[205] Haghir T, Abbasi MH, Golozar MA, Panjepour M. Investigation of α to γ transformation in the production of a nanostructured high-nitrogen austenitic stainless steel powder via mechanical alloying. Mater Sci Eng A 2009;507:144–8. https://doi.org/10.1016/j.msea.2008.12.033

[206] Asri NF, Husaini T, Sulong AB, Majlan EH, Daud WRW. Coating of stainless steel and titanium bipolar plates for anticorrosion in PEMFC: A review. Int J Hydrogen Energy 2017;42:9135–48. https://doi.org/10.1016/j.ijhydene.2016.06.241

[207] McCay K, Kongstein OE, Oedegaard A, Barnett AO, Seland F. Soldering a gas diffusion layer to a stainless steel bipolar plate using metallic tin. Int J Hydrogen Energy 2018;43:9006–14. https://doi.org/10.1016/j.ijhydene.2018.03.188

[208] Tian R, Sun J. Effect of pH value on corrosion resistance and surface conductivity of plasma-nitrided 304L bipolar plate for PEMFC. Int J Energy Res 2011;35:772–80. https://doi.org/10.1002/er.1737

[209] Croll SG. Surface roughness profile and its effect on coating adhesion and corrosion protection: A review. Prog Org Coatings 2020;148:105847. https://doi.org/10.1016/j.porgcoat.2020.105847

[210] K Gautam R, Banerjee S, K Kar K. Bipolar plate materials for proton exchange membrane fuel cell application. Recent Patents Mater Sci 2015;8:15–45. https://doi.org/10.2174/1874464808666150306223104

[211] Wang H, Turner JA. Reviewing metallic PEMFC bipolar plates. Fuel Cells 2010;10:510–9. https://doi.org/10.1002/fuce.200900187

[212] Kumar A, Ricketts M, Hirano S. Ex situ evaluation of nanometer range gold coating on stainless steel substrate for automotive polymer electrolyte membrane fuel cell bipolar plate. J Power Sources 2010;195:1401–7.
https://doi.org/10.1016/j.jpowsour.2009.09.022

[213] Rajasekar S, Chetty R, Neelakantan L. Low-nickel austenitic stainless steel as an alternative to 316L bipolar plate for proton exchange membrane fuel cells. Int J Hydrogen Energy 2015;40:12413–23.
https://doi.org/10.1016/j.ijhydene.2015.05.194

[214] Hsieh H, Wang W-L, Lan C. Application of Carbon Coated Stainless Steel for Bipolar Plate in Proton Exchange Membrane Fuel Cell. ECS Trans 2014;64:917.
https://doi.org/10.1149/06403.0917ecst

[215] Wang H, Turner JA, Li X, Teeter G. Process modification for coating SnO_2: F on stainless steels for PEM fuel cell bipolar plates. J Power Sources 2008;178:238–47.
https://doi.org/10.1016/j.jpowsour.2007.12.010

[216] Ghorbani MM, Taherian R, Bozorg M. Investigation on physical and electrochemical properties of TiN-coated Monel alloy used for bipolar plates of proton exchange membrane fuel cell. Mater Chem Phys 2019;238:121916.
https://doi.org/10.1016/j.matchemphys.2019.121916

[217] De Las Heras N, Roberts EPL, Langton R, Hodgson DR. A review of metal separator plate materials suitable for automotive PEM fuel cells. Energy Environ Sci 2009;2:206–14.
https://doi.org/10.1039/B813231N

[218] Pozio A, Zaza F, Masci A, Silva RF. Bipolar plate materials for PEMFCs: a conductivity and stability study. J Power Sources 2008;179:631–9.
https://doi.org/10.1016/j.jpowsour.2008.01.038

[219] Devrim Y, Erkan S, Bac N, Eroglu I. Improvement of PEMFC performance with Nafion/inorganic nanocomposite membrane electrode assembly prepared by ultrasonic coating technique. Int J Hydrogen Energy 2012;37:16748–58.
https://doi.org/10.1016/j.ijhydene.2012.02.148

[220] Sadeghian Z, Hadidi MR, Salehzadeh D, Nemati A. Hydrophobic octadecylamine-functionalized graphene/TiO_2 hybrid coating for corrosion protection of copper bipolar plates in simulated proton exchange membrane fuel cell environment. Int J Hydrogen Energy 2020.
https://doi.org/10.1016/j.ijhydene.2020.04.015

[221] Husby H, Kongstein OE, Oedegaard A, Seland F. Carbon-polymer composite coatings for PEM fuel cell bipolar plates. Int J Hydrogen Energy 2014;39:951–7.
https://doi.org/10.1016/j.ijhydene.2013.10.115

[222] Tawfik H, Hung Y, Mahajan D. Metal bipolar plates for PEM fuel cell—a review. J Power Sources 2007;163:755–67.
https://doi.org/10.1016/j.jpowsour.2006.09.088

[223] Deyab MA, Mele G. Stainless steel bipolar plate coated with polyaniline/Zn-Porphyrin composites coatings for proton exchange membrane fuel cell. Sci Rep 2020;10:1–8. https://doi.org/10.1038/s41598-020-60288-9

[224] Lee Y-H, Li S-M, Tseng C-J, Su C-Y, Lin S-C, Jhuang J-W. Graphene as corrosion protection for metal foam flow distributor in proton exchange membrane fuel cells. Int J Hydrogen Energy 2017;42:22201–7. https://doi.org/10.1016/j.ijhydene.2017.03.233

[225] Wang W-L, He S-M, Lan C-H. Protective graphite coating on metallic bipolar plates for PEMFC applications. Electrochim Acta 2012;62:30–5. https://doi.org/10.1016/j.electacta.2011.11.026

[226] Wang Z, Feng K, Li Z, Lu F, Huang J, Wu Y, et al. Self-passivating carbon film as bipolar plate protective coating in polymer electrolyte membrane fuel cell. Int J Hydrogen Energy 2016;41:5783–92. https://doi.org/10.1016/j.ijhydene.2016.02.076

[227] Lee YH, Noh S, Lee J-H, Chun S-H, Cha SW, Chang I. Durable graphene-coated bipolar plates for polymer electrolyte fuel cells. Int J Hydrogen Energy 2017;42:27350–3. https://doi.org/10.1016/j.ijhydene.2017.09.053

[228] Yi P, Zhang D, Qiu D, Peng L, Lai X. Carbon-based coatings for metallic bipolar plates used in proton exchange membrane fuel cells. Int J Hydrogen Energy 2019;44:6813–43. https://doi.org/10.1016/j.ijhydene.2019.01.176

[229] Yoo J, Yeo KH, Shin EC, Jun YH. Nanometers Layered Conductive Carbon Coating on 316L Stainless Steel as Bipolar Plates for More Economical Automotive PEMFC. SAE Technical Paper; 2013. https://doi.org/10.4271/TU-001

[230] Che J, Yi P, Peng L, Lai X. Impact of pressure on carbon films by PECVD toward high deposition rates and high stability as metallic bipolar plate for PEMFCs. Int J Hydrogen Energy 2020. https://doi.org/10.1016/j.ijhydene.2020.04.078

[231] Hou K, Yi P, Peng L, Lai X. Niobium doped amorphous carbon film on metallic bipolar plates for PEMFCs: First principle calculation, microstructure and performance. Int J Hydrogen Energy 2019;44:3144–56. https://doi.org/10.1016/j.ijhydene.2018.12.040

[232] Jiang L, Syed JA, Gao Y, Zhang Q, Zhao J, Lu H, et al. Electropolymerization of camphorsulfonic acid doped conductive polypyrrole anti-corrosive coating for 304SS bipolar plates. Appl Surf Sci 2017;426:87–98. https://doi.org/10.1016/j.apsusc.2017.07.077

[233] Stein T, Ein-Eli Y. Challenges and Perspectives of Metal-Based Proton Exchange Membrane's Bipolar Plates: Exploring Durability and Longevity. Energy Technol 2020;8:2000007. https://doi.org/10.1002/ente.202000007

[234] Yeetsorn R, Ouajai WP, Onyu K. Studies on surface modification of polypropylene composite bipolar plates using an electroless deposition technique. RSC Adv 2020;10:24330–42. https://doi.org/10.1039/D0RA00461H

[235] Fu Y, Lin G, Hou M, Wu B, Shao Z, Yi B. Carbon-based films coated 316L stainless steel as bipolar plate for proton exchange membrane fuel cells. Int J Hydrogen Energy 2009;34:405–9. https://doi.org/10.1016/j.ijhydene.2008.10.068

[236] Pei H, Liu Z, Zhang H, Yu Y, Tu Z, Wan Z, et al. In situ measurement of temperature distribution in proton exchange membrane fuel cell I a hydrogen–air stack. J Power Sources 2013;227:72–9. https://doi.org/10.1016/j.jpowsour.2012.11.027

[237] Show Y, Takahashi K. Stainless steel bipolar plate coated with carbon nanotube (CNT)/polytetrafluoroethylene (PTFE) composite film for proton exchange membrane fuel cell (PEMFC). J Power Sources 2009;190:322–5. https://doi.org/10.1016/j.jpowsour.2009.01.027

[238] Chen G, Tao T, Gao P-P, Xie Z-Y, Wu X-B. Corrosion Protection of Amorphous Carbon Coating for the Bipolar Plates of PEMFCs. Surf Rev Lett 2019;26:1950059. https://doi.org/10.1142/S0218625X19500598

[239] Wilberforce T, Ijaodola O, Ogungbemi E, Khatib FN, Leslie T, El-Hassan Z, et al. Technical evaluation of proton exchange membrane (PEM) fuel cell performance–A review of the effects of bipolar plates coating. Renew Sustain Energy Rev 2019;113:109286. https://doi.org/10.1016/j.rser.2019.109286

[240] Hickmann T, Zielinski O. Bipolar Plates: Different Materials and Processing Methods for Their Usage in Fuel Cells. E3S Web Conf., vol. 160, EDP Sciences; 2020, p. 1002. https://doi.org/10.1051/e3sconf/202016001002

[241] Liu S, Pan TJ, Wang RF, Yue Y, Shen J. Anti-corrosion and conductivity of the electrodeposited graphene/polypyrrole composite coating for metallic bipolar plates. Prog Org Coatings 2019;136:105237. https://doi.org/10.1016/j.porgcoat.2019.105237

[242] Jiang L, Syed JA, Lu H, Meng X. In-situ electrodeposition of conductive polypyrrole-graphene oxide composite coating for corrosion protection of 304SS bipolar plates. J Alloys Compd 2019;770:35–47. https://doi.org/10.1016/j.jallcom.2018.07.277

[243] Peng S, Xu J, Li Z, Jiang S, Munroe P, Xie Z-H, et al. A reactive-sputter-deposited TiSiN nanocomposite coating for the protection of metallic bipolar plates in proton exchange membrane fuel cells. Ceram Int 2020;46:2743–57. https://doi.org/10.1016/j.ceramint.2019.09.263

[244] Mahmoudi M, Raeissi K, Karimzadeh F, Golozar MA. A study on corrosion behavior of graphene oxide coating produced on stainless steel by electrophoretic deposition. Surf Coatings Technol 2019;372:327–42. https://doi.org/10.1016/j.surfcoat.2019.05.050

[245] Yoon HW, Choi JY, Park HJ, Sun JH, Shin SY, Moon K Il. Zr-Based Thin Film Metallic Glass for Bipolar Plate in Proton Exchange Membrane Fuel Cell. Adv Eng Mater n.d. https://doi.org/10.1002/adem.202000369

[246] Korkmaz S, Kariper İA. Glass formation, production and superior properties of Zr-based thin film metallic glasses (TFMGs): A status review. J Non Cryst Solids 2020;527:119753. https://doi.org/10.1016/j.jnoncrysol.2019.119753

[247] Yiu P, Diyatmika W, Bönninghoff N, Lu Y-C, Lai B-Z, Chu JP. Thin film metallic glasses: Properties, applications and future. J Appl Phys 2020;127:30901. https://doi.org/10.1063/1.5122884

[248] Wei X, Ying C, Wu J, Jiang H, Yan B, Shen J. Fabrication, Corrosion, and Mechanical Properties of Magnetron Sputtered Cu–Zr–Al Metallic Glass Thin Film. Materials (Basel) 2019;12:4147. https://doi.org/10.3390/ma12244147

[249] Jia P, Huang R, Zhang S, Wang E, Yao J. Synthesis of Ag-Cr thin film metallic glasses with enhanced sulfide-resistance. J Mater Sci Technol 2020. https://doi.org/10.1016/j.jmst.2020.01.070

[250] Zhang B, Yang X, Cao G, Liu G, Wei Z, Zong H, et al. Characteristic studies on the ZrCuAlSi multi-component thin-film metallic glasses fabricated by pulsed laser deposition. Appl Phys A 2020;126:453. https://doi.org/10.1007/s00339-020-03631-1

[251] Meisner LL, Rotshtein VP, Semin VO, Markov AB, Yakovlev E V, Meisner SN, et al. Microstructural characterization and mechanical behavior of nanocomposite Ti-Ni-Nb surface alloys synthesized on TiNi SMA substrate by additive thin-film electron-beam mixing. Mater Charact 2020:110455. https://doi.org/10.1016/j.matchar.2020.110455

[252] Zhang B-Q, Liu G-P, Zong H-T, Fu L-G, Wei Z-F, Yang X-W, et al. Influence of Zr50Cu50 thin film metallic glass as buffer layer on the structural and optoelectrical properties of AZO films. Chinese Phys B 2020;29:37303. https://doi.org/10.1088/1674-1056/ab6c50

[253] Rigail-Cedeño AF, Espinoza-Andaluz M, Vera J, Orellana-Valarezo M, Villacis-Balbuca M. Influence of different carbon materials on electrical properties of epoxy-based composite for bipolar plate applications. Mater Today Proc 2020. https://doi.org/10.1016/j.matpr.2020.06.455

[254] Atik M, Aegerter MA. Corrosion resistant ZrO_2 sol-gel coating on stainless steel. 1992. http://dx.doi.org/10.22028/D291-24153

[255] Misra VC, Chakravarthy Y, Khare N, Singh K, Ghorui S. Strongly adherent Al_2O_3 coating on SS 316L: Optimization of plasma spray parameters and investigation of unique wear resistance behaviour under air and nitrogen environment. Ceram Int 2020;46:8658–68.
https://doi.org/10.1016/j.ceramint.2019.12.099

[256] Rasooli A, Safavi MS, Babaei F, Ansarian A. Electrodeposited Ni–Fe–Cr_2O_3 nanocomposite coatings: A survey of influences of Cr_2O_3 nanoparticles loadings in the electrolyte. J Alloys Compd 2020;822:153725.
https://doi.org/10.1016/j.jallcom.2020.153725

[257] Wu L-K, Wu J-J, Wu W-Y, Yan H-J, Jiang M-Y, Cao F-H. Hot corrosion behavior of electrodeposited SiO_2 coating on TiAl alloy. Corros Sci 2020;174:108827.
https://doi.org/10.1016/j.corsci.2020.108827

[258] de Souza Filho EA, Pieretti EF, Bento RT, Pillis MF. Effect of nitrogen-doping on the surface chemistry and corrosion stability of TiO_2 films. J Mater Res Technol 2020;9:922–34.
https://doi.org/10.1016/j.jmrt.2019.11.032

[259] Soufeiani L, Foliente G, Nguyen KTQ, San Nicolas R. Corrosion protection of steel elements in façade systems–a review. J Build Eng 2020:101759.
https://doi.org/10.1016/j.jobe.2020.101759

[260] Yang L, Qin ZL, Pan HT, Yun H, Min YL, Xu QJ. Corrosion protection of 304 stainless steel bipolar plates of PEMFC by coating SnO_2 film. Int J Electrochem Sci 2017;12:10946–57.
https://doi.org/10.20964/2017.11.67

[261] Manso AP, Marzo FF, Garicano X, Alegre C, Lozano A, Barreras F. Corrosion behavior of tantalum coatings on AISI 316L stainless steel substrate for bipolar plates of PEM fuel cells. Int J Hydrogen Energy 2020.
https://doi.org/10.1016/j.ijhydene.2019.12.157

[262] Park JH, Jeon BJ, Lee JK. Electrochemical characteristics of fluorine-doped tin oxide film coated on stainless steel bipolar plates. Surf Coatings Technol 2015;277:1–6.
https://doi.org/10.1016/j.surfcoat.2015.06.067

[263] Wang Y, Zhang S, Lu Z, Wang L, Li W. Preparation and performances of electrically conductive Nb-doped TiO_2 coatings for 316 stainless steel bipolar plates of proton-exchange membrane fuel cells. Corros Sci 2018;142:249–57.
https://doi.org/10.1016/j.corsci.2018.07.034

[264] Jin J, Hu M, Zhao X. Investigation of incorporating oxygen into TiN coating to resist high potential effects on PEMFC bipolar plates in vehicle applications. Int J Hydrogen Energy 2020;45:23310–26.
https://doi.org/10.1016/j.ijhydene.2020.06.059

[265] Dezfuli SM, Sabzi M. Deposition of self-healing thin films by the sol–gel method: a review of layer-deposition mechanisms and activation of self-healing mechanisms. Appl Phys A 2019;125:557. https://doi.org/10.1007/s00339-019-2854-8

[266] Carrera-Figueiras C, Pérez-Padilla Y, Estrella-Gutiérrez MA, Uc-Cayetano EG, Juárez-Moreno JA, Avila-Ortega A. Surface Science Engineering through Sol-Gel Process. Appl. Surf. Sci., IntechOpen; 2019. https://doi.org/10.5772/intechopen.83676

[267] Aparicio M, Mosa J. Electrochemical characterization of sol–gel coatings for corrosion protection of metal substrates. J Sol-Gel Sci Technol 2018;88:77–89. https://doi.org/10.1007/s10971-018-4785-9

[268] Ashraf MA, Liu Z, Peng W-X, Yoysefi N. Amino acid and TiO_2 nanoparticles mixture inserted into sol-gel coatings: an efficient corrosion protection system for AZ91 magnesium alloy. Prog Org Coatings 2019;136:105296. https://doi.org/10.1016/j.porgcoat.2019.105296

[269] de Castro Braga AV, do Lago DCB, Pimenta AR, de Senna LF. The influence of heat treatment of inorganic conversion coatings produced by sol-gel dip coating on the anticorrosive properties of alumina films deposited on steel substrate–Part I: Single conversion coatings. Surf Coatings Technol 2019;372:190–200. https://doi.org/10.1016/j.surfcoat.2019.05.040

[270] Bhuvaneshwari B, Vivekananthan S, Sathiyan G, Palani GS, Iyer NR, Rai PK, et al. Doping engineering of V-TiO_2 for its use as corrosion inhibitor. J Alloys Compd 2020;816:152545. https://doi.org/10.1016/j.jallcom.2019.152545

[271] Lai D, Kong G, Miao X, Che C. Effect of Silane Coating on the Corrosion Resistance of TiO_2 Conversion Films. Int J Electrochem Sci 2018;13:4055–70. https://doi.org/10.20964/2018.05.48

[272] Huang J-H, Kuo K-L, Yu G-P. Oxidation behavior and corrosion resistance of vacuum annealed ZrN-coated stainless steel. Surf Coatings Technol 2019;358:308–19. https://doi.org/10.1016/j.surfcoat.2018.11.054

[273] Bonu V, Jeevitha M, Kumar VP, Bysakh S, Barshilia HC. Ultra-thin multilayered erosion resistant Ti/TiN coatings with stress absorbing layers. Appl Surf Sci 2019;478:872–81. https://doi.org/10.1016/j.apsusc.2019.02.012

[274] Lopes RF, da Costa JAP, Silva W, Viana BC, Marciano FR, Lobo AO, et al. TiO_2 anti-corrosive thin films on duplex stainless steel grown using cathodic cage plasma deposition. Surf Coatings Technol 2018;347:136–41. https://doi.org/10.1016/j.surfcoat.2018.04.074

[275] Abdollahi B, Afzali D, Hassani Z. Corrosion inhibition properties of SiO_2-ZrO_2 nanocomposite coating on carbon steel 178. Anti-Corrosion Methods Mater 2018;65:66–72. https://doi.org/10.1108/ACMM-12-2015-1618

[276] Prabhu KN, Nayak U V. Quench Cooling Performance–Hardness Correlation for AISI 1045 and 1090 Steels. Mater Perform Charact 2019;8:135–50. https://doi.org/10.1520/MPC20180138

[277] Miao B, Zhao X, Song L, Wei K, Hu J. Raising the Corrosion Resistance of Plasma-Nitrided Steel 45 (AISI 1045) by Preliminary Sandblasting. Met Sci Heat Treat 2019;60:808–13. https://doi.org/10.1007/s11041-019-00360-y

[278] Huang ZH, Zhou YJ, Nguyen TT. Study of nickel matrix composite coatings deposited from electroless plating bath loaded with TiB_2, ZrB_2 and TiC particles for improved wear and corrosion resistance. Surf Coatings Technol 2019;364:323–9. https://doi.org/10.1016/j.surfcoat.2019.01.060

[279] Dias V, Maciel H, Fraga M, Lobo A, Pessoa R, Marciano F. Atomic layer deposited TiO_2 and Al_2O_3 thin films as coatings for aluminum food packaging application. Materials (Basel) 2019;12:682. https://doi.org/10.3390/ma12040682

[280] Peng D, Huang K, He Y, Zhang Z, Wang Y, Wu J. Hybrid sol-gel coating incorporated with TiO_2 nanosheets and anti-corrosive effects on AA2024-T3. Anti-Corrosion Methods Mater 2019;66:215–21. https://doi.org/10.1108/ACMM-08-2018-1980

[281] Stambolova I, Yordanov S, Lakov L, Vassilev S, Blaskov V, Jivov B. Preparation of sol-gel SiO_2 coatings on steel and their corrosion resistance. MATEC Web Conf., vol. 145, EDP Sciences; 2018, p. 5011. https://doi.org/10.1051/matecconf/201814505011

[282] Pouladvand I, Asl SK, Hoseini MG, Rezvani M. Nanostructured Ti/TiO_2–RuO_2–La_2O_3 anodes prepared by sol–gel process and the effect of electrolyte composition on their stability. Micro Nano Lett 2019;14:234–8. https://doi.org/10.1049/mnl.2018.5566

[283] Mazur A, Szczurek A, Chęcmanowski JG, Szczygieł B. Corrosion resistance and bioactivity of SiO_2-Y_2O_3 coatings deposited on 316L steel. Surf Coatings Technol 2018;350:502–10. https://doi.org/10.1016/j.surfcoat.2018.07.042

[284] Chęcmanowski JG, Szczygieł B. The effect of the deposition sequence of sol-gel SiO_2-Al_2O_3, CeO_2 and Y_2O_3 coatings on the corrosion resistance of the FeCrAl alloy during cyclic high-temperature oxidation. Surf Coatings Technol 2018;344:458–66. https://doi.org/10.4271/2019-28-0103

[285] Vega FLA, Olaya JJ, Ruiz JB. Synthesis and corrosion resistance of SiO_2-TiO_2-ZrO_2-Bi_2O_3 coatings spin-coated on Ti6Al4V alloy. Ceram Int 2018;44:2123–31. https://doi.org/10.1016/j.ceramint.2017.10.161

[286] Mumjitha M, Raj V. Fabrication of TiO_2–SiO_2 bioceramic coatings on Ti alloy and its synergetic effect on biocompatibility and corrosion resistance. J Mech Behav Biomed Mater 2015;46:205–21. https://doi.org/10.1016/j.jmbbm.2015.02.006

[287] Thamir AD, Mohammed FQ, Hanon MM. Fabrication of Ni–Al composite coating on stainless steel using hybrid gas-phase coating technique and its corrosion study. SN Appl Sci 2019;1:542. https://doi.org/10.1007/s42452-019-0556-7

[288] Cormier P-A, Dervaux J, Szuwarski N, Pellegrin Y, Odobel F, Gautron E, et al. Single Crystalline-like and Nanostructured TiO_2 Photoanodes for Dye Sensitized Solar Cells Synthesized by Reactive Magnetron Sputtering at Glancing Angle. J Phys Chem C 2018;122:20661–8. https://doi.org/10.1021/acs.jpcc.8b07192

[289] Mthisi A. Influence of Al_2O_3 addition on the hardness and in vitro corrosion behavior of laser synthesized Ti-Al_2O_3 coatings on Ti-6Al-4V. Int J Adv Manuf Technol 2019;100:917–27. https://doi.org/10.1007/s00170-018-2785-0

[290] Deyab MA, Nada AA, Hamdy A. Comparative study on the corrosion and mechanical properties of nano-composite coatings incorporated with TiO_2 nano-particles, TiO_2 nano-tubes, and ZnO nano-flowers. Prog Org Coatings 2017;105:245–51. https://doi.org/10.1016/j.porgcoat.2016.12.026

[291] Adachi T, Latthe SS, Gosavi SW, Roy N, Suzuki N, Ikari H, et al. Photocatalytic, superhydrophilic, self-cleaning TiO_2 coating on cheap, light-weight, flexible polycarbonate substrates. Appl Surf Sci 2018;458:917–23. https://doi.org/10.1016/j.apsusc.2018.07.172

[292] Razavi F, Shabani-Nooshabadi M, Behpour M. Sol-gel synthesis, characterization and electrochemical corrosion behavior of SNC-doped TiO_2 nano coating on copper. J Mol Liq 2018;266:99–105. https://doi.org/10.1016/j.molliq.2018.06.056

[293] Shi Y, Wang N, Liu L, Liu Y. Surface sedimentation and adherence of Nano-SiO_2 to improve thermal stability and flame resistance of melamine-formaldehyde foam via sol-gel method. Fire Mater 2018;42:183–9. https://doi.org/10.1002/fam.2478

[294] Sasireka A, Rajendran R, Priya P, Raj V. Ciprofloxacin-Loaded Ceramic/Polymer Composite Coatings on Ti with Improved Antibacterial and Corrosion Resistance Properties for Orthopedic Applications. ChemistrySelect 2019;4:1166–75. https://doi.org/10.1002/slct.201803769

[295] Stambolova I, Lakov L, Vassilev S, Jivov B, Nedelcheva-Bachvarova A. Corrosion stability in salt medium of stainless steel and carbon steel, using different oxide sol gel coatings. Mater Sci Non-Equilibrium Phase Transform 2019;5:16–8. https://stumejournals.com/journals/ms/2019/1/16

[296] Kanwal S, Thakare JG, Pandey C, Singh I, Mahapatra MM. Characterization of slurry-based mullite coating deposited on P91 steel welds. J Aust Ceram Soc 2019;55:519–28. https://doi.org/10.1007/s41779-018-0258-4

[297] Chęcmanowski JG, Szczygieł I, Mazur A, Szczygieł B. Protective properties of SiO_2 with SiO_2 and Al_2O_3 nanoparticles sol-gel coatings deposited on FeCrAl alloys. Ceram Int 2019;45:2811–9. https://doi.org/10.1016/j.ceramint.2018.07.295

[298] Uchiyama H, Bando T, Kozuka H. Effect of the amount of H_2O and HNO_3 in Ti ($OC_3H_7^i$) 4 solutions on the crystallization of sol-gel-derived TiO_2 films. Thin Solid Films 2019;669:157–61. https://doi.org/10.1016/j.tsf.2018.10.050

[299] Zhao Y, Zhang Z, Shi L, Zhang F, Li S, Zeng R. Corrosion resistance of a self-healing multilayer film based on SiO_2 and CeO_2 nanoparticles layer-by-layer assembly on Mg alloys. Mater Lett 2019;237:14–8. https://doi.org/10.1016/j.matlet.2018.11.069

[300] Wu L-K, Wu W-Y, Song J-L, Hou G-Y, Cao H-Z, Tang Y-P, et al. Enhanced high temperature oxidation resistance for γ-TiAl alloy with electrodeposited SiO_2 film. Corros Sci 2018;140:388–401. https://doi.org/10.1016/j.corsci.2018.05.025

[301] Shi S, Zhao Y, Zhang Z, Yu L. Corrosion protection of a novel SiO_2@PANI coating for Q235 carbon steel. Prog Org Coatings 2019;132:227–34. https://doi.org/10.1016/j.porgcoat.2019.03.040

[302] Tavakoli S, Nemati S, Kharaziha M, Akbari-Alavijeh S. Embedding CuO Nanoparticles in PDMS-SiO_2 Coating to Improve Antibacterial Characteristic and Corrosion Resistance. Colloid Interface Sci Commun 2019;28:20–8. https://doi.org/10.1016/j.colcom.2018.11.002

[303] Gutierrez Martinez M, Guerra L, Bermudez Reyes B, Cabriales R, Reyes LA. Characterization of SiO_2-TiO_2 Coatings on 316l Stainless Steel Substrates. J Adv Mater Process 2018;6:3–13. http://jmatpro.iaun.ac.ir/article_623122.html

[304] Dobruchowska E, Gilewicz A, Warcholinski B, Libralesso L, Batory D, Szparaga L, et al. Al-Mn based coatings deposited by cathodic arc evaporation for corrosion protection of AISI 4140 alloy steel. Surf Coatings Technol 2019;362:345–54. https://doi.org/10.1016/j.surfcoat.2019.02.014

[305] Xing Q, Wang H, Chen M, Chen Z, Li R, Jin P, et al. Mechanical Properties and Corrosion Resistance of NbTiAlSiZrNx High-Entropy Films Prepared by RF Magnetron Sputtering. Entropy 2019;21:396. https://doi.org/10.3390/e21040396

[306] Lu T-W, Feng C-S, Wang Z, Liao K-W, Liu Z-Y, Xie Y-Z, et al. Microstructures and mechanical properties of $CoCrFeNiAl_{0.3}$ high-entropy alloy thin films by pulsed laser deposition. Appl Surf Sci 2019;494:72–9. https://doi.org/10.1016/j.apsusc.2019.07.186

[307] Wang Y, Huang Z, Gurney RS, Liu D. Superhydrophobic and photocatalytic PDMS/TiO_2 coatings with environmental stability and multifunctionality. Colloids Surfaces A Physicochem Eng Asp 2019;561:101–8. https://doi.org/10.1016/j.colsurfa.2018.10.054

[308] Gapale DL, Arote SA, Palve BM, Dalvi SN, Borse RY. Effect of film thickness on humidity sensing of spray deposited TiO_2 thin films. Mater Res Express 2018;6:26402. https://orcid.org/0000-0002-6404-9597

[309] Kozlovskiy A, Shlimas I, Dukenbayev K, Zdorovets M. Structure and corrosion properties of thin TiO_2 films obtained by magnetron sputtering. Vacuum 2019;164:224–32. https://doi.org/10.1016/j.vacuum.2019.03.026

[310] Liu Y, Liu R, Liu M. Improved sintering ability of SiC ceramics from SiC@Al_2O_3 core-shell nanoparticles prepared by a slow precipitation method. Ceram Int 2019;45:8032–6. https://doi.org/10.1016/j.ceramint.2019.01.023

[311] Dehghanghadikolaei A, Ansary J, Ghoreishi R. Sol-gel process applications: A mini-review. Proc Nat Res Soc 2018;2:2008. https://doi.org/10.11605/j.pnrs.201802008

[312] Yu J, Ji G, Shi Z, Wang X. Corrosion resistance of ZrO_2 films under different humidity coal gas conditions at high temperature. J Alloys Compd 2019;783:371–8. https://doi.org/10.1016/j.jallcom.2018.12.322

[313] John S, Salam A, Baby AM, Joseph A. Corrosion inhibition of mild steel using chitosan/TiO_2 nanocomposite coatings. Prog Org Coatings 2019;129:254–9. https://doi.org/10.1016/j.porgcoat.2019.01.025

[314] Karimi Sahnesarayi M, Sarpoolaky H, Rastegari S. Influence of Multiple Coating and Heat Treatment Cycles on the Performance of Nano-TiO_2 Coating in Protection of 316L Stainless Steel against Corrosion under UV Illumination and Dark Conditions. Iran J Mater Sci Eng 2019;16:33–42. https://doi.org/10.22068/ijmse.16.2.33

[315] Leong KH, Lee JQ, Kumar AA, Sim LC, Pichiah S. Facile techniqe for the immobilisation of TiO_2 nanoparticles on glass substrates for application in the photocatalytic self-cleaning of indoor air pollutants. Malaysian J Anal Sci 2019;23:90–9.
https://doi.org/10.17576/mjas-2019-2301-11

[316] Krishna V, Padmapreetha R, Chandrasekhar SB, Murugan K, Johnson R. Oxidation resistant TiO_2–SiO_2 coatings on mild steel by Sol–Gel. Surf Coatings Technol 2019:125041.
https://doi.org/10.1016/j.surfcoat.2019.125041

[317] Johari ND, Rosli ZM, Juoi JM, Yazid SA. Comparison on the TiO_2 crystalline phases deposited via dip and spin coating using green sol–gel route. J Mater Res Technol 2019;8:2350–8.
https://doi.org/10.1016/j.jmrt.2019.04.018

[318] Boukerche S, Himour A, Bououdina M, Bensouici F, Ouchenane S. Multilayered ZnO/TiO_2 nanostructures as efficient corrosion protection for stainless steel 304. Mater Res Express 2019;6:55052.
https://doi.org/10.1088/2053-1591/ab042f

[319] Kumar S, Kumar S, Sivakumar M. Investigation of anticorrosion properties of nanocomposites of spray coated zinc oxide and titanium dioxide thin films on stainless steel (304L SS) in saline environment. Mater Res Express 2018;5:14006.
https://doi.org/10.1088/2053-1591/aaa2bd

[320] La J, Song M, Kim H, Lee S, Jung W. Effect of deposition temperature on microstructure, corrosion behavior and adhesion strength of Zn-Mg coatings on mild steel. J Alloys Compd 2018;739:1097–103.
https://doi.org/10.1016/j.jallcom.2017.12.289

[321] Wang X, Xia Y, Zuo X, Schaper SJ, Yin S, Ji Q, et al. Synergistic effects from super-small sized TiO_2 and SiOx nanoparticles within TiO_2/SiOx/carbon nanohybrid lithium-ion battery anode. Ceram Int 2019;45:14327–37.
https://doi.org/10.1016/j.ceramint.2019.04.147

[322] El Nahrawy AM, Haroun AA, Abou Hammad AB, Diab MA, Kamel S. Uniformly Embedded Cellulose/Polypyrrole-TiO_2 Composite in Sol-Gel Sodium Silicate Nanoparticles: Structural and Dielectric Properties. Silicon 2019;11:1063–70.
https://doi.org/10.1007/s12633-018-9910-4

[323] Beverskog B, Puigdomenech I. Revised pourbaix diagrams for iron at 25–300C. Corros Sci 1996;38:2121–35.
https://doi.org/10.1016/S0010-938X(96)00067-4

[324] Chun MC, Park S, Park S, Park G, Kang BS. Effects of repetitive polarization switching on the coercive voltage of Pt/Pb $(Zr_{0.52}Ti_{0.48})O_3$/Pt thin films analyzed using impedance spectroscopy. Curr Appl Phys 2019;19:503–5.
https://doi.org/10.1016/j.cap.2019.02.003

[325] Qiu P, Sun X, Lai Y, Gao P, Chen C, Ge L. N-doped TiO_2@TiO_2 visible light active film with stable and efficient photocathodic protection performance. J Electroanal Chem 2019;844:91–8. https://doi.org/10.1016/j.jelechem.2019.05.020

[326] Alves-Lima DF, Letizia R, Degl'Innocenti R, Dawson R, Lin H. Quantitative video-rate hydration imaging of Nafion proton exchange membranes with terahertz radiation. J Power Sources 2020;450:227665. https://doi.org/10.1016/j.jpowsour.2019.227665

[327] Hu M, Triulzi G, Sharifzadeh M. Technological change in fuel cell technologies. Des. Oper. Solid Oxide Fuel Cells, Elsevier; 2020, p. 3–41. https://doi.org/10.1016/B978-0-12-815253-9.00001-X

[328] Park H, Kim D-K, Kim H, Oh S, Jung WS, Kim S-K. Binder-coated electrodeposited PtNiCu catalysts for the oxygen reduction reaction in high-temperature polymer electrolyte membrane fuel cells. Appl Surf Sci 2020;510:145444. https://doi.org/10.1016/j.apsusc.2020.145444

[329] Shi J, Zhang P, Han Y, Wang H, Wang X, Yu Y, et al. Investigation on electrochemical behavior and surface conductivity of titanium carbide modified Ti bipolar plate of PEMFC. Int J Hydrogen Energy 2020;45:10050–8. https://doi.org/10.1016/j.ijhydene.2020.01.203

[330] Kargar-Pishbijari H, Hosseinipour SJ, Aval HJ. A novel method for manufacturing microchannels of metallic bipolar plate fuel cell by the hot metal gas forming process. J Manuf Process 2020;55:268–75. https://doi.org/10.1016/j.jmapro.2020.04.040

[331] Bouziane K, Lachat R, Zamel N, Meyer Y, Candusso D. Impact of cyclic mechanical compression on the electrical contact resistance between the gas diffusion layer and the bipolar plate of a polymer electrolyte membrane fuel cell. Renew Energy 2020;153:349–61. https://doi.org/10.1016/j.renene.2020.02.033

[332] Pilinski N, Käding C, Dushina A, Hickmann T, Dyck A, Wagner P. Investigation of Corrosion Methods for Bipolar Plates for High Temperature Polymer Electrolyte Membrane Fuel Cell Application. Energies 2020;13:235. https://doi.org/10.3390/en13010235

[333] Alo OA, Otunniyi IO, Pienaar Hc, Sadiku ER. Electrical and mechanical properties of polypropylene/epoxy blend-graphite/carbon black composite for proton exchange membrane fuel cell bipolar plate. Mater Today Proc 2020. https://doi.org/10.1016/j.matpr.2020.03.642

[334] Li X, Zhou P, Ogle K, Proch S, Paliwal M, Jansson A, et al. Transient stainless-steel dissolution and its consequences on ex-situ bipolar plate testing procedures. Int J Hydrogen Energy 2020;45:984–95. https://doi.org/10.1016/j.ijhydene.2019.10.191

[335] Leng Y, Ming P, Yang D, Zhang C. Stainless steel bipolar plates for proton exchange membrane fuel cells: Materials, flow channel design and forming processes. J Power Sources 2020;451:227783. https://doi.org/10.1016/j.jpowsour.2020.227783

[336] Li T, Zhang PC, Liu K, Xu S, Han YT, Shi JF, et al. Performance of Tantalum Modified 316L Stainless Steel Bipolar Plate for Proton Exchange Membrane Fuel Cell. Fuel Cells 2019;19:724–30. https://doi.org/10.1002/fuce.201900099

[337] Lu JL, Abbas N, Tang J, Hu R, Zhu GM. Characterization of Ti_3SiC_2-coating on stainless steel bipolar plates in simulated proton exchange membrane fuel cell environments. Electrochem Commun 2019;105:106490. https://doi.org/10.1016/j.elecom.2019.106490

[338] Hua Q, Zeng Y, He Z, Xu Q, Min Y. Microstructure, synergistic mechanism and corrosion behavior of tin oxide conversion film modified by chitosan on aluminum alloy surface. Colloid Interface Sci Commun 2020;36:100262. https://doi.org/10.1016/j.colcom.2020.100262

[339] Wang Y, Zhang S, Lu Z, Wang P, Ji X, Li W. Preparation and performance of electrically conductive Nb-doped TiO_2/polyaniline bilayer coating for 316L stainless steel bipolar plates of proton-exchange membrane fuel cells. RSC Adv 2018;8:19426–31. https://doi.org/10.1039/C8RA02161A

[340] Huang K, Zhang D, Hu M, Hu Q. Cr_2O_3/C composite coatings on stainless steel 304 as bipolar plate for proton exchange membrane fuel cell. Energy 2014;76:816–21. https://doi.org/10.1016/j.energy.2014.08.076

[341] Mohammadi N, Yari M, Allahkaram SR. Characterization of PbO_2 coating electrodeposited onto stainless steel 316L substrate for using as PEMFC's bipolar plates. Surf Coatings Technol 2013;236:341–6. https://doi.org/10.1016/j.surfcoat.2013.10.010

[342] Kamnerdkhag P, Free ML, Shah AA, Rodchanarowan A. The effects of duty cycles on pulsed current electrodeposition of $ZnNiAl_2O_3$ composite on steel substrate: Microstructures, hardness and corrosion resistance. Int J Hydrogen Energy 2017;42:20783–90. https://doi.org/10.1016/j.ijhydene.2017.06.049

[343] Khosravi S, Veerapandiyan VK, Vallant R, Reichmann K. Effect of processing conditions on the structural properties and corrosion behavior of TiO_2–SiO_2 multilayer coatings derived via the sol-gel method. Ceram Int 2020. https://doi.org/10.1016/j.ceramint.2020.04.079

[344] Wang Y, Zhang S, Wang P, Chen S, Lu Z, Li W. Electropolymerization and corrosion protection performance of the Nb:TiO_2 nanofibers/polyaniline composite coating. J Taiwan Inst Chem Eng 2019;103:190–8. https://doi.org/10.1016/j.jtice.2019.07.015

[345] Figueira RB, Sousa R, Silva CJR. Multifunctional and smart organic–inorganic hybrid sol–gel coatings for corrosion protection applications. Adv. Smart Coatings Thin Film. Futur. Ind. Biomed. Eng. Appl., Elsevier; 2020, p. 57–97. https://doi.org/10.1016/B978-0-12-849870-5.00008-2

[346] Wang D, Bierwagen GP. Sol–gel coatings on metals for corrosion protection. Prog Org Coatings 2009;64:327–38. https://doi.org/10.1016/j.porgcoat.2008.08.010

[347] Cui L-Y, Cheng S-C, Liang L-X, Zhang J-C, Li S-Q, Wang Z-L, et al. In vitro corrosion resistance of layer-by-layer assembled polyacrylic acid multilayers induced Ca–P coating on magnesium alloy AZ31. Bioact Mater 2020;5:153–63. https://doi.org/10.1016/j.bioactmat.2020.02.001

[348] Martin U, Ress J, Bosch J, Bastidas DM. Stress corrosion cracking mechanism of AISI 316LN stainless steel rebars in chloride contaminated concrete pore solution using the slow strain rate technique. Electrochim Acta 2020;335:135565. https://doi.org/10.1016/j.electacta.2019.135565

[349] Abbas N, Shao GN, Imran SM, Haider MS, Kim HT. Inexpensive synthesis of a high-performance Fe_3O_4-SiO_2-TiO_2 photocatalyst: Magnetic recovery and reuse. Front Chem Sci Eng 2016;10:405–16. https://doi.org/10.1007/s11705-016-1579-x

[350] Biglu YFG, Taheri-Nassaj E. Investigation of phase separation of nano-crystalline anatase from TiO_2-SiO_2 thin film. Ceram Int 2013;39:2511–8. https://doi.org/10.1016/j.ceramint.2012.09.010

[351] Dihingia PJ, Rai S. Synthesis of TiO_2 nanoparticles and spectroscopic upconversion luminescence of Nd^{3+}-doped TiO_2–SiO_2 composite glass. J Lumin 2012;132:1243–51. https://doi.org/10.1016/j.jlumin.2011.12.008

[352] Kim YN, Shao GN, Jeon SJ, Imran SM, Sarawade PB, Kim HT. Sol–gel synthesis of sodium silicate and titanium oxychloride based TiO_2–SiO_2 aerogels and their photocatalytic property under UV irradiation. Chem Eng J 2013;231:502–11. https://doi.org/10.1016/j.cej.2013.07.072

[353] Zita J, Maixner J, Krýsa J. Multilayer TiO_2/SiO_2 thin sol–gel films: Effect of calcination temperature and Na^+ diffusion. J Photochem Photobiol A Chem 2010;216:194–200. https://doi.org/10.1016/j.jphotochem.2010.07.030

[354] Yang Z, Xu Y, Yang S. Fabrication, characterization, and photocatalytic performance of TiO_2 hybridized with SiO_2. Russ J Appl Chem 2016;89:2050–60. https://doi.org/10.1134/S107042721612017X

[355] Yan S-R, Gholami T, Amiri O, Salavati-Niasari M, Seifi S, Amiri M, et al. Effect of adding TiO_2, SiO_2 and graphene on of electrochemical hydrogen storage performance and coulombic efficiency of $CoAl_2O_4$ spinel. J Alloys Compd 2020;828:154353. https://doi.org/10.1016/j.jallcom.2020.154353

[356] Kapridaki C, Maravelaki-Kalaitzaki P. TiO_2–SiO_2–PDMS nano-composite hydrophobic coating with self-cleaning properties for marble protection. Prog Org Coatings 2013;76:400–10. https://doi.org/10.1016/j.porgcoat.2012.10.006

[357] Yang J, Liang Q. TiO_2/SiO_2 membrane materials via a sol–gel process: preparation and characterization calcined under N_2 atmosphere. Ferroelectrics 2019;547:10–20. https://doi.org/10.1080/00150193.2019.1592478

[358] Koli VB, Mavengere S, Kim J-S. An efficient one-pot N doped TiO_2-SiO_2 synthesis and its application for photocatalytic concrete. Appl Surf Sci 2019;491:60–6. https://doi.org/10.1016/j.apsusc.2019.06.123

[359] Kirtay S. Characterization of SiO_2-TiO_2 Hybrid Corrosion Protective Coatings on Mild Steel. J Mater Eng Perform 2014;23:4309–15. https://doi.org/10.1007/s11665-014-1218-y

[360] Krzak-Roś J, Filipiak J, Pezowicz C, Baszczuk A, Miller M, Kowalski M, et al. The effect of substrate roughness on the surface structure of TiO_2, SiO_2, and doped thin films prepared by the sol-gel method. Acta Bioeng Biomech 2009;11:21–9. https://www.researchgate.net/publication/38020698

[361] Halin DSC, Abdullah M, Mahmed N, Malek SNAA, Vizureanu P, Azhari AW. Synthesis and Characterization of TiO_2/SiO_2 Thin Film via Sol-Gel Method. IOP Conf. Ser. Mater. Sci. Eng., vol. 209, IOP Publishing; 2017, p. 12002. https://doi.org/10.1088/1757-899X/209/1/012002

[362] Riazian M, Montazeri N, Biazar E. Nano structural properties of TiO_2-SiO_2. Orient J Chem 2011;27:903. http://www.orientjchem.org/?p=11735

[363] Wiranwetchayan O, Promnopat S, Thongtem T, Chaipanich A, Thongtem S. Effect of polymeric precursors on the properties of TiO_2 films prepared by sol-gel method. Mater Chem Phys 2020;240:122219. https://doi.org/10.1016/j.matchemphys.2019.122219

[364] Gulyaev A, Kondrutieva O, Koldaev V, Koltsov V. Building a Three-dimensional Purbe Diagram. 2020 IEEE Conf. Russ. Young Res. Electr. Electron. Eng., IEEE; 2020, p. 1960–3. https://doi.org/10.1109/EIConRus49466.2020.9039304

[365] Wongpanya P, Saramas Y, Chumkratoke C, Wannakomol A. Erosion–corrosion behaviors of 1045 and J55 steels in crude oil. J Pet Sci Eng 2020;189:106965. https://doi.org/10.1016/j.petrol.2020.106965

[366] Li Q, Dong L, Yang Y, Wu Z, Zhu H, Dong Y, et al. Corrosion Behavior of AISI 1045 Carbon Steel in Metalworking Fluids Containing Pseudomonas xiamenensis. Int J Electrochem Sci 2020;15:470–83. https://doi.org/10.20964/2020.01.60

[367] Aversa A, Saboori A, Librera E, de Chirico M, Biamino S, Lombardi M, et al. The Role of Directed Energy Deposition Atmosphere Mode on the Microstructure and Mechanical Properties of 316L Samples. Addit Manuf 2020:101274. https://doi.org/10.1016/j.addma.2020.101274

[368] Boes J, Röttger A, Becker L, Theisen W. Processing of gas-nitrided AISI 316L steel powder by laser powder bed fusion–Microstructure and properties. Addit Manuf 2019;30:100836. https://doi.org/10.1016/j.addma.2019.100836

[369] He RY, Jiang J, Wang RF, Yue Y, Chen Y, Pan TJ. Anti-corrosion and conductivity of titanium diboride coating on metallic bipolar plates. Corros Sci 2020:108646. https://doi.org/10.1016/j.corsci.2020.108646

[370] Mani SP, Rajendran N. Corrosion and interfacial contact resistance behavior of electrochemically nitrided 316L SS bipolar plates for proton exchange membrane fuel cells. Energy 2017;133:1050–62. https://doi.org/10.1016/j.energy.2017.05.086

[371] Yang S, Brant AT, Giles NC, Halliburton LE. Intrinsic small polarons in rutile TiO_2. Phys Rev B 2013;87:125201. https://doi.org/10.1103/PhysRevB.87.125201

[372] Di Valentin C, Pacchioni G, Selloni A. Reduced and n-type doped TiO_2: nature of Ti^{3+} species. J Phys Chem C 2009;113:20543–52. https://doi.org/10.1021/jp9061797